SYNTHESIS, CHARACTERIZATION, AND *IN VITRO* EVALUATION OF NEAR-INFRARED ABSORBING CONDUCTIVE POLYMER NANOPARTICLES AS AGENTS FOR PHOTOTHERMAL ABLATION OF BREAST CANCER CELLS

by

Travis Cantu, B.S., M.S.

A dissertation submitted to the Graduate Council of
Texas State University in partial fulfillment
of the requirements for the degree of
Doctor of Philosophy
with a Major in Materials Science, Engineering, and Commercialization
December 2015

Committee Members:

Jennifer A. Irvin and Tania Betancourt, Co-Chairs

James Tunnell

Shannon Weigum

John Burns

FAIR USE AND AUTHOR'S PERMISSION STATEMENT

Fair Use

Duplication Permission

DEDICATION

To my mother, father, sister, and wife

ACKNOWLEDGEMENTS

I would like to thank my co-advisers Dr. Jenifer Irvin and Dr. Tania Betancourt for their constant support and guidance through my Ph.D. studies. I am grateful for the opportunity that they gave me in allowing me to apprentice under them. They constantly pushed me to achieve my best allowing me to reach levels that I never thought I could accomplish. Though them I not only learned about science but also about life and what it takes to be a successful in this occupation. Dr. Irvin constantly gave me positive reinforcement helping me see the bright side of any tough situation, and Dr. Betancourt always kept me on task and constantly challenged me. I truly believe I could not have had better advisors, during my graduate studies. Thank you both very much. I would also like to thank Dr. Shannon Weigum and Dr. John Burns for taking the time to be on my committee and giving valuable feedback on my projects as I progress though my graduate studies.

I am very grateful for the support Dr. James Tunnell gave me during my project. He treated me as one of his own students and with out his contribution I would not have been able to complete my studies. I would also like to thank the graduate students in the Tunnell research group for there patients, support, and guidance, specifically Dr. Varun Pattani for get settled in the lab and sharing his knowledge with me. I would also like to thank Dr. Austin Moy for helping me during the later stages of dissertation; you always gave me positive feedback and was supportive through the whole process.

I would like to thank my previous advisor Dr. Javier Macossay for giving me my first opportunity to do research. The research I did while studying under him as well as his encouragement motivated me to pursue a higher education. I would also like to give thanks to people that were apart of the early stages of my research career: Sean Pelfry and Erving Morales were my first mentors when I started doing research, Raj Desai was the first undergraduate that I trained and was a key contributor to my early work, and Dr. Faheem Sheik whom encouraged me and always pushed me to look for opportunities to expand my knowledge and constantly grow.

I would like to thank all of the members of the Irvin research group Leslie Wood, Brad Roider, Dean Dornak, Jacob Frasier, Ryan Charles, Zachary Izzard, Marvin Solano, and I would like to give a special thanks to Sothavy Vong, Katherina Webber, and Alissa Kilian for all their hard work and time that they contributed to helping me. I know work in the lab can be tedious and you all really made my life much easier.

I also want to thank the students in the Betancourt research group specifically, Robert Danso, Renato Navarro, Tugba Ozel, Karolyn Barker, and I would like to give a very special thanks to Kyle Walsh for contributing his time and effort in helping me complete my work.

I would also like to acknowledge the life long friends I have made along this journey. My high school friends, Ben Smith, Alex Sotelo, Daniel Zamora, Juan Perez, Ivan (Alvin) Briones, Dr. Luis Monsivais, and Isidro (Rambo) Armijo and the fiends I made during my undergraduate studies, John Hamilton, Aniekan Okon, Jerry Escano,

Eric Gonzales, and Xujun Zhang thanks for all you support and always treating me as a brother. I would also like to thank the Materials Science Engineering and Commercialization and everyone involved in the early stages of the program, Dr. Tom Myers, Dr. Gary Beall, and Karla Pizana. I would also like to thank all the students in the program specifically Jeff Simpson, Amber Douglas, Tyler Nash, Sayaton Das, and Marcus Goss.

I would like to thank the Vela family for all their support as well as my immediate family, my sister, Monique Yvette Chavez, and both my parents, Janie and Juan Cantu for supporting me though all of my education and always being there for me. Lastly I would like to thank the most important person in my life, my wife, Clarisa, for supporting me though all the tough time and for being the light in the dark shinning right through my heart. Our journey has just begun.

TABLE OF CONTENTS

Page

LIST OF TABLES

Table **Page**

LIST OF FIGURES

Figure **Page**

ABSTRACT

In recent years, photothermal therapy (PTT) has emerged as a viable alternative for cancer treatment. Much effort has been devoted to finding various types of PTT agents with excellent heat generation, photothermal efficiency, biocompatibility, and biodegradability. In this work, polymeric nanoparticles (NPs) composed of poly(1,4-bis(3,4-ethylenedioxythienyl)-2,5-dialkoxybenzenes) (PBEDOT-B$(OR)_2$) and poly(3,4-ethylenedioxythiophene) (PEDOT) were synthesized using microemulsion polymerization. The NPs were characterized using dynamic light scattering, UV-Vis-NIR spectroscopy, and electron microscopy. The microemulsion polymerization yielded sub–100 nm NPs and the colloidal suspensions exhibited a strong absorbance in the near infrared region. The photothermal transduction and efficiency of these materials were determined and compared to those of commonly used PTT agents. When irradiated with NIR light, the suspensions showed a temperature change of ca. 30 °C with a photothermal efficiency of ca. 35%. *In vitro* cytocompatibility studies were also performed on the conductive polymeric NPs in an effort to determine the concentration limits that could be used without causing toxicity to cells. Cytocompatibility studies for the colloid suspensions were conducted at 24 h and exposure times, and the NPs were found to be non-toxic at a dose of 50 μg/mL. Photothermal *in vitro* studies also demonstrated that cell death can be achieved after 5 min of irradiation at concentrations as low as 0.5 μg/mL. These results suggest that these materials could be good candidates for use as photothermal therapy (PTT) agents.

1 INTRODUCTION

1.1 Motivation

Cancer accounts for nearly 1 out of every 4 deaths in the United States[1]. It is predicted that in the United States alone there will be a total of 1.6 million new cancer cases by the end of 2015, and that cancer will account for nearly 600,000 deaths in the United States alone.[1] According to the American Cancer Society, the direct medical cost for cancer in the United States in 2011 was $88.7 billion, and these cost is projected to hit $158 billion by 2020.[2] It is known that cancer incidence increases as a result of exposure to external factors, including UV and radiation exposure, tobacco use, alcohol use, and lack of exercise and diet, but it is still difficult to predict and sometimes diagnose this disease.[1]

Currently, breast cancer is one of the leading causes of cancer-related mortality among women in the United States, accounting for an estimated 40,000 deaths annually.[3] It is also estimated that 231,840 women will be diagnosed with breast cancer in the coming year.[1] It was estimated that in 2011 nearly $16.5 billion was spent on the care and treatment of breast cancer.[2] Recent progress in breast cancer treatment has slowly been shifting from the use of cytotoxic drugs to more highly sophisticated therapies that target specific molecules or pathways.[3] The main course of action once the cancer is detected typically involves either breast-conserving surgery (removal of the tumor and surrounding tissue), or mastectomy (removal of the entire breast).[1] Radiation therapy and chemotherapy are also still commonly used before and after surgery. Hormone therapy has proven to be an effective treatment; however, this treatment method only benefits patients that test positive for overexpression of specific receptors, making them sensitive

to hormones.[4] Many of these treatment options are invasive or are limited to select patients.

In the past quarter century, the emergence of nanomaterials has led to rapid advancements in biomedicine and biomaterials; specifically, nanoparticles have made a significant impact, leading to advances in diagnostics, drug delivery, imaging, sensing, and therapy.[5–7] Nanoparticles can be engineered in an array of shapes and sizes through the use of wet chemistry. This has propelled nanoparticles to be considered the future of medicine, allowing for less invasive imaging, detection, and therapy for several diseases.

1.2 Overall Research Project

One treatment option that is at the early stages of development is photothermal therapy (PTT). Photothermal therapy (PTT) is a light-based therapy where photothermal (PT) agents are injected intravenously; once these agents are accumulated at the tumor site either by passive or active targeting, light that corresponds to the absorbing wavelength of the PT agent is used to excite the material.[8] This in turn creates localized heating, resulting in the PT ablation of cancer cells in the vicinity but not affecting surrounding healthy tissue.[8] Figure 1-1 illustrates the PTT process. This therapy is a drug-free process that is making a transition from the laboratory to the clinic. Nanoparticles used in biomedicine and more specifically in PTT typically range in size from 1 – 200 nm and can be made up of an array of materials including metals and polymers. The shape of the nanoparticles also varies greatly; morphologies such as spheres, rods, hollow spheres, and cubes are all achievable.[9] The advantage of using nanoparticles in PTT will be discussed in more detail in Chapter 2. Currently, the standard materials used as PT agents consist of metal nanoparticles such as gold nanorods

and gold nanoshells. While these materials have been extensively studied as PT agents, other organic-based materials such as carbon nanotubes, several different organic dyes, and conductive polymers have also been reported as PT agents.

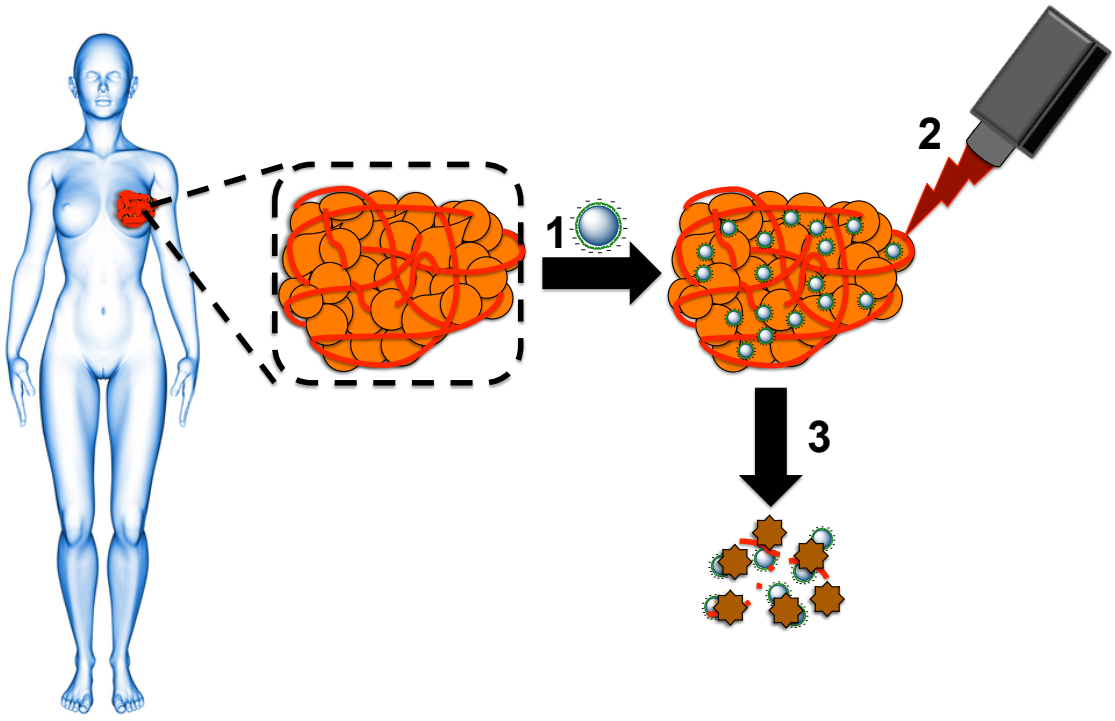

Figure 1-1. Phtotothermal therapy. 1. The nanoparticles are introduced to the site of the tumor either intravenously or by direct injection to the tumor. 2. Near infrared radiation is used to excite the nanoparticles, generating heat. 3. The heat generated by the nanoparticles causes ablation of the cells

In this work, the synthesis of polymer-based PT agents that can be used for PTT is reported. The PT agents in this work are sub-100 nm and have a high absorbance in the near infrared region (NIR). The PT agents are based on conductive polymers, specifically poly(3,4-ethylenedioxythiophene) (PEDOT, P3) and PEDOT derivatives. Two PEDOT derivatives were synthesized, poly(1,4-bis[2-(3,4-ethylenedioxy thienyl]-2,5-dihexyloxybenzene) (P1) and poly(diethyl 4,4'-{[2,5-bis(2,3-dihydrothieno[3,4-b][1,4]

dioxin-5-yl)-1,4-phenylene] bis(oxy)} butanoate) (P2). The absorbance and electrochemical effects of the pendant groups on the benzene ring were explored. Nanoparticles of these monomers were synthesized via oxidative emulsion polymerization in the presence of PSS-co-MA as the stabilizer. The photothermal conversion efficiency of the polymer nanoparticles was determined and compared to that of gold nanorods and commercially available poly(3,4-ethylenedioxythiophene):poly(styrenesulfonate) (PEDOT:PSS). The cytocompatibility and therapeutic effect enabled by photothermal heating of breast carcinoma cells exposed to the nanoparticles were investigated.

1.3 Specific Aims

The specific aims addressed in this project are the following:

1. **Synthesize and characterize novel 3,4-ethylenedioxythienyl monomers.** The preparation of the monomers was accomplished by coupling 3,4-ethylenedioxythiophene to 1,4-dibromo-2,5-dialkoxybenzenes. The monomers were polymerized chemically and electrochemically.
2. **Prepare, characterize, and optimize conductive polymeric nanoparticles using the monomers prepared previously.** The preparation of nanoparticles was explored using two different methods: a single surfactant system and a two-surfactant system. The optimal method of synthesis was determined for the different polymers by examining NIR absorbance and nanoparticle size.
3. **Examine the photothermal heating and photothermal conversion efficiency of the synthesized nanoparticles.** Photothermal heating was determined by

irradiating the nanoparticle suspensions with an 808-nm laser. The heating of the synthesized nanoparticles was compared to commercially available conductive polymer suspensions as well as gold nanorods at the same concentration and optical density.

4. **Determine the cytotoxicity and the photothermal effect of the nanoparticles *in vitro*.** Cytotoxicity studies were carried out in a human breast cancer cell line. The photothermal effect of the nanoparticles as a function of irradiation time, nanoparticle concentration, and laser settings was studied *in vitro* using the same breast cancer cell line.

1.4 Dissertation Outline

Chapter 2 provides background relevant to this work. Chapter 3 describes the monomer and polymer synthesis and characterization. Chapter 4 describes nanoparticle preparation and characterization of unique poly(1,4-bis(3,4-ethylenedioxythienyl)-2,5-dialkoxybenzene) and poly(3,4-ethylenedioxythiophene) nanoparticles via emulsion polymerization. Chapter 5 summarizes results regarding the photothermal conversion efficiency of the nanoparticles, the performance of the nanoparticles in comparison to gold nanorods and commercially available conductive polymer nanoparticles, cytotoxicity of the nanoparticles to breast carcinoma cells, and photothermal ablation of breast carcinoma cells when irradiated in the presence of the synthesized photothermal agents. Finally, Chapter 6 summarizes the conclusions of this research and explores the future potential of this technology.

2 BACKGROUND

2.1 Nanoparticles in Modern Medicine

Nanoparticles are being used in a number of different areas in medicine. Two fields within medicine that nanoparticles have greatly contributed to are in imaging and drug delivery/therapeutics. A powerful imaging technique that is commonly used in medicine is fluorescence imaging. Fluorescence imaging is a highly sensitive technique that allows for the visualization of small molecules that have been fluorescently labeled within the body.[7] This technique can be used to observe biodistribution of fluorescent markers, such as fluorescent drug delivery systems, fluorescent guided therapies, and fluorescent imaging diagnostics. In most fluorescence imaging applications, extrinsic fluorescent probes are utilized to label tissues or processes of interest. Fluorophores are used as these probes are able to emit light when excited by light of a specific wavelength. Some characteristics of fluorophores used in biomedical imaging are high fluorescence quantum yield in the visible and near infrared (NIR) region (600 – 1000 nm), photostability, and resistance to degradation in the body.[7] In the NIR window (700 – 900 nm), blood, hemoglobin, oxygenated hemoglobin, and other biological chromophores have very little absorbance, resulting in a deeper penetration depth of light in this wavelength range.[10] Thus the NIR region is advantageous to scientist and doctors using light-based therapies. Fluorescent nanoparticles are an effective tool for image-guided tumor surgery. Hill *et al.* described the synthesis of self-assembled indocyanine green nanoparticles by encapsulating the green dye in hyaluronic acid.[11] *In vivo* fluorescence image-guided surgery studies demonstrated that enhanced fluorescence at the tumor site was observed when mice were injected intravenously with fluorescent nanoparticles.[11]

The use of nanoparticles as drug delivery systems (DDSs) and therapeutics for the treatment of cancer aims to improve the biodistribution and selectivity of potent chemotherapeutics as a means to improve therapeutic efficacy and reduce the severe side effect normally associated with conventional chemotherapeutic treatments.[12] In controlled DDSs, the chemotherapeutic is encapsulated within the nanoparticle and introduced to the body by intravenous injection or by direct injection to the tumor. The use of DDSs leads to improved biodistribution and circulation time in the body, allowing for more localized treatment. By improving biodistribution, circulation time in the body, and selectivity, DDSs reduce the required treatment dosage and the severe side effects caused by chemotherapeutics.

Liposomal systems are one of the first and most well-studied DDSs. The first FDA-approved liposomal DDS was Doxil®, which received approval in 1995. Doxil® is an injectable liposomal DDS that is modified with poly(ethylene glycol) (PEG) on the surface. Doxil® has been approved to treat both breast and ovarian cancer. Abraxane™ is another DDS that was approved by the FDA in 2005 for chemotherapy. Abraxane™ is an albumin-based therapy where albumin is bound to paclitaxel, a chemotherapeutic, and is unique in that the drug is encapsulated by a human protein.[13] Abraxane™ has been approved to treat metastatic breast cancer, non-small cell lung cancer, and pancreatic cancer. Both doxorubicin and paclitaxel are insoluble hydrophobic drugs that are extremely toxic, but by using a DDS the bioavailability of the drug is increased and the pharmacokinetics of the drug are improved.[13] Since the approval of Doxil® in 1995, there have been a handful of other DDS approved by the US FDA and other countries around

the world, with several others in the clinical trial phase. Table 2-1 gives a list of DDS that are approved or in the later stages of clinical trials for breast cancer treatment.

Table 2-1. Nanomedicines approved by the FDA or which are in clinical trials for breast cancer treatment.[13]

Nanomedicine	Encapsulated Drug	Area of Treatment	FDA approval
Doxil®	Doxorubicin	Breast and ovarian cancer	November 1995
Abraxane™	Paclitaxel	Breast, pancreatic, and non-small cell cancer	January 2005
Myocet	Doxorubicin	Breast cancer	Approved in Europe and Canada, 2000
Genexol-PM	Paclitaxel	Breast and small cell lung cancer	Sold in Europe and Korea
Narekt-102	Irinotecan	Breast and colorectal cancer	Clinical phase III
LEP-ETU	Paclitaxel	Breast, ovarian, and lung cancer	Clinical phase II
Endo TAG-1	Paclitaxel	Breast and pancreatic cancer	Clinical phase II
Lipoplatin	Cisplatin	Breast, pancreatic, and head and neck cancer	Clinical phase III

2.2 Nanoparticle Delivery

Nanoparticles are typically administered intravenously as suspensions. The nanoparticles circulate in the bloodstream and concentrate at the tumor location either by passive or active targeting. In passive targeting, the nanoparticle accumulation in the tumor tissue is a size-dependent process that takes advantage of the enhanced permeability and retention (EPR) effect. The theory behind the EPR effect is that when tumor cells begin to rapidly multiply and reach a size of 2 – 3 mm, the nutrient and

oxygen demand to sustain these cells is increased.[14] This leads to angiogenesis, the formation of new vessels, also known as neovascularization, or the reordering of existing vessels near the tumor.[15] These newly formed tumor vessels are structurally abnormal, leading to highly disorganized tumor vessels and dilation, creating pores with sizes on the order of 100 – 2000 nm.[6,15] The tumor tissue also demonstrates poor lymphatic drainage, leading to longer retention time.[16] This allows macromolecules and nanoparticles to accumulate in the tumor tissue. Also of note is that in order to take advantage of the EPR effect, the nanoparticles must not be seen as foreign objects in the body, as this will lead to clearance of the nanoparticles by the reticuloendothelial system.[13] One approach to prevent clearance by reticuloendothelial system is by coating the surface of the nanoparticle with poly(ethylene glycol) (PEG).[13,17] The PEG coating is advantageous because it has been shown to have high biocompatibility, and it increases circulation time of proteins and nanocarriers in the blood. Additionally, end-functionalized PEG can potentially undergo surface modification in order to introduce additional functionalization of the surface of the nanoparticle.[17]

Active targeting involves the use of affinity ligands that specifically target diseased cells. Most commonly the recognition ligands are covalently attached directly on the surface of the nanoparticle, or through linker molecules that are on the surface of the nanoparticle. However, physical absorption using affinity ligands has also shown to be effective.[18] The approach used to conjugate the ligands to the nanoparticle depends on whether the particle is inorganic or organic. For example, most inorganic particles require modification with either amine or hydroxyl groups on the surface, whereas organic

particles may require the incorporation of linker molecules with terminal functionalization before or after nanoparticle synthesis.[18]

Attachment of molecules to nanoparticles can be carried out through a variety of different conjugation chemistry methods. Conjugation can be accomplished using cabodiimide crosslinker chemistry, where a carboxylic acid is activated using 1-ethyl-3-(3-dimethylaminopropyl)cabodiimide (EDC) with or without N-hydroxysuccinimide (NHS) and crosslinked to a primary amine on the affinity ligand through an amide bond.[19] Another approach involves coupling a maleimide group on the nanoparticle to the thiol group on the affinity ligand, yielding a thioether bond.[19] More recently, a new conjugation method was developed known as click-chemistry. This single step reaction can occur with or without the use of a copper catalyst depending on the reactants used. When a catalyst is not used the reaction is referred to as copper-free click chemistry. The classic example of copper-free click chemistry, is the reaction of azides and cyclic alkynes by strain-driven cycloaddition.[20] Nieves *et al.* reported maleimide functionalization of gold nanoparticles by copper-free click chemistry.[21] In this procedure gold nanoparticles were first azide functionalized, followed by using copper-free click chemistry to bind dibenzocycloctyne functionalized with a malemide group to the surface of the gold nanoparticle.[21]

Non-covalent attachment of ligands onto the surface of the nanoparticle is also an effective approach. Lidke *et al.* reported the conjugation of biotinylated epidermal growth factor (EGF) to the surface of quantum dots that were bioconjugated to streptavidin.[22] The biotin-streptavidin interaction is one of the strongest non-covalent bonds and has been used to conjugate ligands to nanoparticles. The fundamental weakness of the biotin-

streptavidin method for conjugation of ligands onto the surface of nanoparticles is that exogenous proteins on the surface lead to an immune response, known as immunogenicity. In addition, crosslinking among the nanoparticles can occur due to biotin binding with avidin.[23] Other non-covalent methods have been explored, including the use of high affinity complexes such as an adamantane-cyclodextrin complex.[23] Affinity ligands, including aptamers, antibodies, proteins, peptides, and other small molecules such as vitamins, can be covalently attached to the surface of the nanoparticle to increase binding specificity.[23] Selection of the appropriate ligand is dependent on the ultimate application of the nanoparticle. The nanoparticles will bind to the target cell by ligand-receptor interactions, where the receptors are overexpressed in cancer cells.

2.3 Targeting Breast Cancer

Several studies have demonstrated successful delivery of nanoparticles to breast cancer cells by effectively targeting human epidermal growth factor receptor 2 (HER-2). HER-2 is a protein with an intracellular tyrosine kinase domain and an extracellular ligand binding domain. HER-2 is from the HER tyrosine kinase receptor family which consists of HER-1 (also called epidermal growth factor receptor,), HER-2, HER-3, and HER-4.[24] While HER-2 is expressed in healthy tissue at low levels, it is significantly overexpressed in breast cancer.[25] HER-2 is found in about 1 in 5 patients with breast cancer. These patients that overexpress HER-2 are considered HER-2 positive (+).[26] There are three FDA approved monoclonal antibodies that target the HER-2 protein. The first approved humanized monoclonal antibody was trastuzumab, which binds to the extracellular domain of HER-2. Jang *et al*. reported the synthesis of trastuzumab-conjugated liposomal magnetic nanoparticles and demonstrated a significant increase in

the uptake of trastuzumab-conjugated particles by HER-2+ cells compared to their controls.[25] Pertuzumab is also a humanized monoclonal antibody that was approved to treat HER-2+ breast cancer cells in 2012.[26] Since the mechanisms of binding for pertuzumab and trastuzumab are different, they can be used in combination to improve breast cancer treatment. This combination therapy is currently in clinical phase III trials.

2.4 Photothermal Therapy

As mentioned above, photothermal therapy (PTT) is a light-based therapy where photothermal (PT) agents are excited to produce localized heating. Using heat to treat diseases is something that already occurs naturally in the human body. A fever is an example of the body raising the internal temperature a few degrees to help defend against an infection. A fever is a natural form of hyperthermia treatment. The body normally maintains a temperature of 37 °C; when this temperature is elevated to 42 °C, cells are more susceptible to damage. Hyperthermia as a treatment has been explored as a cancer therapeutic.[27,28] Hyperthermia treatment helps kills cancer cells by heating the affected area to a temperatures of 41 to 46 °C.[27] This increase in temperature damages the cells and enhances the effectiveness of radiation or chemotherapy. Any temperature above 46 ^{o}C is considered thermo-ablation, which leads to irreversible cell destruction through protein denaturation and coagulation.[27,29] Hyperthermia treatment can be used to treat the entire body or specific locations. Magnetic fluids have been explored for local hyperthermia treatment. Gilcherst *et al.* first postulated the use of magnetic fluid for hyperthermia treatment in 1957.[30] Since then, there have been many studies reporting the use of magnetic nanoparticles for cancer treatment. The magnetic nanoparticles in colloidal suspensions can be delivered using the same methods used for DDS. Once the

nanoparticles are at the target site they can be heated using alternating magnetic frequencies, resulting in heating in deep tissues. This method is also selective: only areas that contain the magnetic fluid are heated, thereby sparing healthy tissue. Small paramagnetic particles have been the preferred material for hyperthermia treatment; this is due to single-domain particles absorbing at more physiologically-relevant magnetic fields than those of multi-domain particles.[31] Iron oxide nanoparticles are almost exclusively used in hyperthermia therapy. The advantages of this material are their biocompatibility, ease of synthesis, and high magnetism.[31,32]

More recently, the use of laser light has been employed to generate thermal damage in cancerous tissue. The use of lasers in surgery was first reported by in 1963, followed by another report of the use of laser light for tumor eradication in 1965.[29] However, the sole use of laser therapy is not preferred due to lack of selectivity and high power density requirements.[29] On the other hand, laser use in combination with other components has proven to be very effective and has recently become a larger area of interest. One type of tumor therapy that uses laser light to its advantage is photodynamic therapy (PDT). Photodynamic therapy destroys cells by the production of toxic singlet oxygen and other reactive oxygen species. This occurs when photosensitizers react with oxygen within the tissue after exposure to a specific wavelength of light, either in the visible or the NIR region.[33] One of the first sensitizers reported was acridine, which was introduced in 1900.[33] Since then, there have been several different chemicals reported for PDT. Porphyrin-based sensitizers are the most preferred for clinical applications.[34] This is due to their high yields of singlet oxygen, high selectivity for cancerous tissue, and their relatively fast elimination from the body.[34]

Currently, Photofrin®, a purified hematoporphyrin derivative, is a photosensitizer used in PDT that has been approved by the FDA to help treat endobronchial cancer, esophageal cancer, and high-grade dysplasia in Barrett's esophagus.[35] One of the limitations of Photofrin® is that it absorbs light at wavelengths shorter than 640 nm, only allowing for treatment just under the skin or the lining of internal organs.[34] For deeper tumors, second generation photosensitizers are used, which have a strong absorbance in the NIR region.[34] FDA-approved second generation photosensitizers are listed in Table 2-2.

Table 2-2. List of photosensitizer dyes approved by the U.S. FDA for PDT treatment.[35]

Nanomedicine	PS Compound	Application	FDA Approval
Photofrin	Profimer sodium	Esophageal* and lung cancer**, and Barrett's esophagus***	1995* 1998** 2003***
Levulan	5-Aminolevulinic acid	Actinic keratosis	1999
Metvixia	Methyl aminolevulinate	Actinic keratosis	2004
Cysview	Hexaminolevulinate	Bladder cancer	2010
Visudine	Benzoporphyrin derivative monoacid ring A	Age-related macular degeneration	1999

Similar to PDT, photothermal therapy (PTT) uses laser light in combination with a light-absorbing material to kill cancer cells. However, instead of using photosensitizers, PTT uses photothermal agents to achieve selective heating. The PTT agents absorb laser light, gaining enough energy for electrons to transition from the ground state to the excited state, after which the electrons relax back to the ground state through nonradiative decay. This results in an increase in kinetic energy leading to overheating of the local environment.[29] This type of treatment is considered a form of hyperthermia known as

optical hyperthermia.[36] To be useful under physiological conditions, photothermal agents must absorb in the NIR window range.

The type of laser used –whether a continuous wave (cw) or short-pulsed laser— also plays a role in how the PT agent is heated. The main differences are the required exposure time, cell killing mechanism, and the size of the damage.[37] Using a cw laser the PT agents are exposed to irradiation for several minutes at a time, after which the heat generated is then conducted to the surrounding medium eventually leading to photothermal ablation.[38] When using a short-pulsed laser, the PT agents are exposed to irradiation at femto- to nano-second intervals. This leads to fast thermal expansion of the material or surrounding liquid, which leads to the generation of acoustic waves.[39] Additionally, microbubble formation and acoustic waves are generated by rapid evaporation of the surrounding liquids.[39] El-Sayed *et al*. studied the different mechanisms of cell death caused when gold nanospheres are excited with either cw or pulsed wave lasers.[37] It was determined that the use of a cw laser led to apoptotic cell death, whereas the use of a single pulsed laser led to necrotic cell death.[37] Both cw and pulsed lasers can be used in PTT, and the selection of the type of laser depends on the treatment trying to be achieved.

Initially, PTT agents explored consisted of natural chromophores found in tissue or extrinsic dye molecules such as indocyanine green, an FDA-approved tricarbocyanine dye with a spectral absorbance at 780 to 805 nm.[40–42] One drawback of using natural chromophores is their weak absorption. PTT agents should have a strong absorbance in the NIR region and effectively convert light to heat, which reduces the laser power density required to damage the targeted tissue. While dye molecules, such as indocyanine

green, have a strong absorbance in the NIR region, under laser irradiation the molecules may experience photobleaching, rendering them useless.[29]

With advances in nanotechnology, there have been several different nanomaterials with unique optical properties that have been found to be useful in biomedical applications. Nanoparticles that demonstrate a strong absorbance in the NIR region and that are able to efficiently convert light to heat, are candidates for PT agents. Materials that are at the forefront as PT agents due to their unique optical properties are gold nanospheres, gold nanoshells, gold nanorods, gold nanocages, carbon nanotubes and conductive polymers. Gold colloids have demonstrated a strong absorbance in the visible region due surface plasmon resonance (SPR).[43] The SPR of the gold nanoparticles is dependent on the size, shape, structure, and surrounding media.[44] It is reported that as the size of the gold nanoparticle increases, the absorption maximum redshifts to the NIR region.

When the shape of the gold nanoparticle is changed from spherical to rod-shaped, the material exhibits two absorbance bands.[10,45] Gold nanorods (GNRs) have strong absorption in the NIR region and a weaker absorbance in the visible region due to transverse electronic oscillation.[44] GNRs demonstrate a significant redshift when the aspect ratio is increased. This is also seen in gold nanoshells (GNSs). First reported by Halas *et al.* in 1998, GNSs were initially composed of silica cores 100 nm in diameter and surrounded by a thin layer of gold shells ranging 5 – 20 nm in thickness.[46] These GNSs show a strong absorbance in the NIR region, and the optical properties can be tuned by adjusting the ratio of the silica core to the gold shell.[47] Since this early work,

there have been several studies demonstrating the effectiveness of gold nanoparticles as PTT agents.

One of the earliest studies demonstrating GNSs as PTT agents was first reported by Hirsch *et al*.[48] In the study, GNSs with a strong absorbance in the NIR region were PEGylated and incubated in the presence of breast carcinoma cells. *In vitro* studies showed irreversible photothermal cell damage after exposure to 820 nm laser light at a power density of 35 W/cm^2 for 4 min.[48] *In vivo* studies were performed by injecting the nanoparticles directly into the tumor and then exposing the tumor region to 820 nm light at a power density of 4 W/cm^2 for 4 min. It was reported that magnetic resonance temperature imaging recorded a temperature rise of more than 30 ^{o}C, leading to irreversible tissue damage.[48] In 2002, Halas and West founded Nanospectra Biosciences, Inc., a company that focuses on the development AuroLase® therapy utilizing AuroShell® Particles (GNSs) that were developed by the Halas group. Currently AuroShell® has advanced to clinical phase 1 trials and is being studied for the treatment of head and neck cancers, as well as metastatic lung tumors.[13]

GNRs have also shown to be a promising material for PTT agents. El-Sayed *et al.* first demonstrated the PTT potential of GNRs *in vitro*.[49] GNRs conjugated to anti-EGFR antibodies were incubated in three different cell lines: HaCaT (human keratinocytes), HOC 313 clone 8, and HSC 3 (human oral squamous cancer cells). The cells were irradiated at 800 nm for 4 min, and it was found that the cells containing GNRs were photothermally damaged at half of the power density (10 W/cm^2) compared to non-cancerous cells that were irradiated at 20 W/cm^2.[49] In an extensive study comparing GNRs to GNSs, Pattani *et al.* demonstrated that at the same optical density, GNRs have

twice the PT conversion efficiency than GNSs; however, in order to achieve equivalent heating, 36 times the concentration of GNRs compared to the concentration of GNSs is required.[50] It was concluded that the cell death pathway is influenced by the localization of the GNRs this can then be used to maximize apoptosis cell death.

While the bulk of the research has focused on GNRs and GNSs as PT agents, other materials have also been explored. Xia and coworkers have shown that hollow gold nanoparticles are promising candidates for use as PT agents.[51,52] In one of the first reports of the use of gold nanocages, Chen *et al.* synthesized gold nanocages that were 45 nm in size and exhibited a strong resonance absorption peak in the NIR range.[53] The gold nanocages were conjugated with anti-HER2 targeting EGRF overexpressed on breast cancer cells. Irreversible cell damage was observed when tumors/cells were irradiated for 5 min at a power density of 1.5 W/cm^2 after exposure to the nanocages.[53] Rengan *et al*. compared the effectiveness of gold nanocages to GNSs and found that the gold nanocages demonstrated a higher PT efficiency.[54]

Carbon-based materials have also been studied for PTT, including carbon nanotubes (CNTs) and polymers. Liu *et al.* demonstrated *in vitro* photothermal ablation of cancerous cells by selective targeting using PEGylated single-walled carbon nanotubes (SWNT) conjugated with folic acid as the PT agent.[55] The PT agents were irradiated at 808 nm and a power density of 2 W/cm^2.[55] Moon *et al*. reported that PEG-functionalized single-walled carbon nanotubes (SWNT) have a strong absorbance in the NIR region.[56] The PEG-SWNTs suspended in fetal bovine serum produced a temperature change greater than 60 °C at a concentration of 140 mg/mL when irradiated at a power density of 3.8 W/cm^2 for 10 min.[56] *In vivo* studies were conducted in mice bearing human

epidermoid mouth carcinoma KB tumor cells; the PEG-SWNTs were injected intratumorally at a concentration of 120 mg/L.[56] A significant decrease in tumor volume was observed after 20 days of treatment compared to the tumors that were irradiated without PEG-SWNTs. Gosh *et al*. coated multi-walled carbon nanotubes (MWNTs) with DNA and demonstrated PT ablation by injecting DNA-MWNTs at a concentration of 500 μg/mL intratumorally, followed by excitation using 1064 nm laser at a power density of 2.5 W/cm^2.[57] The irradiated xenograft tumors, grown from PC3 (human prostate cancer) cells, were completely eliminated; in comparison, tumors without DNA-MWNTs that were irradiated showed no decrease in the tumor size.[57] Robinson *et al*. conducted side-by-side experiments comparing SWNTs and GNRs and found that tumor elimination was achieved with concentrations of SWNTs one-tenth that of GNRs at a laser power of 2 W/cm^2.[58] The major limitation of CNTs transitioning from the lab to the clinical setting is the unknown long-term toxicity of these materials. Although several reports suggest that carbon nanotubes that are properly functionalized and coated are nontoxic, further pre-clinical toxicity studies on the carbon nanomaterials must be conducted to determine long-term effects on the human body.[59]

2.5 Electroactive Polymers in photothermal therapy

More recently, polymeric materials that exhibit a strong absorbance in the NIR region have been explored as PT agents. Specifically, conductive polymers are of interest in this area. Conductive polymer nanoparticles that have a strong absorbance in the NIR region have been studied as PT agents for PTT. The majority of the work involving conductive polymers as PTT agents has been demonstrated by Liu and coworkers.[60–62] Polypyrrole (PPy) was one of the first reported conductive polymers to be used in PTT.

PPy nanoparticles were synthesized in aqueous media in the presence of poly(vinyl alcohol) as the stabilizing agent. The study determined that PPy nanoparticles generated a temperature change of ≈ 45 °C at 1 mg/mL when irradiated with an 808-nm laser at a power density of 0.5 W/cm^2.[60] *In vitro* studies determined the effectiveness of the nanoparticles as photothermal agents. In this study, 4T1 (human breast cancer) cells were irradiated for 5 min at 1 W/cm^2 in the presence of nanoparticles.[60] Cell death was observed at concentrations as low as 0.025 mg/mL.[60] Poly(3,4-ethylenedioxythiophene):poly(styrenesulfonate) (PEDOT:PSS), a conductive colloidal suspension that will be discussed in detail in Chapter 3, has also been reported as a potential PTT agent by Liu *et al*.[61] In this study, commercial PEDOT:PSS was surface-modified with PEG using layer-by-layer deposition. This was accomplished by first coating the negatively charged particles with positively charged poly(allylamine hydrochloride) followed by coating with negatively charged poly(acrylic acid). The two layers are then crosslinked by amide bond formation, followed by conjugation of PEG to the surface of the nanoparticle yielding PEDOT:PSS:PEG nanoparticles with a diameter of 130 nm. Nanoparticles at 0.1 mg/mL demonstrated a heat change of ≈ 50 °C when irradiated at 808 nm with a power density of 1 W/cm^2.[61] *In vivo* studies determined that the PEDOT:PSS-PEG nanoparticle suspension injected in 4T1-tumor bearing mice enabled complete tumor elimination after PT treatment.[61] The potential of using conductive polymers as PT agents has shown to be effective, but there is still the potential for improvement.

By modifying the backbone of the conductive polymers one can control the absorbance of the material. The absorbance of PEDOT:PSS is very broad, which may

translate to lower PT conversion efficiencies. Also, conductive polymers as PT agents are relatively new compared to gold nanoparticles and have not been fully characterized. Characteristics such as the PT conversion efficiencies, degradation over several irradiation cycles, cell uptake, and cell death mechanism induced by irradiation with these types of nanoparticless is still not well understood. Lastly there are only a handful of commercially available conductive polymer colloidal suspensions. If modifications are made to the backbone of the polymer, a nanoparticle preparation route will also have to be determined. This is a challenge because conductive polymers are poorly processable and pose several challenges during preparation.

In this study we will describe the synthesis of extended conjugation 3,4-ethylenedioxythiophene derivatives. Preparation of nanoparticles with these materials by emulsion polymerization, and the optimization of this method to yield spherical nanoparticles with a strong absorbance in the NIR region will be discussed. The photothermal heating and conversion efficiencies will also be described and compared to commercial PEDOT:PSS and GNRs. Cytotoxicity studies of the colloidal suspensions will also be investigated in an effort to determine the highest loading concentration that results in more than 80% cell viability. Lastly, the *in vitro* photothermal ablation of the of breast cancer cells will be discussed.

3 SYNTHESIS OF 1,4-BIS(3,4-ETHYLENEDIOXYTHIENYL)-2,5-DIALKOXYBENZENES

3.1 Introduction

This chapter focuses on the structural modification of bis-EDOTbenzenes to fine-tune the absorption spectra of the polymers for use as PTT agents. The effect of alkoxy, alkoxy ester, and carboxylic ester substituents on electronic and optical properties is examined and the effect of polymerization method on polymer properties is discussed. The monomers discussed in this chapter were synthesized using Negishi coupling. Previously, Irvin and co-workers reported alkoxy-substituted bis-EDOT benzene monomers that were synthesized using Negishi coupling, as well as polymers that were synthesized both chemically and electrochemically.[63] Negishi coupling is a transition metal-mediated coupling reaction that forms bonds between two aromatic carbons.[64] This process has many advantages, including the use of organozinc intermediates, which are less toxic and tend to have higher reactivity than organometallics used in other coupling reactions.[64,65] Organozinc compounds are also compatible with a wide range of functional groups on the organohalides.[64] In the Negishi coupling reaction, an organohalide and organometal are coupled through the use of a palladium (0) catalyst.[64] In the work presented herein, this cross-coupling method is utilized in the synthesis of 1,4-dialkoxy-2,5-bis(3,4-ethylenedioxythienyl) benzene (BEDOT-B$(OR)_2$) monomers. These monomers can then be easily polymerized electrochemically or chemically. The resultant polymers are promising candidates for use in biomedical applications.

3.2 Background of Conducting Polymers

Electroactive polymers are a promising class of materials that can be used to meet quickly evolving technologies and the demand for more efficient and lighter materials. Electroactive polymers, also known as conductive polymers, are fully π–conjugated materials that can undergo oxidation/reduction processes resulting in changes in their properties including conductivity, reactivity, morphology and color. This reversible process can occur through chemical stimulation or through external energy such as an applied voltage.[66] This class of polymers has several advantages over inorganic semiconductors and metal oxide materials due to ease of synthesis, processing, and surface functionalization, as well as flexibility and lower weight.[67–69] Polyaniline (PANI), polypyrrole (PPy), and polythiophene (PT), Figure 3-1, are among the most common conductive polymers, and their properties have been well defined.

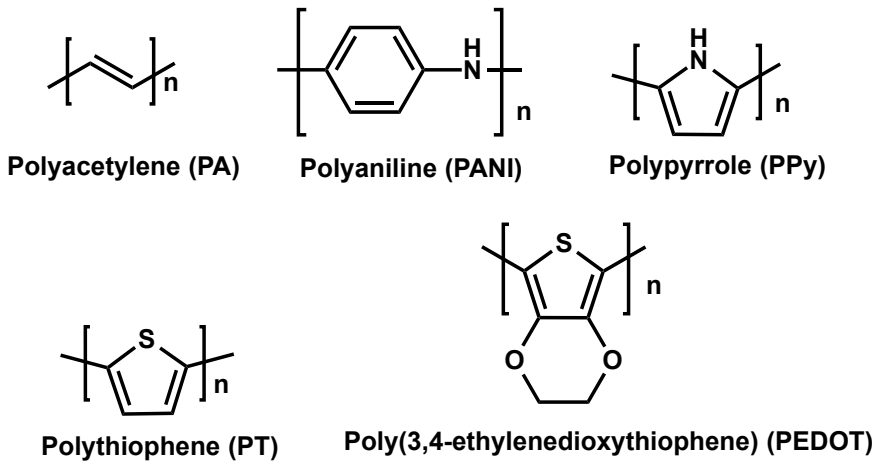

Figure 3-1. Chemical structures of common conductive polymers

In the 1950s the first conductive polymer (CP) was synthesized when pyrrole was polymerized electrochemically.[70] Bolto first reported the electronic properties of polypyrrole in 1963.[71] At the time there was limited knowledge about the material, and many years elapsed before interest in this polymer was rekindled. In 1977 Heeger demonstrated seven orders of magnitude increase in conductivity of polyacetylene (Figure 3-1) when doped with iodine.[72] It was concluded that charge transfer complexes are formed between polyacetylene and the dopant (halogens or iodine), possibly due to the formation of kinks, as a result of the cis-trans configuration.[72] This was the first step towards an understanding of the significance of CPs and their capabilities. Polyacetylene has many limitations, such as high chemical instability in air.[73] By adding nitrogen or sulfur atoms to the conjugated system, stability is added to the polymer.[74,75] Polyheterocycles such PANI, PPy, and PT have been investigated due to their stability and conductivity. These materials gained popularity in the 1980s, but at the time it was difficult to envision practical applications of these materials due to their brittleness. In order to overcome this problem, conductive polymers were blended with non-conductive polymers. These blends become conductive when the concentration of the conductive polymer exceeds a threshold point.[75]

Currently there are many know applications of CPs in a variety of different fields. One of the largest applications for CPs is use as coatings for metals as anticorrosive protection.[73] Conductive polymers are also used as electrically conductive transparent coatings for anti-static applications, rechargeable batteries, electrochemical capacitors, solar cells, and light emitting diodes (LEDs).[4]

3.3 Synthesis of Conductive Polymers

The synthesis of CPs can be accomplished by chemical polymerization or electrochemical polymerization. Most conductive polymers can be prepared via chemical oxidative polymerization as shown in Figure 3-2. In this method, oxidation of the monomer is initiated by either an organic or inorganic oxidizing agent such as an Fe(III) salt. In this process a resonance-stabilized radical cation site is formed on the monomer, which then couples to a another radical cation to form a dicationic dimer.[76,77] This process is repeated until polymer is formed. The oxidation potential of the monomer is determined by the ionization potential and electron affinity of the molecule.[77]

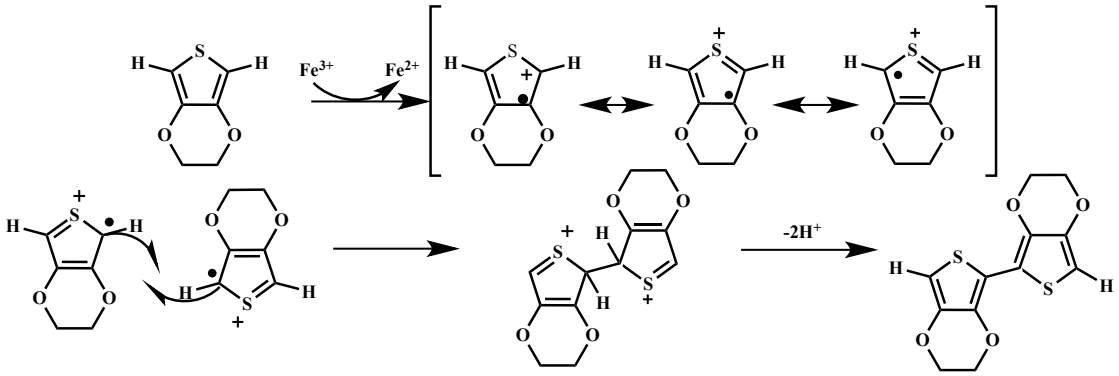

Figure 3-2. Oxidative polymerization

Electrochemical synthesis is a straightforward procedure that is used to produce thin film CPs. This was first performed by exposing a solution of monomer to an oxidant, resulting in precipitation onto a platinum electrode.[74] More recently electrochemistry is accomplished by using a three-electrode configuration (working, counter, and reference) in a solution of monomer and electrolyte (Figure 3-3). Current is passed through the solution, and electrodeposition occurs at the positively charged electrode, or anode.

Monomer molecules at the electrode surface undergo oxidation, forming radical cations that react with neutral monomer or other radical cations forming insoluble polymer chains on the surface of the electrode (as shown in Figure 3-2). Deposition time and temperature, concentration, solvent, electrolyte, electrode materials, and deposition charge are all factors that need to be considered. These parameters affect morphology, mechanical properties, and conductivity, which all affect the performance of the material. Some advantages of this approach are the production of thin films, entrapment of molecules, simultaneous doping, and synthetic ease. One limitation is that this is not an easily scalable process.[78]

The significant difference between chemical and electrochemical synthesis is the quantity of production. Electrochemical polymerization typically produces a thin film on the order of 20 nm. In chemical polymerization, bulk polymer can be synthesized. All CPs can be synthesized chemically, but not all can be synthesized electrochemically. Electrochemical polymerization of CPs is limited to monomers that can be oxidized in the presence of an electrochemical potential to form radical intermediates.[73]

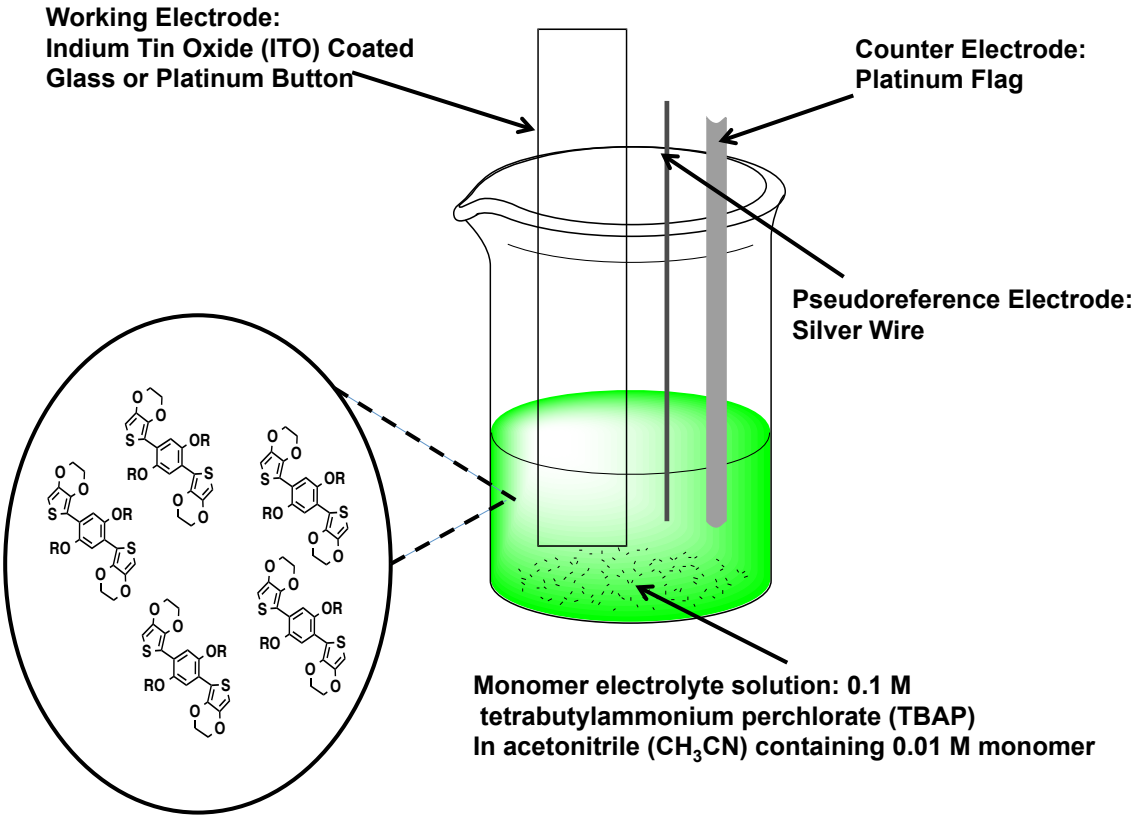

Figure 3-3. Schematic of electrochemical cell

3.4 Doping of Conductive Polymers

Most organic polymers lack intrinsic charge carriers. The charge carriers for CPs can be provided by partial oxidation (p-doping) of the polymer chain by electron acceptors such as iodine, forming positive charges (holes) along the chain. Alternatively, partial reduction (n-doping) can be accomplished using electron donors such as sodium, forming negative charges (electrons along the chain). These doping processes create charge defects that include polarons and bipolarons, which are then available to be the charge carriers.[79] The doping-induced changes in electronic structures can be understood using band theory. Small molecules like ethylene have discrete energy levels (Figure 3-4): the highest occupied molecular orbital (HOMO) and the lowest unoccupied molecular

orbital (LUMO). The difference in energy (the band gap) between the HOMO and the LUMO is large in ethylene; the difference is slightly smaller in butadiene, due to resonance stabilization. As more and more double bonds are in conjugation with each other (as in the oligomer in Figure 3-4), the amount of resonance stabilization increases, and the energy gap decreases. Eventually, as more and more conjugation is present in a molecule (as in polyacetylene), the discrete energy levels combine to form bands. The highest occupied band is the valence band, and the lowest unoccupied band is the conduction band. The difference between the two is known as the band gap (E_g), Figure 3-4.[70,73,75] The band gap is the amount of energy required to promote an electron from the valence band to the conduction band. Band gap can be determined spectroscopically from the absorption spectrum of a conducting polymer.[63]

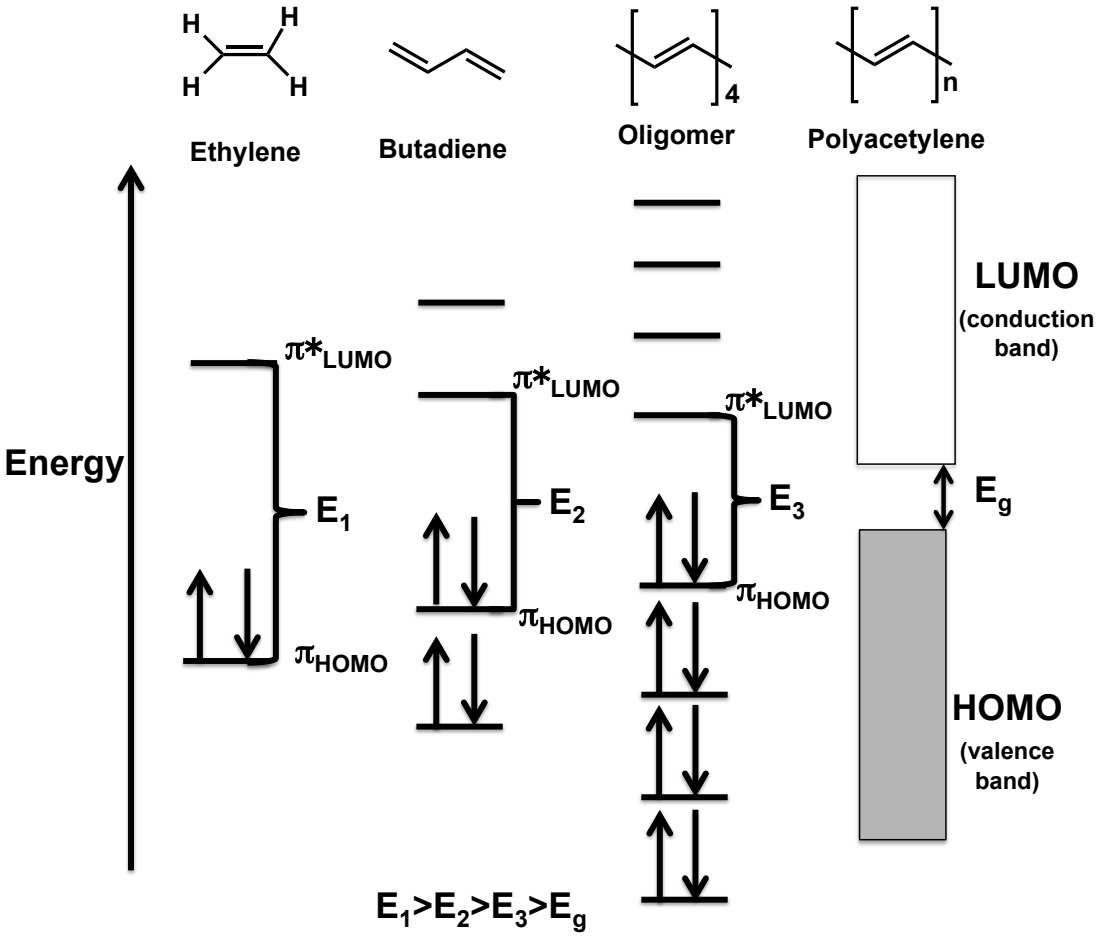

Figure 3-4. Molecular energetics as conjugation is increased for polyacetylene

Resonance stabilization in conducting polymers makes it possible to easily remove electrons from the valence band of the neutral polymer. When one electron is removed, a radical cation (polaron) of the polymer is formed. When a second electron is removed, the polaron is converted to a bipolaron (dication) shown in Figure 3-5. The charges are delocalized along the polymer chain, which typically supports one positive charge for every three to five rings.

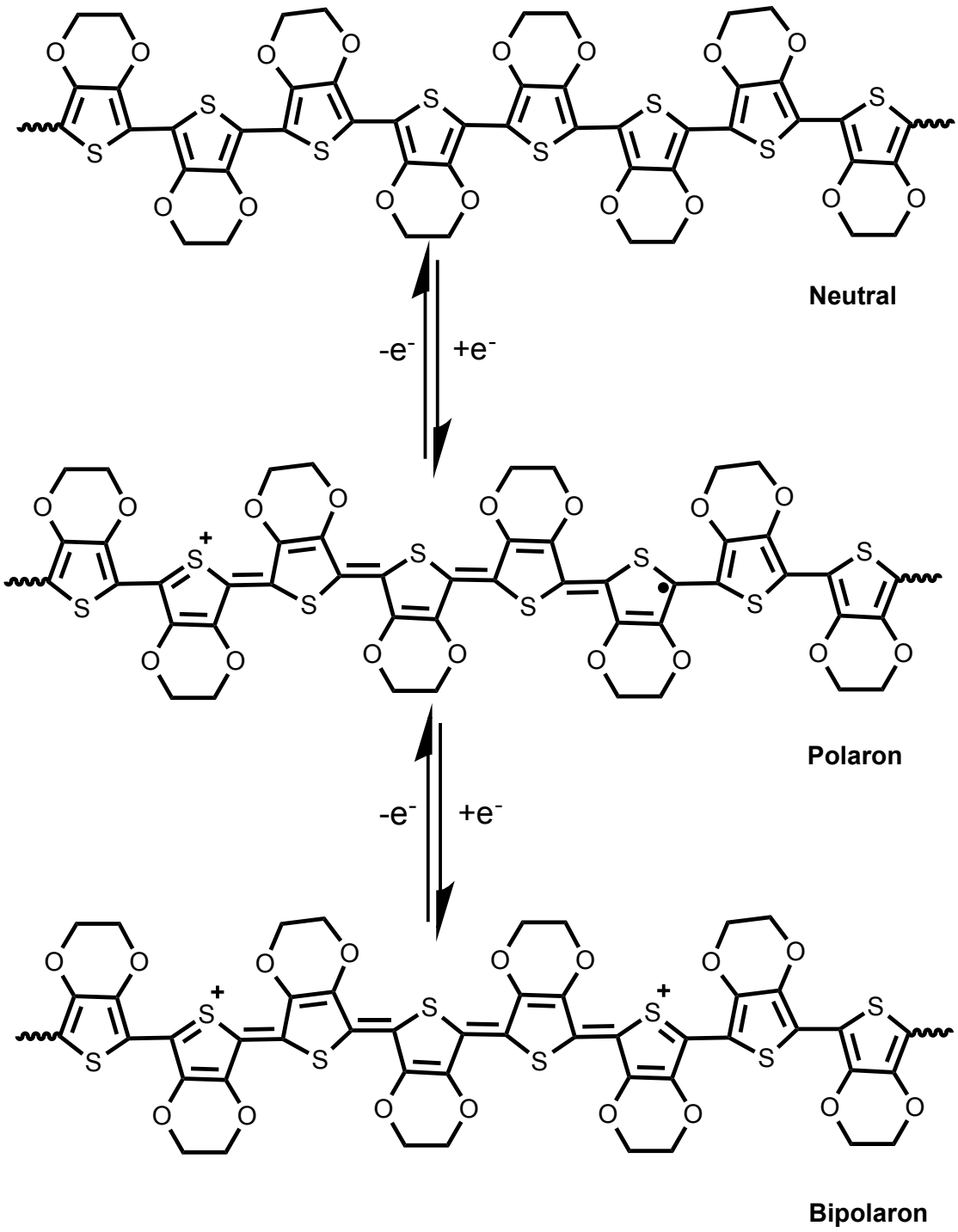

Figure 3-5. Conversion between neutral, polaron, and bipolaron in poly(3,4-ethylenedioxythiophene)

In an effort to create more stable materials with better conductivity and electrochemical properties, modifications to these electroactive polymers have been performed. These modifications allow for different conductivities, oxidation potentials, mechanical properties, and color-tuning. Among these derivatives, poly(3,4-ethylenedioxthiophene) (PEDOT), a derivative of polythiophene, has gained attention for several reasons. PEDOT has demonstrated high electrochemical stability compared to polythiophene and other thiophene derivatives. It also has demonstrated higher conductivity than polythiophene, and it is nearly transparent when in the oxidized state.[80] There are many proposed applications for electroactive polymers ranging from electrochromics to biomedical devices due to their rapid switching times, tunability, durability, and lightness.[78,81] Applications in electrochromic devices include glare-reduction systems for buildings, automobiles, sunglasses, protective eyewear, optical storage devices, and smart textiles.[68] Smart windows can reduce energy requirements by blocking specific wavelengths of light on–demand and protecting interiors of homes and automobiles.[68] Electroactive polymers have also been explored for use in medical devices. For example, these types of polymers are commonly used as transducers in biosensor devices.[82] Applications in therapeutic delivery have also shown promise; studies have demonstrated the release of drugs and therapeutic proteins.[83–85] More recently, electroactive polymers have been used as therapeutic agents in photothermal therapy.[60,61]

In photothermal therapy the therapeutic agents must absorb light in the optical window (700 – 900 nm) also known as the therapeutic window; in this range light has the maximum depth of penetration in tissue, typically between 0.5 to 1 cm.[36] This depth is

due to the fact that biological chromophores such as hemoglobin, oxigenated hemoglobin, lipids, and water have little to no absorbance in this region. When these photothermal agents absorb light in this therapeutic window, the photoenergy is converted to photothermal energy.

3.5 Experimental

3.5.1 Materials

3,4-Ethylenedioxythiophene (EDOT) was purchased from VWR and purified as described previously.[86] Anhydrous tetrahydrofuran (THF) and anhydrous acetonitrile were purchased from Acros Organics and used as received. Tetrabutylammonium perchlorate (TBAP) was purchased from VWR, recrystallized from ethyl acetate, and dried under vacuum for 24 h prior to use. n-Butyllithium (nBuLi, 2.5 M in hexanes) was titrated as described by Hoye *et al.* 48 h prior to use to determine the actual concentration.[87] Hydroquinone, bromine, 1-bromohexane, ethyl 4-bromobutyrate, anhydrous hydrazine, tributyltin chloride, and iron (III) chloride were purchased from Sigma Aldrich and used as received. Ethyl acetate, dichloromethane, chloroform, hexane, acetone, anhydrous *N,N*-dimethylformamide (DMF), hydrochloric acid, and magnesium sulfate ($MgSO_4$) were purchased from Fisher Scientific and used as received. Potassium carbonate (K_2CO_3), potassium iodide (KI) and potassium fluoride (KF) were purchased from VWR and dried at 100 °C overnight prior to use. The salts were ground prior to drying using a coffee grinder.

3.5.2 Structural identification and spectroscopic characterization

Structural identification was accomplished using nuclear magnetic resonance (NMR) spectroscopy and ultraviolet-visible-near infrared (UV-Vis-NIR) spectroscopy. Solutions of the products were analyzed using ^{1}H NMR and ^{13}C NMR spectroscopy with a Bruker Avance 400 MHz NMR Spectrometer.

3.6 Synthesis

3.6.1 Monomer Synthesis

3.6.1.1 Synthesis of 1,4-dihexyloxybenzene (1)

The synthesis of compound 1 was carried out following a procedure similar to that reported by Ko *et al.*[88] A solution of KOH (14 g, 0.25 mol) in ethanol (40 mL) was added to a solution of hydroquinone (12.5 g, 0.114 mol) in THF (42 mL) at room temperature with stirring under positive argon flow. The solution was stirred at room temperature for 1 hour, and then 1-bromohexane (35 mL, 0.25 mol) was added to the reaction flask. The mixture was stirred at reflux for 24 h under argon. The reaction was cooled to room temperature and washed several times with water. The organic layer was isolated, dried over $MgSO_4$, filtered, and concentrated under reduced pressure to yield 1,4-dihexyloxybenzene as a white solid. Recrystallization from methanol yielded a white crystalline solid [80% yield]. ^{1}H NMR ($CDCl_3$, 6.89 (s), 4.06 (t), 1.76 (q), 1.48 (m), 1.31 (m), 0.90 (t) ppm): [lit. (Ko et al.[88]) ^{1}H NMR ($CDCl_3$, 6.82 (s), 3.90 (t), 1.80-1.73 (q), 1.47-1.30 (m), 0.90 (t) ppm].

3.6.1.2 Synthesis of 1,4-dibromo-2,5-dihexyloxybenzene (2)

Compound 2 was synthesized following a procedure similar to that reported by Umezewa *et al*.[89] Compound 1 was dissolved in dichloromethane with stirring under argon, the reaction flask was cooled to 0 °C, and bromine (4.65g, 0.029mol) was added dropwise. An outlet adapter was connected to poly(vinyl chloride) tubing fitted with an inverted glass funnel. The funnel was suspended over a beaker containing 6 M aqueous sodium hydroxide. This trap was necessary to neutralize bromic acid fumes produced during the reaction. The reaction was allowed to proceed for 5 h at 0 °C. The reaction mixture was washed three times with water. After the last wash, the organic layer was dried over $MgSO_4$ and filtered through paper. The solvent was evaporated under reduced pressure, and the resultant solid was then purified by recrystallization from ethyl acetate to yield (2) as a white solid [65% yield]. ^{1}H NMR ($CDCl_3$, 7.17 (s), 4.03 (t), 1.76 (q), 1.48 (m), 1.31 (m), 0.90 (t) ppm): [lit. (Umezewa et al.[89]) ^{1}H NMR ($CDCl_3$, 7.09 (s), 3.95 (t), 1.80 (q), 1.51-1.46 (m), 1.37-1.32 (m), 0.90 (t) ppm)]

3.6.1.3 Synthesis of diethyl 1,4-bis(butanoyloxy) benzene (3*)*

Hydroquinone (2.5 g, 0.0187 mol) was combined with potassium iodide (1.88 g, 0.00935 mol) and potassium carbonate (15.69 g, 0.0933 mol) in DMF (25 mL) under argon. Ethyl 4-bromobutanoate (9.13 g, 0.0468 mol) was added, and the reaction mixture was heated at reflux for 3 hrs. DMF was removed under vacuum, and the product was resuspended in ethyl acetate and vacuum filtered. The filtrate was collected, and the ethyl acetate was removed under reduced pressure. The product was resuspended in dichloromethane and filtered through silica gel under vacuum. The filtrate was collected, and the dichloromethane was removed under vacuum. The resultant solid was then

purified by recrystallization from ethyl acetate to yield (3) as a white solid. [48% yield]. ^{1}H NMR ($CDCl_3$, (7.08 (s), 4.14 (q), 3.99 (t), 2.54 (t), 2.11 (p), 1.25 (t) ppm). ^{13}C NMR ($CDCl_3$, 173.3, 150.2, 118.8, 111.5, 69.3, 60.7, 30.9, 24.3, 14.4 ppm).

3.6.1.4 Synthesis of diethyl 4,4'-[(2,5- dibromo-1,4-phenylene)bis(oxy)]dibutanoate (4)

Compound 4 was synthesized following the same procedure for compound 2 using 1,4-bis(ethylbutanoyloxy)benzene (5.00 g, 0.015 mol) and bromine (4.61 g, 0.028 mol), resulting in a white solid after recrystallization from ethyl acetate. [60% yield]. ^{1}H NMR ($CDCl_3$,(7.08 (s), 4.14 (q), 3.99 (t), 2.54 (t), 2.11 (p), 1.25 (t) ppm). ^{13}C NMR ($CDCl_3$, 173.3, 150.2, 118.8, 111.5, 69.3, 60.7, 30.9, 24.3, 14.4 ppm).

3.6.1.5 Synthesis of 1,4-bis[2-(3,4-ethylenedioxy)thienyl]-2,5-hexyloxybenzene (M1)

nBuLi (0.0669 mol) was added slowly to a solution of EDOT (0.0669 mol) in THF (50 mL) at -78^{o}C under argon. The yellow solution was allowed to stir for 1 h. $ZnCl_2$ (0.0639 mol) in THF was then added to the lithiated EDOT. The mixture was stirred for one hour at 0 °C under argon. Compound 2 (0.0167 mol) and $Pd(PPh_3)_4$ (8.65 X 10^{-5} mol) were added to the resulting EDOT-ZnCl. The yellow solution was stirred at reflux for 5 days under argon. It was cooled to ambient temperature and quenched by pouring into 1 M HCl. Dichloromethane was added to the solution, forming two layers. The organic layer was separated and dried over $MgSO_4$, filtered through paper, and concentrated under reduced pressure. The product was purified by recrystallization from 3:1 ethanol:benzene solution. [48% yield] ^{1}H NMR (C_6D_6, 8.1 (s), 6.45 (s), 4.03 (t), 3.58 (m), 1.76 (p), 1.48 (p), 1.31 (m), 0.90 (t) ppm) ^{13}C NMR (C_6D_6, ppm)

3.6.1.6 Synthesis of diethyl 4,4'-{[2,5-bis(2,3-dihydrothieno[3,4-b][1,4]dioxin-5-yl)-1,4-phenylene]bis(oxy)}dibutanoate (M2)

Monomer 2 (M2) was prepared according to the procedure described for M1 where compound 3 (5.00g, 0.010 mol) and $Pd(PPh_3)_4$ (8.65 X 10^{-5} mol) were added to the EDOT-ZnCl solution. [62% yield] ^{1}H NMR ($CDCl_3$ 7.68 (s), 6.47 (s), 4.32 (m), 4.14 (m), 2.54 (t), 2.11 (p), 1.25 (t) ppm) ^{13}C NMR ($CDCl_3$ 173.6, 149.3, 142.1, 139.4, 121,5, 114.0, 113.5, 99.9, 69.2, 65.5, 60.8, 31.6, 25.4, 14.7 ppm)

3.6.1.7 Synthesis of 1,4-dihexyl 2,5-dibromoterephthalate

2,5-Dibromoterephthalic acid (3 g, 0.00926 mol) was dissolved in 1-hexanol (12.20 g, 0.118 mol) with stirring under argon. Concentrated H_2SO_4 (1 mL) was added to the reaction, and the flask was fitted with a soxhlet extractor packed with 4 Å molecular sieves to absorb water. The reaction mixture was heated at reflux for 48 h, allowed to cool to room temperature, and washed with water and then with brine. The organic layer was dried over $MgSO_4$, filtered through paper, and concentrated under reduced pressure. The resultant solid was recrystallized from ethyl acetate to yield a white solid. [55% yield]. ^{1}H NMR (CD_2Cl_2, 8.03 (s), 4.35 (t), 1.80 (p), 1.42 (p), 1.31 (m), 0.92 (t) ppm) ^{13}C NMR (CD_2Cl_2, 165.7, 138.2, 121.1, 64.6, 31.7, 25.5, 22.7, 14.1 ppm)

3.6.1.8 Attempted synthesis of dihexyl 2,5-bis(2,3-dihydrothieno[3,4-b][1,4]dioxin-5-yl) terephthalate

Negishi Coupling

The reaction was carried out following the procedure for M1 and M2, with compound 5 (5.00 g, 0.01 mol) and $Pd(PPh_3)_4$ (8.65 X 10^{-5} mol) added to EDOT-ZnCl.

After 5 days of refluxing the reaction was not fluorescent and after doing ^{1}H NMR revealed only starting materials with no indication of the coupled product.

Stille Coupling

EDOT lithiation was carried out as previously discussed for M1 and M2. $SnBu_3Cl$ (10.64 g, 0.0327 mol) was added to the lithiated EDOT and reacted for 1 h at room temperature under argon. Compound 5 (5.00 g, 0.01 mol) and $Pd(PPh_3)_4$ (8.65×10^{-5} mol) was added to the resulting EDOT-$SnBu_3$. The brown orange solution was stirred at reflux for 5 day, and the reaction was quenched by adding 1 M HCl and 3 M KF. Dichloromethane was added to the reaction to separate the organic layer, which was then dried over $MgSO_4$, filtered and concentrated under reduced pressure.

3.6.2 Electrochemistry

Electropolymerizations were carried out in an argon atmosphere using 0.01 M monomer and 0.1 M TBAP. The solvent used to prepare the solutions was an 80:20 mixture of dichloromethane to acetonitrile in the case of M1 and acetonitrile in the case of M2. The mixture of the solvents was required for polymerization of M1 because of the poor solubility of the monomer. The working, auxiliary, and reference electrodes were a platinum button (2 mm^2), a platinum wire, and an Ag/Ag^+ reference electrode, respectively. The Ag/Ag^+ wire is a pseudoreference electrode that was calibrated to ferrocene/ferrocenium (Fc/Fc^+) redox system.[90] In these experiments Ag/Ag^+ wire was calibrated separately using 1.5 mM solution of Fc/Fc^+. Five cycles were used each time to deposit the polymer on the working electrode. The polymer was then rinsed with 0.1 M TBAP/acetonitrile and placed in 0.1 M TBAP/acetonitrile. Cyclic voltammetry of the

polymerized films on the working electrode was accomplished using monomer-free 100 mM TBAP in acetonitrile as the electrolyte system at scan rates ranging from 50 to 400 mV/s.

3.6.3 UV-Vis-NIR Spectroscopy

For spectroscopic characterization, the working electrode was changed to indium tin oxide (ITO) coated glass (Delta Technologies 5-15 Ω). The counter electrode was a platinum wire, and silver wire was used as a pseudo reference electrode. To prepare samples for the UV-Vis-NIR spectroscopy, the conditions described in 3.5.5 were used, except that the films deposited onto the ITO glass were kept at a constant potential of +0.50 V vs. Ag wire for 1 min, leaving the film in the oxidized state for initial spectroscopic characterization. Spectral data of oxidized films were collected. Once deposited onto the ITO slides, the films were washed several times and scanned using BioTek Synergy H4 Hybrid Reader. The absorbance was measured from 300−1000 nm. The oxidized polymer film was then dipped into anhydrous hydrazine for 5 min, reducing the polymer back to the neutral state. The color of the film changed from blue to red. The spectra of the reduced films were then acquired. The band gaps of the polymers were determined from the onset of the π to π* transition (the intercept of the tangent of the lower energy side of the absorption curve).

3.7 Results and Discussion

3.7.1 Monomer Synthesis

1,4-Hexyloxybenzene (1) was prepared by etherification of hydroquinone in the presence of KOH and ethanol in THF. The white crystalline product was recovered in 80

% yield. Using 1,4-dihexyloxybenzene, compound 2 was synthesized through a bromination reaction in CH_2Cl_2. Compound 3 was prepared by esterification of hydroquinone in the presence of KI and K_2CO_3 in DMF. The white crystals were collected by filtration and recovered at 48% yield. Diethyl 4,4'-[(2,5- dibromo-1,4-phenylene)bis(oxy)]dibutanoate (compound 4) was prepared via bromination of compound 3.

Preparation of M1 and M2 was accomplished by coupling EDOT-ZnCl to compounds 2 and 4 using $Pd(PPh_3)_4$ as the catalyst. Prior to lithiation of EDOT, the exact concentration of nBuLi was determined via titration. The synthesis scheme is shown in Figure 3-7 EDOT was lithiated by the addition of nBuLi under constant argon flow. The reaction was carried out for 1 h at -78 °C. After 1 h of stirring, the reaction changed from having no color to being transparent yellow. Following 1 h of stirring, the reaction temperature was raised to 0 °C, and $ZnCl_2$ was added. The reaction was carried out for an additional 1 h. After 1 h of reacting, the color changed from transparent yellow to a transparent orange. After 1 h the ice bath was removed and the palladium catalyst and precursor, compound 2 or 4, were added to the reaction flask. The reaction was carried out for several days, and reaction progress was followed using TLC. Once the precursor was no longer visible in the TLC, the reaction mixture was worked up. The organic layer was collected and purified, resulting in yellow solids at 48% and 62% yield for M1 and M2 respectively. M1 and M2 were characterized with ^{1}H and ^{13}C NMR, see appendix for NMR data.

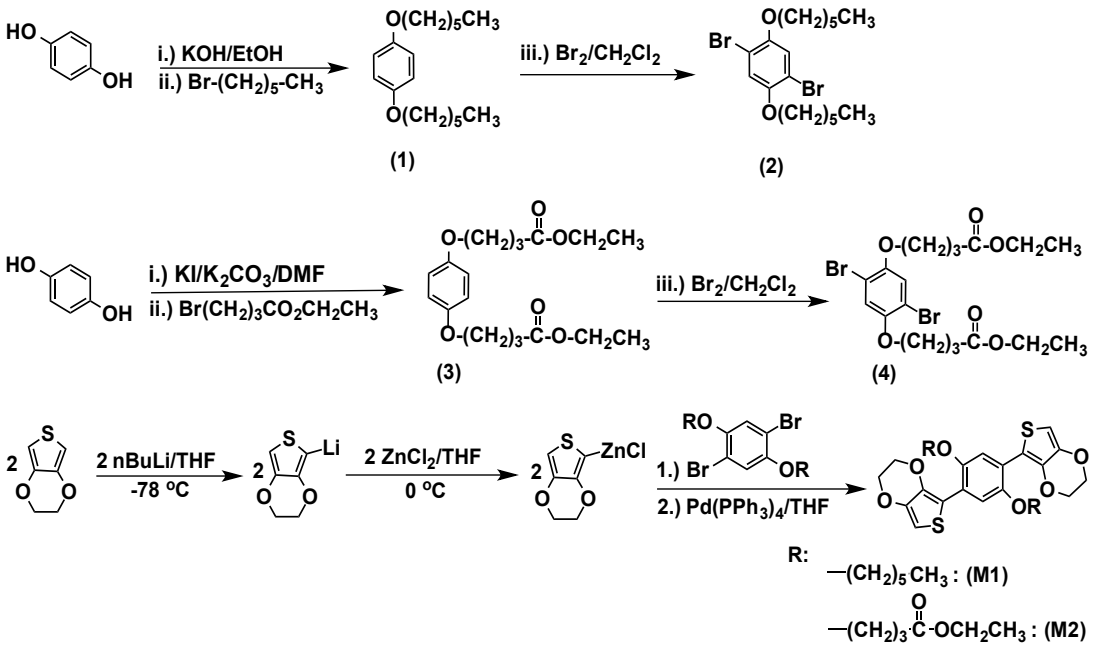

Figure 3-6. Synthesis of 1,4-bis(3,4-ethylenedioxythienyl)2,5-dialkoxybenzenes

Dihexyl 2,5-dibromoterephthalate, compound 5, was prepared by esterification of 2,5-dibromoterephthalic acid with 1-hexanol (Figure 3-7). The molecular sieves were changed periodically in order to absorb the water produced as a byproduct of the reaction. Compound 5 was purified and collected at 55% yield. NMR spectroscopy of the product was consistent with the anticipated structure. Two different approaches were then used in an attempt to couple EDOT to compound 5, as shown in Figure 3-7. Negishi coupling was first attempted following a similar procedure previously described for M1 and M2 synthesis. While the preparation of EDOT-ZnCl was accomplished similarly as before, the coupling reaction never occurred as evidenced by TLC and ^{1}H NMR. Both starting materials were evident, however, there was no evidence of the coupled product. In a second attempt to couple compound 5 to EDOT, Stille coupling was used. Stille coupling is also a palladium-catalyzed reaction; however, the carbon-carbon bond formation is accomplished by reacting an organohalides with organotin reagents.[91,92] The organotin

compounds are not as sensitive to moisture or oxygen, and the reaction can tolerate a variety of functional groups making the Stille reaction a more versatile process than Negishi coupling.[92] EDOT was lithiated as in the Negishi reaction; however, rather than adding $ZnCl_2$, $SnBu_3Cl$ was added, forming an EDOT-$SnBu_3$ complex. The EDOT-$SnBu_3$ was then reacted with compound 5 using a palladium catalyst. The reaction was allowed to proceed for 5 days and tracked by TLC. After 5 days the reaction was stopped by the addition of HCl and KF. The organic layer was collected and characterized. Based on the ^1H NMR, the reaction was unsuccessful showing only the starting material; additionally, the recovered oil was also not fluorescent. Fluorescence is a characteristic of extended conjugation monomers.

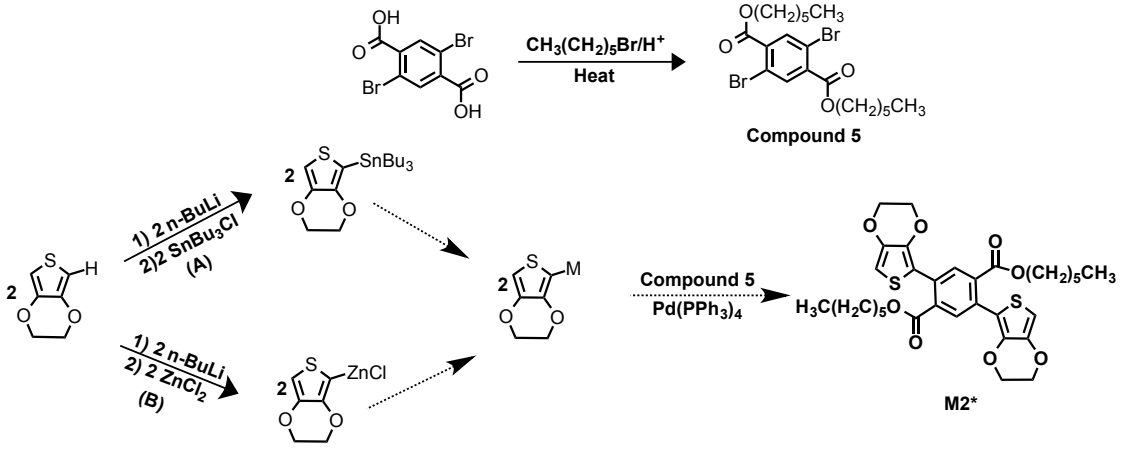

Figure 3-7. Attempted synthesis of dihexyl 2,5-bis(2,3-dihydrothieno[3,4-b][1,4]dioxin-5-yl) tetrephthalate **(A)** Stille coupling and **(B)** Negishi coupling

3.7.2 Electrochemical analysis and electropolymerization

Monomers M1 and M2 were electrochemically polymerized, Figure 3-8. Monomer M2 was electrochemically polymerized in an argon atmosphere using a 0.01 M monomer and 0.1 M TBAP in CH_3CN. For monomer M1, a mixture of CH_3CN and CH_2Cl_2 at 20:80, respectively, was required due to poor solubility of the monomer in

CH_3CN. Previously synthesized BEDOT-$B(OR)_2$ monomers reported similar poor solubility in CH_3CN, and a mixture of CH_3CN and CH_2Cl_2 at different ratios were required for electrochemistry.[63] Figure 3-9 shows the repeated potential scanning electropolymerization of the monomers, with a total of 5 scans used for each deposition.

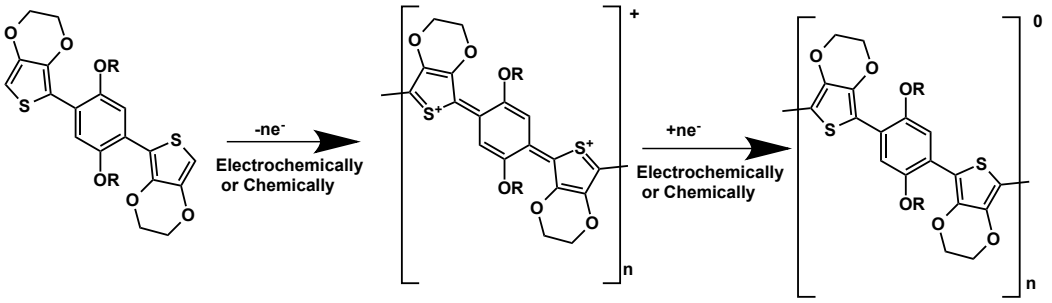

Figure 3-8. Oxidative polymerization of 1,4-bis(3,4-ethylenedioxythienyl)-2,5-dialkoxybenzene and subsequent re-neutralization.

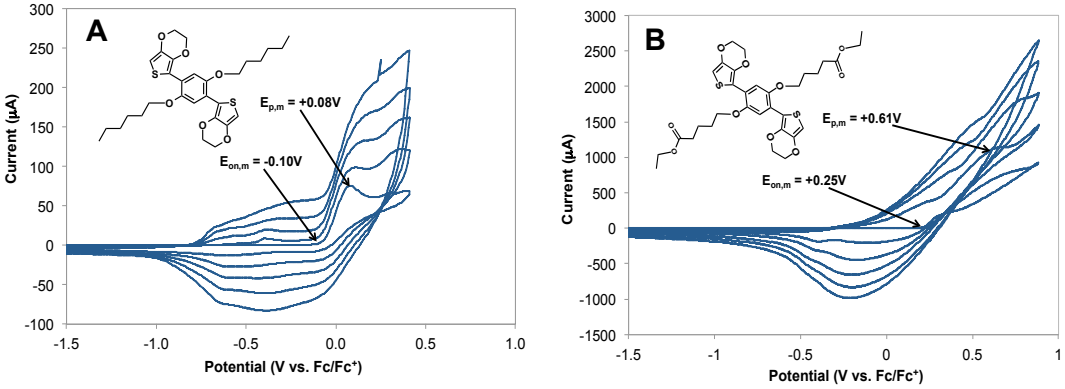

Figure 3-9. Electropolymerization of M1 (0.01 M) (A) and M2 (0.01 M) (B) at 100 mV/s in 0.1 M TBAP in CH_3CN/CH_2Cl_2 (20:80) for M1 and 100 mV/s in 0.1 M TBAP in CH_3CN for M2.

Initially, there is no current response for M1 until a higher potential is reached, indicating the onset of the monomer oxidation ($E_{on,m}$) which occurs at -0.10 V with the peak oxidation of the monomer ($E_{p,m}$) occurring at +0.08 V. During the first scan, the

initial peak observed is indicative of irreversible oxidation of the monomer, which is polymerized onto the surface of the working electrode giving P1. During subsequent scans, an additional oxidation process is observed at lower potentials, due to the reoxidation of the polymer that is already deposited onto the working electrode during the previous cycles. The film deposited onto the working electrode is dark green when in the oxidized state and red in the neutral state. Compared to other heterocyclic polymers BEDOT-B$(OR)_2$ have relatively low oxidation potentials, as shown in Table 3-1. 1,4-Bis(3,4-ethylenedioxythienyl) benzene (BEDOT-B) was first reported to have a $E_{on,m}$ of +0.79 V and an $E_{p,m}$ of +0.83 V by Sotzing *et al.*[93] Several studies have shown that by adding alkoxy chains as pendant groups the oxidation potential is increased compared to that of BEDOT-B. Specifically, research performed by Irvin *et al.*[94] shown in Table 3-1, demonstrates that as the alkoxy groups are extended the $E_{on,m}$ and $E_{p,m}$ are increased; however, M1 does not follow a similar trend. M1 has a very low oxidation potential compared to the diheptyltoxy and even dimethoxy BEDOT-B derivatives. This difference in the monomer oxidation potential observed between the hexyloxy and heptyloxy may be explained by the odd-even effect. The odd-even effect is an alteration in the materials structure or properties based on the odd or even number of the substituents on the pendant group. The odd-even effect on the electrochemical properties of ω-(4'-methyl-biphenyl-4-yl)-alkanethiols (BP*m*) where *m*=1 – 6 was observed by Long *et al*.[95] It was determined that there was a potential difference on the order of 83 mV comparing the odd and even number of alkyl chains.[95] Potentially the hexyloxy molecule (M1) may have a higher magnitude of order and stability in comparison to the odd number heptyloxy molecule, lowering the oxidation potential of M1.

Table 3-1. Electrochemical Results for BEDOT-B(OR)$_2$ where R varies as shown in the first column

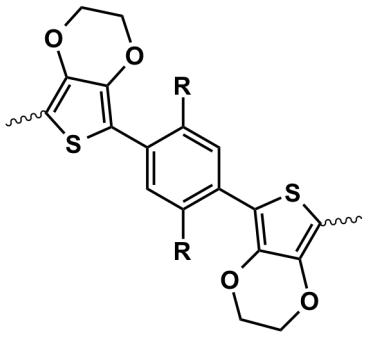

R (groups)	$E_{on,m}$ (V vs. Fc/Fc^+)	$E_{p,m}$ (V vs. Fc/Fc^+)	$E_{a,p}$ (V vs. Fc/Fc^+)	$E_{c,p}$ (V vs. Fc/Fc^+)	E_g (solid film) (eV)	E_g (solution) (eV)
OC_6H_{13}	-0.10	+0.08	-0.66	-0.88	2.1	2.1
$O(CH_2)_3COO$ CH_2CH_3	+0.25	+0.61	-0.02	-0.3	1.8	1.8
$OCOCH_3$ (OAc)[96]	+0.83	+0.93	+0.74	+0.64	1.8	N/A
H[93]	+0.79	+0.83	N/A	N/A	1.8	N/A
OCH_3[63]	+0.48	+0.64	-0.02	N/A	1.75	N/A
OC_7H_{15}[63]	+0.5	+0.65	-0.1	-0.18	1.95	N/A
$OC_{12}H_{25}$[63]	+0.56	+0.69	-0.07	-0.13	2.03	N/A
$OC_{16}H_{35}$[63]	+0.59	+0.84	-0.12	-0.22	N/A	N/A
F[98]	+1.01	+1.1	+0.86	+0.69	1.9	N/A

Figure 3-9 also shows the electropolymerization of M2, which has an $E_{on,m}$ at +0.25 V and a $E_{p,m}$ at +0.61 V. The film deposited onto the working electrode is P2 and was blue in the oxidized state and red in the neutral state. Compared to BEDOT-B the oxidation potential of M2 is much lower, perhaps due to electron donation from the alkoxy substituents in M2.

To our knowledge there have not been any EDOT-based monomers synthesized with R groups that have ester functional groups in the outer pendant group. In order to

understand the role the ester group has on the oxidation potential, our group attempted to synthesize M2* (Figure 3-7), but after several attempts we were unsuccessful. This may have been due to instability of the benzene ring during synthesis caused by the withdrawing nature of the ester group. However, in a study done by D. Irvin *et al.*[96] an EDOT-based monomer was synthesized with the carboxyl group directly on benzene ring yielding BEDOT-B(OAC)$_2$. BEDOT-B(OAc)$_2$ had an $E_{on,m}$ at +0.83 V and a $E_{p,m}$ of +0.93 see Table 3-1. Based on these results we can determine the role of an ester pendant group on the oxidation potential of the material. By having the ester group directly on the benzene ring the oxidation potential is increased compared to that of alkoxy pendant groups. However, when the ester group is further away from the backbone, the oxidation potential is reduced. While BEDOT-B(OAc)$_2$ slightly donates electrons to the backbone of the polymer, the ester group on P2 is farther away and free to interact with backbone while stacking occurs during polymerization. The stacking that occurs may lead to π- π^* interactions with the free carbonyl and the backbone of the polymer reducing the oxidation potential. The effect of removing electron density from the π system is evident in the energy difference required to oxidize the three different monomers as shown by their structures.

With repeated potential scanning, insoluble films of polymer P1 and P2 were deposited onto the electrodes. The increased current response observed with each scan is representative of the polymer film depositing onto the electrode with each cycle. After five cycles, films of P1 and P2 were washed in CH_3CN and placed in a monomer-free 0.1 M TBAP/CH_3CN solution. Cyclic voltammograms (CV) of the polymers were acquired between 50 to 400 mV/s as shown in Figure 3-10. The first peak observed in the CVs is

the anodic peak potential ($E_{a,p}$), and the peak observed as voltage is cycled back is the cathodic peak potential ($E_{c,p}$). A linear increase in the both $E_{a,p}$ and $E_{c,p}$ as a function of scan rate (as observed in the voltammograms of both polymers) is indicative of a film that is adhered to the electrode and electroactive.[77] The previously synthesized alkoxy monomers had relatively similarly low $E_{a,p}$ values that were below 0.0 V. $E_{a,p}$ values for P1 again did not follow the trend that was reported previously, and at 100 mV/s is significantly lower at -0.66 V with $E_{c,p}$ at -0.88 V. This decrease in oxidation potential of the P1 may again be attributed to an odd-even effect where the even number alkyl pendant group has more stability and is highly ordered. Polymer P2 again showed a linear increase in $E_{a,p}$ and $E_{c,p}$ values at -0.02 V and -0.3 V respectively, when cycled at 100 mV/s. By moving the ester group further from the conjugated backbone, the polymer oxidation potential was decreased when compared to poly(BEDOT-B$(OAc)_2$). Poly(BEDOT-B$(OAc)_2$), which has the ester group directly on the backbone, exhibits an increased $E_{a,p}$ value compared to alkoxy substituents groups. P2 has similar $E_{a,p}$ values to the alkoxy substituent groups, which indicates that once polymerized the ester linkage of the R group plays little to no role in the oxidation potential of the polymer. Instead, the ether linkage that is directly on the conjugated backbone is what dictates the oxidation potential of the polymer.

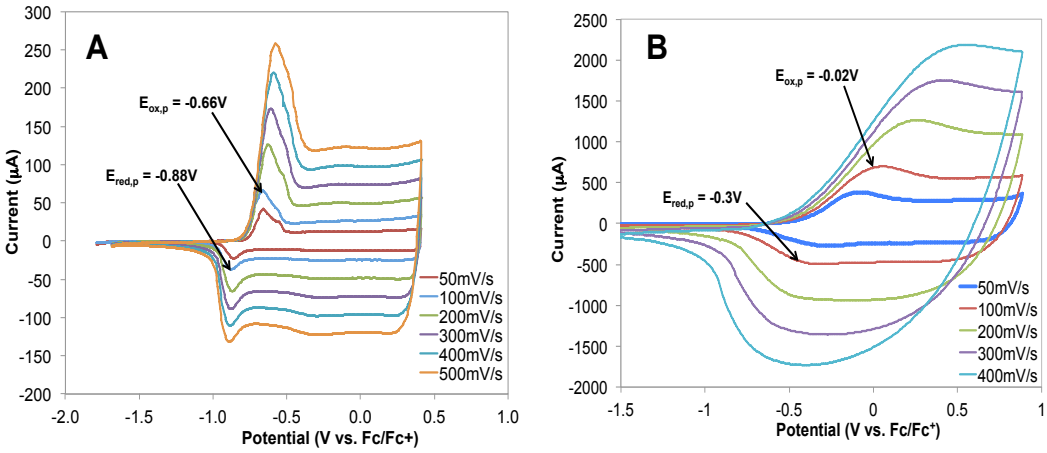

Figure 3-10. Cyclic voltammograms of polymer P1 (A) and polymer P2 (B) at 50-400 mV/s acquired in 0.1 M TBAP in CH_3CN.

3.7.3 Absorption Spectroscopy

UV-Vis-NIR was used to determine the absorbance spectra and band gaps of polymers P1 and P2. The measurements were performed using films of polymers electrochemically deposited on indium tin oxide ITO coated glass, and the polymerization was carried out at a constant potential of +0.50 V/s for 1 min. The films were washed several times with CH_3CN to remove excess monomer. The absorption spectra of the films were obtained from 300 – 1000 nm (Figure 3-11). The oxidized film of P1 was dark green in color and had a peak absorbance at 1.75 eV (708 nm), while P2 was dark blue in color with a peak at 1.56 eV (795 nm). A significant red shift in the absorbance is observed in both polymers when switching from the neutral state to the oxidized state. This shift is attributed to intermediate bands introduced by the dopant in the oxidized state.[97] When both P1 and P2 films are compared, the shift observed in the P2 UV-Vis-NIR spectra compared to P1 is due to the π-orbital of the C=O. With ability to bend and twist, the carbonyl pendant group may come into relatively close proximity

to the conjugated backbone, playing a role in reducing the energy required for the transition of electrons from the HOMO to the LUMO state. The oxidized polymer films were also compared to oxidized nanoparticle suspensions (prepared as discussed in Chapter 4), and there was no significant shift in the absorbance.

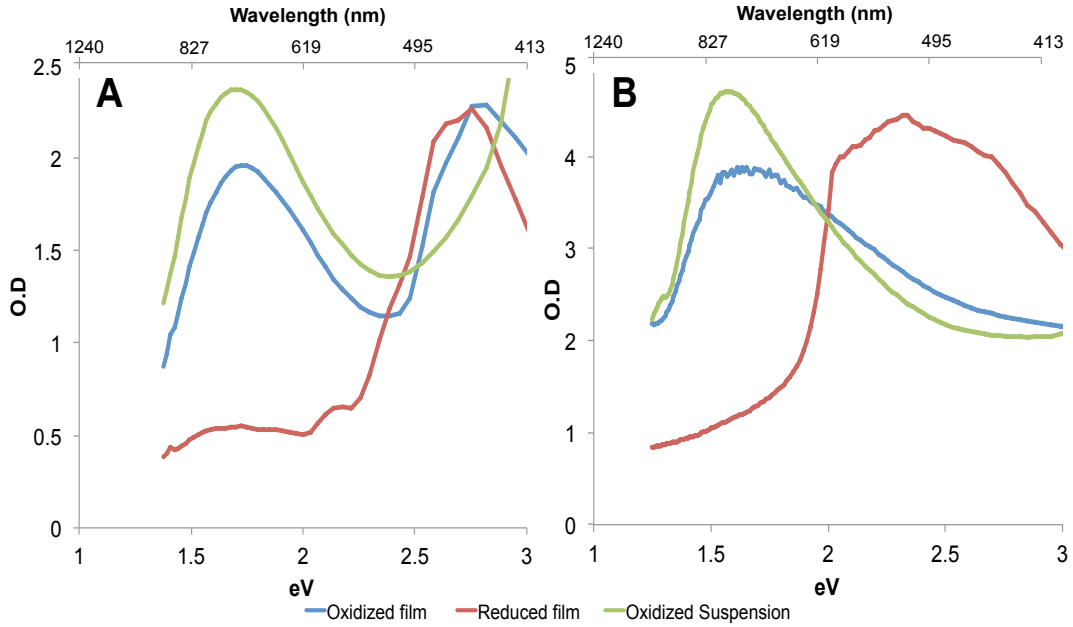

Figure 3-11. UV-Vis-NIR spectroscopy of polymer films P1 (A) and P2 (B).

In order to determine band gap, the films were reduced to the neutral state by dipping them into a solution of hydrazine until the films turned from green/blue to red. Figure 3-3 illustrates this reversible process. In the reduced state the only absorption is from the electrons going from the HOMO to the LUMO;[63] by extrapolating the data from the onset, the band gap (E_g) can be determined, as shown in Figure 3-12. The reduced films exhibited peak absorbance at 2.69 eV (460 nm) for P1 and 2.29 eV (541 nm) for P2. When extrapolated from the onset of the π- π* transition the band gap was determined to be 2.1 eV for P1 and 1.8 eV for P2. BEDOT-B has a band gap of 1.8 eV,[93] and the

different derivatives of alkoxy groups all had a band gap between 1.75 – 2.1 eV.[63] BEDOT-B(OAc)$_2$ has a reported band gap of 1.8 eV, while BEDOT-B(F)$_2$ has a band gap of 1.9 eV.[98] This indicates that when in the neutral state all the polymers with a BEDOT-B(R)$_2$ behave similarly and the difference in pendant groups play a very small role in affecting the band gap of the neutral polymers.

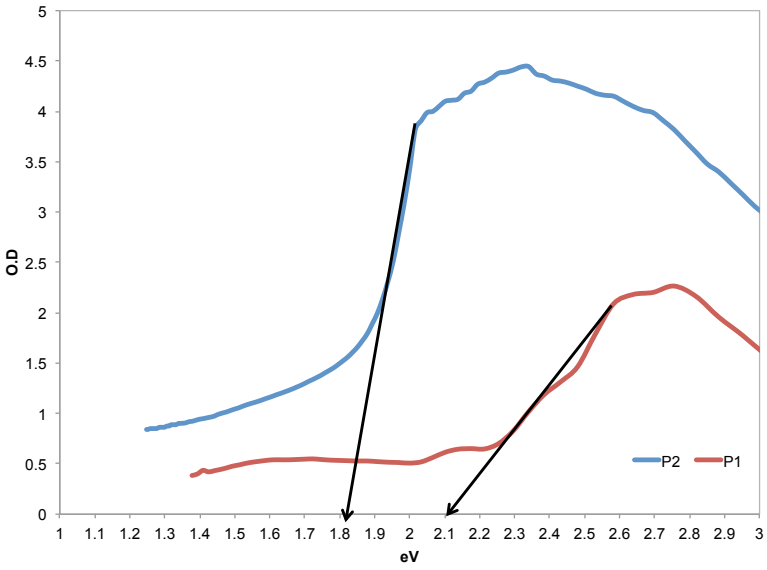

Figure 3-12. Band gap determination of P1 and P2 films

3.8 Conclusions

Two extended conjugation monomers (M1) and (M2) were synthesized using Negishi coupling. Attempts to synthesize a third monomer were unsuccessful. The monomers were electropolymerized, giving electroactive polymer films. The oxidation and reduction potentials for both polymer films were below 0.0 V versus Ag/Ag$^+$, as is characteristic of low oxidation polymers. The role of the substituent groups on the oxidation potential of the monomer was explored and compared to previous studies. It

was determined that by adding either a hexyloxy pendant group or an alkoxy ester pendant group, the oxidation potential of the monomer was lowered compared to BEDOT-B. Repeated cyclic voltammograms showed that the ester group further from the conjugated backbone did decrease the oxidation potential of the polymer compared BEDOT-B$(OAC)_2$ but had similar oxidation potential to BEDOT-B$(OR)_2$, supporting the theory that the functional group directly linked to the backbone is what influences the oxidation potential of the polymer. The effects of the withdrawing groups on polymer P2 were observed in the UV-Vis-NIR spectroscopy when in the oxidized state. Finally the band gap was determined from films deposited onto ITO slides when in the neutral state. There is no significant difference in the band gaps of polymers bearing different pendant groups. Rather, the band gap is controlled primarily by the conjugated backbone itself.

4 PREPERATION AND CHARATERIATION OF CONDUCTIVE POLYMER NANOPARTICLES

4.1 Introduction

In this chapter, the methods developed for the preparation of conductive polymer nanoparticles for photothermal ablation are described. Specifically, oil-in-water emulsion polymerization of 1,4-bis[2-(3,4-ethylenedioxy thienyl]-2,5-dihexyloxybenzene (M1), diethyl 4,4'-{[2,5-bis(2,3-dihydrothieno[3,4-b][1,4] dioxin-5-yl)-1,4-phenylene] bis(oxy)} butanoate (M2) and 3,4-ethylenedioxythiophene (EDOT) (M3) was used to produce aqueous dispersions of P1, P2, and P3 nanoparticles, respectively. The structures are shown in Figure 4-1. Using emulsion polymerization methods similar to those previously reported for polypyrrole and poly(3,4-ethylenedioxythiophene) (PEDOT), the monomers have been polymerized directly as aqueous suspensions. Using this approach, insoluble polymer is suspended in water with the help of stabilizer. During oxidative polymerization of the conductive polymer, cations are delocalized along the heavily conjugated backbone. Anionic surfactants were used as counter ions, stabilizing the oxidized polymer and helping with the self-assembly of the colloidal suspension. The optimal concentration of the surfactants for nanoparticle preparation was investigated. Nanoparticle size distributions were determined using dynamic light scattering, transmission electron microscopy (TEM), and scanning electron microscopy (SEM). Electron microscopy was also used to determine the morphology of the nanoparticles. In addition, UV-Vis-NIR spectroscopy was used to determine the absorbance spectrum of the nanoparticles.

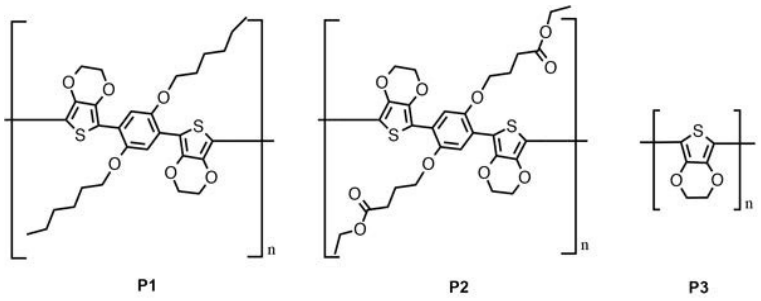

Figure 4-1. Chemical Structures of the polymers described in this chapter

4.1.1 Importance

Traditional electrochemical polymerization methods yield highly conductive polymer films, but once polymerized the films are poorly processable and typically insoluble in organic solvents, limiting their use in many applications. One of the earliest reports of using chemical methods for polymerization of conductive polymers was by Angeli and Lutri who observed the oxidative polymerization of pyrrole using hydrogen peroxide.[99] Several decades later, Bjorklund *et al.* reported the synthesis of polypyrrole (PPy) composites using a similar chemical method.[100] This was the first report of the synthesis of 100 to 200 nm conductive polymer particles. Cellulose/PPy composites were synthesized by dipping cellulose into a solution of $FeCl_3$, followed by immersion into a solution of pyrrole.[100] The pyrrole was polymerized in the pores of the cellulose, yielding conductive paper. This early example of conductive composites led to expanding the application of conductive polymers, which at the time mainly focused on electrochemically produced films. Specifically, the cellulose composites prepared by Bjorklund *et al.* were observed as rather-sensitive reversible chemical sensors for ammonia.[100] Other cellulose/conductive polymer composites have been utilized in ion-

exchange applications and as paper-based batteries.[101–103] All of this work led to alternative techniques for the synthesis of conductive polymers that provide solutions to their solubility problems. Perhaps the most promising approach is Bayer AG's patented process that enables conductive polymers to be suspended in aqueous solution.[104] Bayer developed Baytron® P, a conductive polymer suspension where 3,4-ethylenedioxythiophene (EDOT) is polymerized in water and stabilized by the presence of poly(styrene sulfonate) (PSS), a water–soluble polyelectrolyte, yielding PEDOT:PSS aqueous suspensions. The sub-200 nm colloidal suspension exhibits high conductivity (10 S/cm) and excellent stability, and its films are highly transparent.[104] PEDOT:PSS was originally designed for antistatic coatings, but because of its versatility and transparent nature it has been used in many applications since it became commercially available. This includes electrically conducting coatings, transparent conductors in electroluminescent devices, and also electrochromic windows because the color of the polymer can be changed by applying different voltages.[104]

Another interesting aspect of the PEDOT:PSS synthesis process is that it results in the formation of spherical nanoparticles that exhibit a strong absorbance in the near infrared (NIR) region of the spectrum (600 – 1200 nm), making them suitable as potential photothermal (PTT) agents.

While most of the monomers used to prepare conductive polymers are not water soluble, there are many methods that can be used to deliver water-insoluble monomers into aqueous suspensions. One of the most common and quickest methods for nanoparticle preparation using insoluble monomers is emulsion polymerization. An emulsion polymerization requires four main components: monomer, dispersion medium,

emulsifier, and initiator. Emulsion polymerizations can be divided into three categories: macro-emulsion, mini-emulsion, and micro-emulsion polymerization.[105,106] Macro-emulsion polymerization is most commonly used and will be explained in more detail. While the general process is the same for all emulsion polymerizations, there are subtle differences between the three including the stability of the suspension and size of the droplets before and after polymerization.[107]

Macro-emulsion polymerization occurs when a free-radical polymerizable monomer is dissolved in a solvent, creating the monomer phase.[107] Most commonly, an organic solvent is used. Once dissolved, the monomer solution is added to the dispersion medium, a non-solvent that is most commonly water, creating an emulsion. Emulsifiers are typically surfactants or protective soluble polymers that are often added to the aqueous phase.[106,107] The emulsifiers have a number of important roles, such as stabilizing the monomer droplets in the emulsion and stabilizing the particles once polymerized. Examples of emulsifiers are sodium dodecyl sulfate (SDS), polyvinyl alcohol (PVA), and cetyltrimethylammonium bromide (CTAB). Once the monomer solution is added to the aqueous phase, an initiator is added and the polymerization occurs, usually following the free-radical polymerization mechanism. Initially, the monomer droplets are 1 – 100 μm in size prior to polymerization, resulting in the formation of micron-sized particles.

Mini-emulsion polymerization follows the same mechanism as macro-emulsion polymerization, but when dispersing the monomer in water, high-shear such as sonication is used to form the emulsion.[107,108] This creates much smaller droplets on the order of 50 – 500 nm in size prior to polymerization and typically yields particles in the same

range.[107] Finally, micro-emulsion polymerization consists of monomer droplets with sizes from 10 – 100 nm prior to polymerization; these look like one-phase systems to the naked eye.[107] This process yields sub-50 nm particles.

4.1.2 Significant Background

Emulsion polymerization has recently been used to synthesize conductive polymer nanoparticles. Liu *et al.* reported the synthesis of PPy nanoparticles using micro-emulsion polymerization by first dissolving PVA and $FeCl_3$ in water followed by the addition of pyrrole, yielding PVA-stabilized PPy nanoparticles that showed excellent stability in water and in serum.[60] In a similar approach, PPy particles stabilized by hydroxypropyl cellulose in aqueous media were prepared by Amaike and Yamamoto[109] using $FeCl_3$ to induce oxidative polymerization; the particles produced were uniform in size, and the suspension showed excellent stability by not precipitating out of solution over long periods of time.

Other groups have also reported the synthesis of PEDOT particles using oxidative polymerization with different surfactants and oxidants. Choi *et al.* reported the synthesis of PEDOT particles using dodecylbenzenesulfonic acid (DBSA) as the stabilizer.[110] This process produced particles that were 35 – 100 nm in size. Wu *et al.* also reported the synthesis of PEDOT latex particles stabilized in aqueous suspension in DBSA using a bi-oxidant process with $FeCl_3$ and H_2O_2.[111] By using a bi-oxidant process, more of the EDOT polymerized by regeneration of Fe^{3+} through the addition of the second oxidant H_2O_2, resulting in higher polymer nanoparticle yield. All of these methods used a single surfactant for the stabilization of the nanoparticles.

Using a slightly different approach than what has been previously reported, Han *et al.* synthesized PEDOT nanoparticles stabilized by poly(styrenesulfonic acid-co-maleic acid) PSS-co-MA and DBSA.[112] The fabrication process used a two-surfactant system having PSS-co-MA in the aqueous phase and DBSA in the organic phase. The polymerization was initiated by $FeCl_3$, which was included in the aqueous phase prior to the addition of the monomer. The organic phase was added to the aqueous phase using a spray method in which the monomer solution was loaded into a spray gun and the tip was then submerged into the aqueous phase. Flowing N_2 into the spray gun allowed the monomer to be dispersed into the aqueous phase. Using this process the group was able to achieve 100-nm particles.

In this portion of the study emulsion polymerization was used to synthesize conductive nanoparticles with a strong absorbance in the NIR region. Several different surfactants were studied in an effort to determine the optimal condition for nanoparticle synthesis. Two approaches were used for the synthesis of the nanoparticles the first is a single surfactant method and the second is a two-surfactant system where one surfactant is in the aqueous phase while the other is in the organic. The nanoparticles were characterized using UV-Vis-NIR spectroscopy, scanning and transmission electron spectroscopy, and dynamic light scattering.

4.2 Materials and Methods

4.2.1 Materials

Brij S20, poly(vinyl alcohol) (30,000 – 70,000 Da), bovine serum albumin, hydroxypropyl cellulose (80,000 Da), poly(ethylene glycol) 4-nonylphenyl 3-sulfopropyl

ether potassium salt, and poly(4-styrenesulfonic acid-co-maleic acid) sodium salt (20,000 Da, 3:1 styrenesulfonic acid: maleic acid) were purchased from Sigma Aldrich and used as received. Triton X-100 and chloroform were purchased from J.T. Baker Chemicals and used as received. 4-Dodecylbenzenesulfonic acid (DBSA) was purchased from TCI America and used as received. Ultra pure water was obtained from a Millipore Direct-Q 3 purifying system. 3,4-Ethylenedioxythiophene (EDOT) was purchased from VWR and purified as described previously.[86]

4.2.2 Instrumentation

UV-Vis-NIR measurements were obtained using a BioTek Synergy™ 4 Hybrid Microplate Reader. SEM images were obtained using an FEI Helios Nano Lab 400 scanning electron microscope. SEM samples were coated with 2 nm of iridium using an EMS Quorum EMS150T ES turbo-pumped sputter coater. TEM images were obtained using a JEOL JEM 1200 EXII microscope. Dynamic light scattering measurements were obtained using Malvern Zetasizer Nano ZS. Two different sonicators were used: a Fisher Scientific™ Model 505 Sonic Dismembrator, and a VWR® Symphony™ Ultrasonic Cleaner.

4.2.3 Emulsion Polymerization

Two methods were initially attempted to form nanoparticles via emulsion polymerization. The first involved only using a single surfactant, while the second involved a two-surfactant system.

4.2.3.1 Method 1

The monomer was dissolved in chloroform. The aqueous phase consisted of a 5 % (w/v) aqueous solution of the surfactants depicted in Figure 4-2. To prepare these solutions, the surfactant was added to 1 mL of ultra pure water and mechanically stirred until dissolved. Monomer solution (100 µL) was added drop-wise to the aqueous phase while maintaining continuous stirring. Ferric chloride (3.8 µL of 100 mg/mL solution in ultra pure water) was added to the emulsion immediately after the addition of the organic phase, and the emulsion was stirred 1 h. The nanoparticles were recovered via centrifugation at 75,500 x g, resuspended with ultra pure water, and stored under argon in the dark until further use. Figure 4-2 depicts the process of this method.

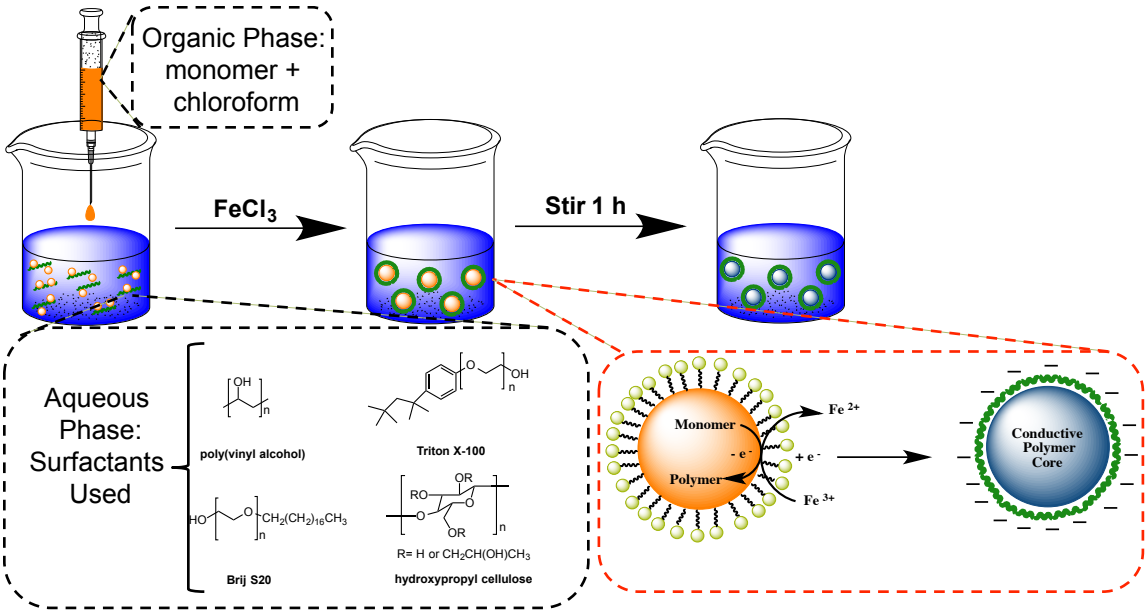

Figure 4-2. Procedure used in Method 1 and chemical structures of surfactants utilized in the aqueous phase. In this method there is only surfactant in the aqueous phase.

4.2.3.2 Method 2

Figure 4-3 depicts the process used for preparation of nanoparticles with Method 2. A procedure similar to Han *et al.* was followed during the preparation of the nanoparticles.[112] The organic phase consisted of monomer 1.6% (w/v) and DBSA 3% (w/v) dissolved in chloroform. This organic solution was mixed for 30 min to ensure homogeneity. The aqueous phase was prepared by dissolving PSS-co-MA in ultra pure water to a concentration of 2% (w/v). The organic phase was then added dropwise to the aqueous phase while stirring. After completing the addition of the organic phase, ultra pure water (3 mL) was added, and the sample was sonicated for 10 min in a water bath. $FeCl_3$ (3.8 μL of 100 mg/mL) was then added to the emulsion while stirring, followed by continuous stirring for 1 h. The suspension was carefully transferred to dialysis tubes and dialyzed for 2 days using a 100,000 molecular weight cut-off cellulose ester membrane. The dialyzed nanoparticle suspension was then sealed under argon and stored in the dark until further use.

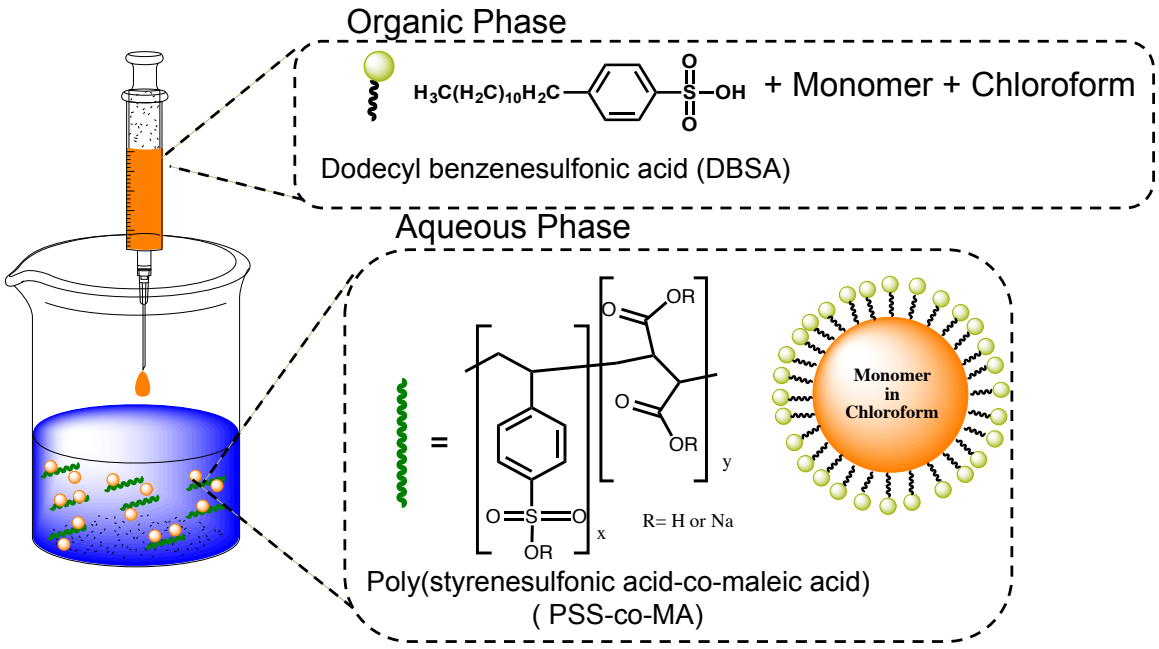

Figure 4-3. Procedure used in Method 2. A two-surfactant system that contains DBSA in the organic phase and PSS-co-MA in the aqueous phase was used in this process.

4.2.3.2.1 DBSA Concentration Study with Method 2

In this study, the effect of the concentration of DBSA in the organic solution on the formation and spectral properties of the nanoparticles formed through Method 2 was investigated. Monomer (16 mg/mL) was added to varying concentrations of DBSA ranging from 0 – 0.9 mg/mL (Table 3-1) in chloroform. The solutions were allowed to mix for 30 min. The aqueous phase consisted of 2 % (w/v) of PSS-co-MA. The organic phase was added dropwise to the aqueous phase while stirring. After the complete addition of the organic phase, ultra pure water (3 mL) was added, and the emulsion was sonicated in a water bath for 10 min. $FeCl_3$ (3.8 µL of 100 mg/mL) was added to the emulsion and stirred for 1 h. The suspension was then transferred to a dialysis tube with a molecular weight cut-off of 100,000 cellulose ester membrane and dialyzed for 24 h. The

suspensions were then characterized using DLS, scanning and transmission electron microscopy, and UV-Vis-NIR spectroscopy.

4.2.4 Characterization

Dynamic light scattering (DLS) measurements were used to determine the average size of the nanoparticles in aqueous suspension. SEM and TEM imaging allowed for morphology determination. The absorbance of the nanoparticle suspensions was determined by UV-Vis-NIR spectroscopy.

4.3 Results and Discussion

4.3.1 Method 1

Several studies have demonstrated the synthesis of PPy nanoparticles via emulsion polymerization.[100,109,113,114] In this study, we explored the synthesis of PEDOT and PEDOT derivatives using emulsion polymerization. Two separate approaches were used in an effort to determine the best procedure for synthesizing nanoparticles that have a strong absorbance in the NIR region and suitable size for biomedical applications. In the first method, four different surfactants were studied: two anionic and two neutral, as shown in Figure 4-2. For the first method, the concentration of monomer M3, addition rate, $FeCl_3$ concentration, mixing method, and reaction times were kept constant. Initially, the emulsions were cloudy after complete addition of the organic phase to the aqueous phase, with the exception of the emulsions prepared with Triton X-100 which had a pale blue hue. Upon the addition of the oxidant, $FeCl_3$, the emulsions remained cloudy, and the color turned from white to a light yellow. The final products after polymerization can be seen in Figure 4-4, where the emulsion remained cloudy and large

particulates were visible in the medium. Additionally, none of these suspensions had an absorbance in the NIR region, indicating that oxidative polymerization may not have occurred. As discussed in Chapter 2, all three polymers absorb strongly in the NIR region. Thus, this method may not be suitable for the synthesis of stable conductive polymeric nanoparticles for use as photothermal therapy agents. Triton X-100 was the only surfactant with an obvious visible change, and because of this a more detailed study was conducted using this surfactant.

In the case of emulsions prepared with Triton X-100, the emulsion turned from translucent to a cloudy yellow. Triton X-100 was further investigated, using a higher surfactant concentration of 32 mg/mL in the aqueous phase. By using this method, M1 was polymerized yielding a colloidal suspension. At the higher surfactant concentration, the emulsion changed from cloudy white to cloudy green once the oxidant was added yielding P1. After purification, the absorption of the colloidal suspension was measured, demonstrating a strong absorbance in the NIR region (Figure 4-5 A).

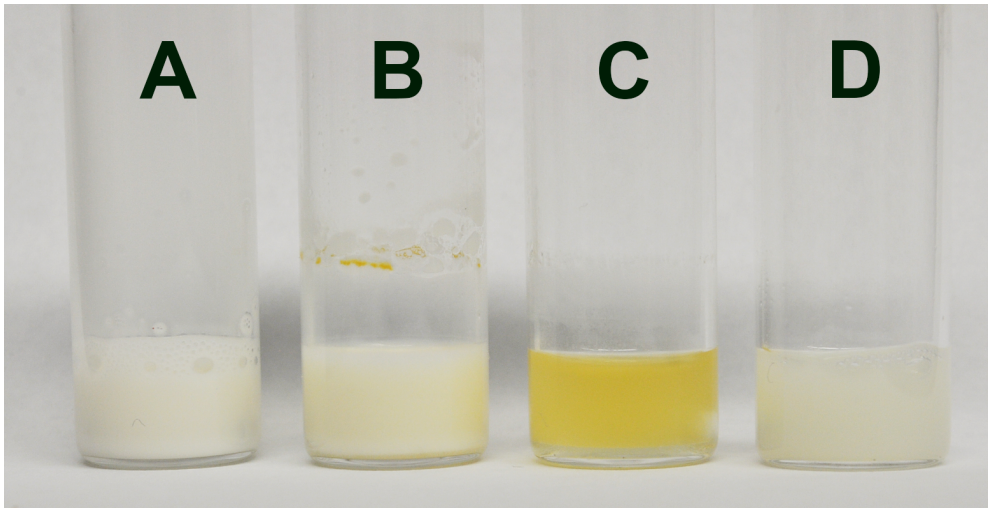

Figure 4-4. Product of oxidative emulsion polymerization of P3 using Method 1. The aqueous phase consisted of a 5% solution of the following surfactants: **A**. Poly(vinyl alcohol). **B**. Brij S20. **C**. Triton X-100. D. hydroxypropyl cellulose

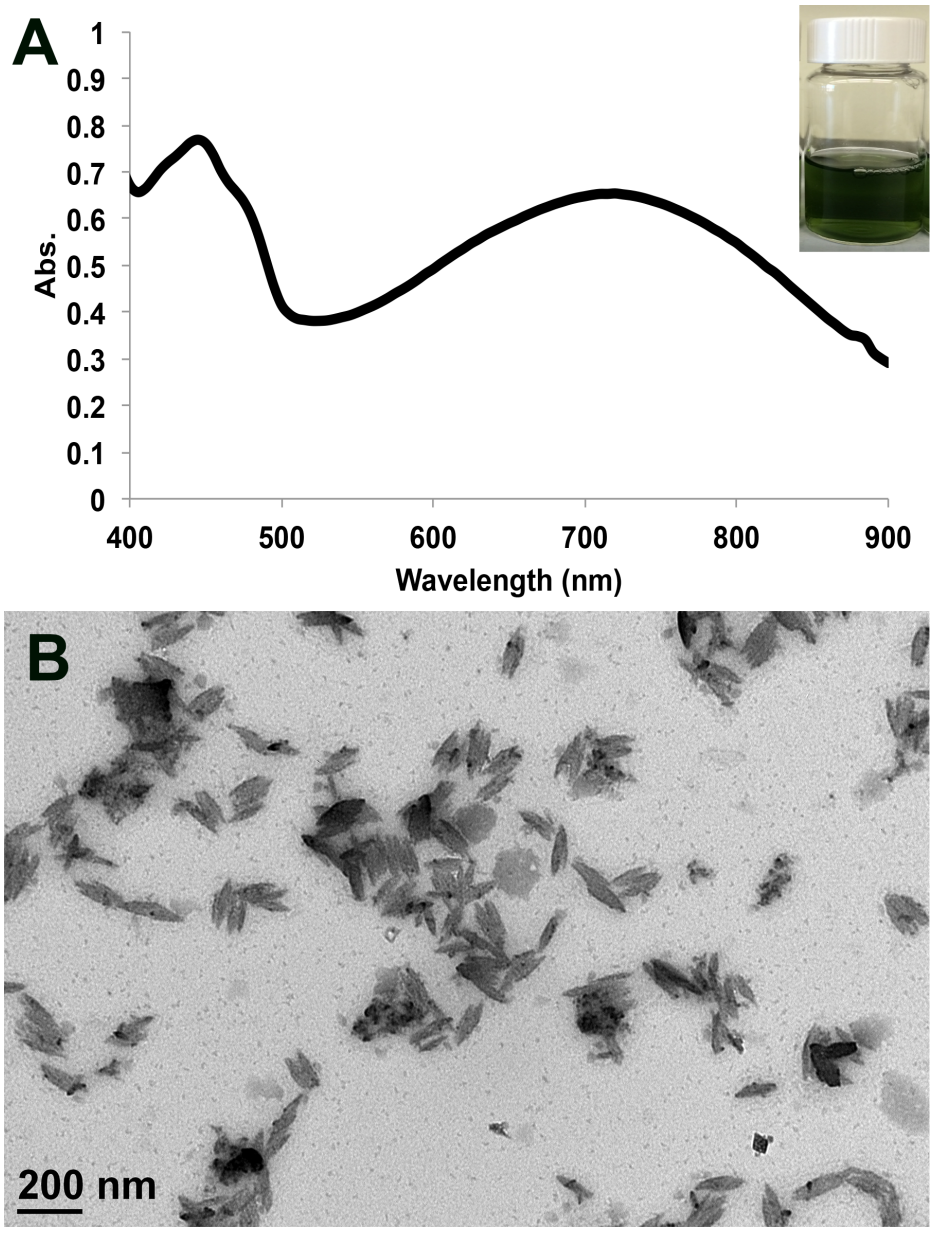

Figure 4-5. P1 nanoparticles synthesized using Method 1 where Triton X-100 is the stabilizer (32 mg/mL). **A**. Absorbance spectra of suspension, with an absorbance in the NIR region. Insert: image of suspension after purification **B**. TEM image of rod-shaped particles.

P1 nanoparticles were further characterized using transmission electron microscopy, and images show that the polymer nanoparticles synthesized were rod-shaped and sub-100 nm in length (Figure 4-5 B). Similar results have been reported by

Armes *et al.* and Sun *et al.*[115,116] In an attempt to produce polyaniline colloidal suspensions in water, Armes *et al.* oxidatively polymerized aniline using water-soluble reactive stabilizers containing pendant aniline groups as graft sites in aqueous media.[115] The result was sterically stabilized rod-shaped polyaniline nanoparticles. Sun *et al.* also reported the synthesis of PEDOT nanowires which were oxidatively polymerized in aqueous media using poly(acrylic acid) as a stabilizer.[116] It is well understood that conductive polymers are heavily π-conjugated, and the $\pi - \pi^*$ interactions in these polymers influence self-assembly as rods or nanowires, as shown for both polyaniline and PEDOT particles.[115,116] Similarly, the polymer synthesized using Method 1 has these same rod-shaped features due to $\pi - \pi^*$ interactions along the backbone, leading to stacking of polymer sheets along the backbone. Once polymerized, the particles are stabilized by electrostatic interactions between the polymer and the stabilizer. In addition to electrostatic interactions, there may also be some $\pi - \pi^*$ interactions between the heavily conjugated polymer backbone and the surfactant. This can only occur if the surfactant has π –conjugation, such as in the case of Triton X-100.

4.3.2 Method 2

In an effort to change the morphology of the nanoparticles, a two-surfactant system was incorporated. Han *et al.* reported the use of a two-surfactant spray emulsion polymerization method that yielded spherical nanoparticles that were stable in aqueous media.[112] In our approach, we used a dropwise method, where DBSA 3% (w/v) was added to the organic phase, and the aqueous phase contained 2 % (w/v) PSS-co-MA. As the organic phase was added dropwise, the color of the emulsion slowly changed from yellow to light green in the case of M3. After complete addition of the monomer, the

oxidant was added, and the color changed from light green to dark green, giving P3 nanoparticles. From the DLS results, P3 particles suspended in PSS-co-MA had a diameter of 52 nm and demonstrated a strong absorbance in the NIR region, as shown in Figure 4-6.

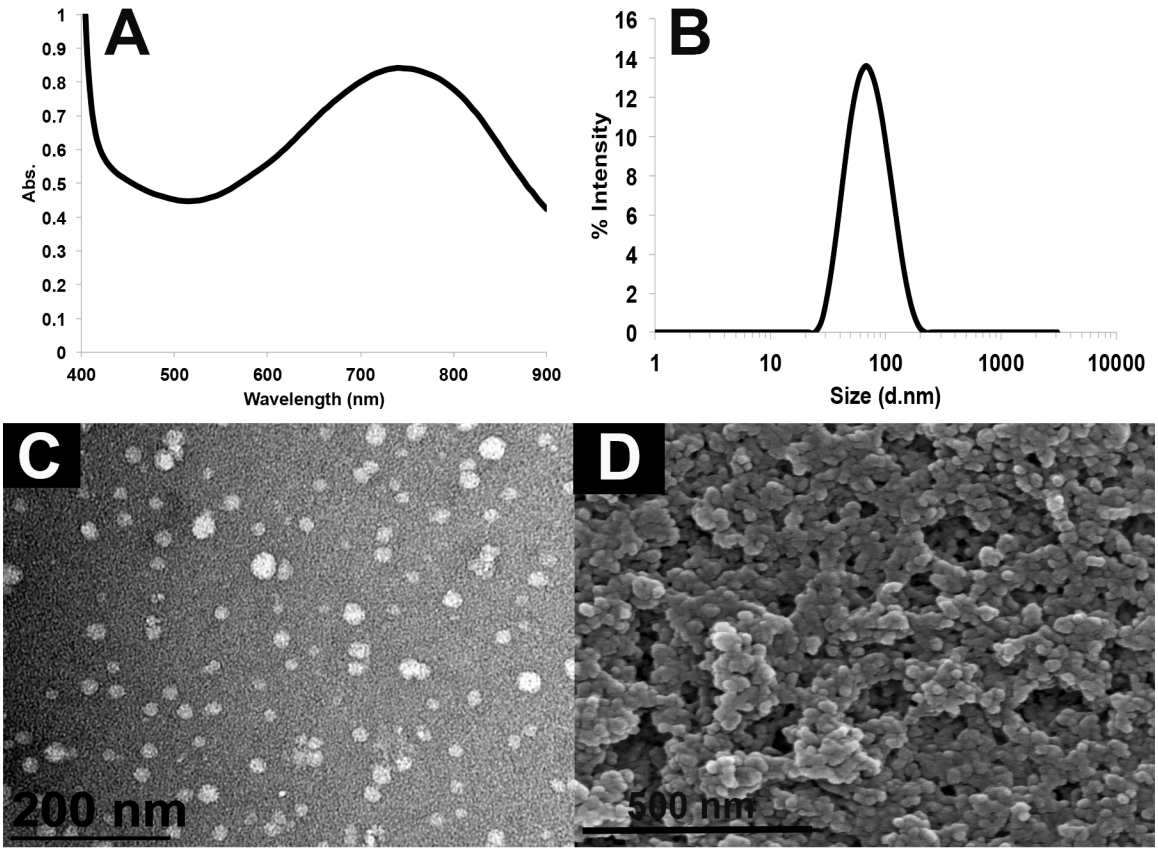

Figure 4-6. Characterization of P3 nanoparticles. **A.** UV-ViS-NIR absorption spectrum showing strong absorption in the NIR region. **B.** DLS size distribution. **C.** TEM image of spherical nanoparticles. **D.** SEM image of nanoparticles.

For the synthesis of P2 nanoparticles, as the organic phase was added dropwise to the aqueous phase, the color of the emulsion changed from light yellow to a light purple. After complete addition of the M2, the oxidant was added, and the color changed from light purple to dark blue. SEM images for P2 show that these particles have spherical

morphology, in contrast to the rod-shaped particles observed with Method 1. DLS data also show that the particles had an average diameter of 60 nm. The P2 suspension also shows a strong absorbance in the NIR region as shown in Figure 4-7. This indicates that the two-surfactant emulsion method can also used to prepare nanoparticles from larger EDOT derivatives.

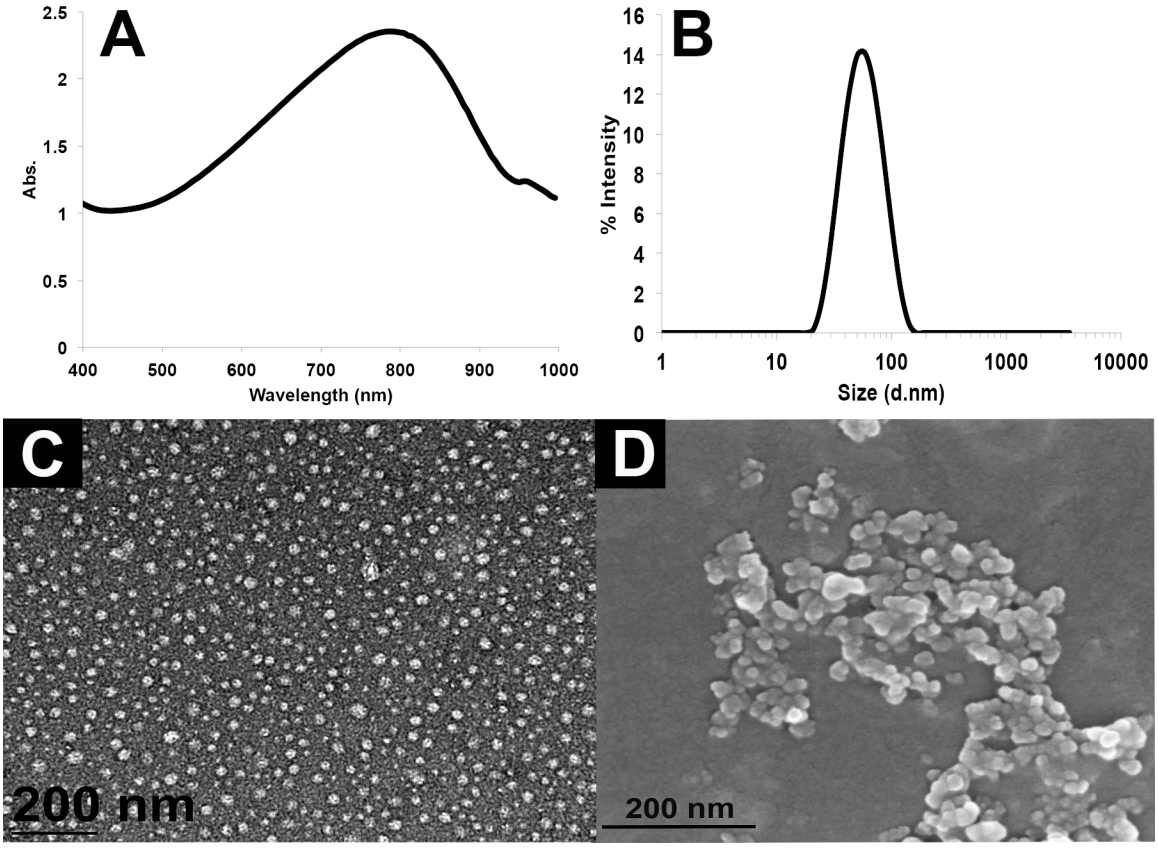

Figure 4-7. Characterization of P2 nanoparticles. **A.** UV-ViS-NIR absorption spectrum. **B.** DLS size distribution. **C.** TEM images of spherical nanoparticles. **D.** SEM image of P2 nanoparticles.

In an effort to further understand the role of DBSA in the organic phase, the concentration of the surfactant was varied using the same method described above with EDOT as the monomer. By changing the surfactant concentration in the organic phase, it

was determined that DBSA affects the morphology and size of the particles. Table 4-1 summarizes the conditions and results of these trials.

Table 4-1. Conditions Used for Method 2

Trial	PSS-co-MA Concentration (%)	DBSA in Organic	Size (nm)	Morphology
1	2%	No	Particles not stable	N/A
2	2%	1.5%	N/A	Rod shaped
3	2%	3%	75	Spherical
4	2%	6%	120	Spherical
5	No	3%	N/A	Rod shaped

Initially, as the organic phase was added to form the emulsions, all of the samples turned to a light yellow. However, as more monomer was added, trials 3 – 5 appeared dark brown, whereas trial 2 appeared yellow. Trial 1 phase separated (oil droplets settled to the bottom). Once the oxidant was added, all the emulsions turned dark green with the exception of trial 1. The color change of the suspension to a dark green after addition of the oxidant indicates that polymerization occurred to form polymer in the oxidized state; this is further confirmed by an absorbance in the NIR region. The suspensions before and after the addition of the oxidant are shown in Figure 4-8.

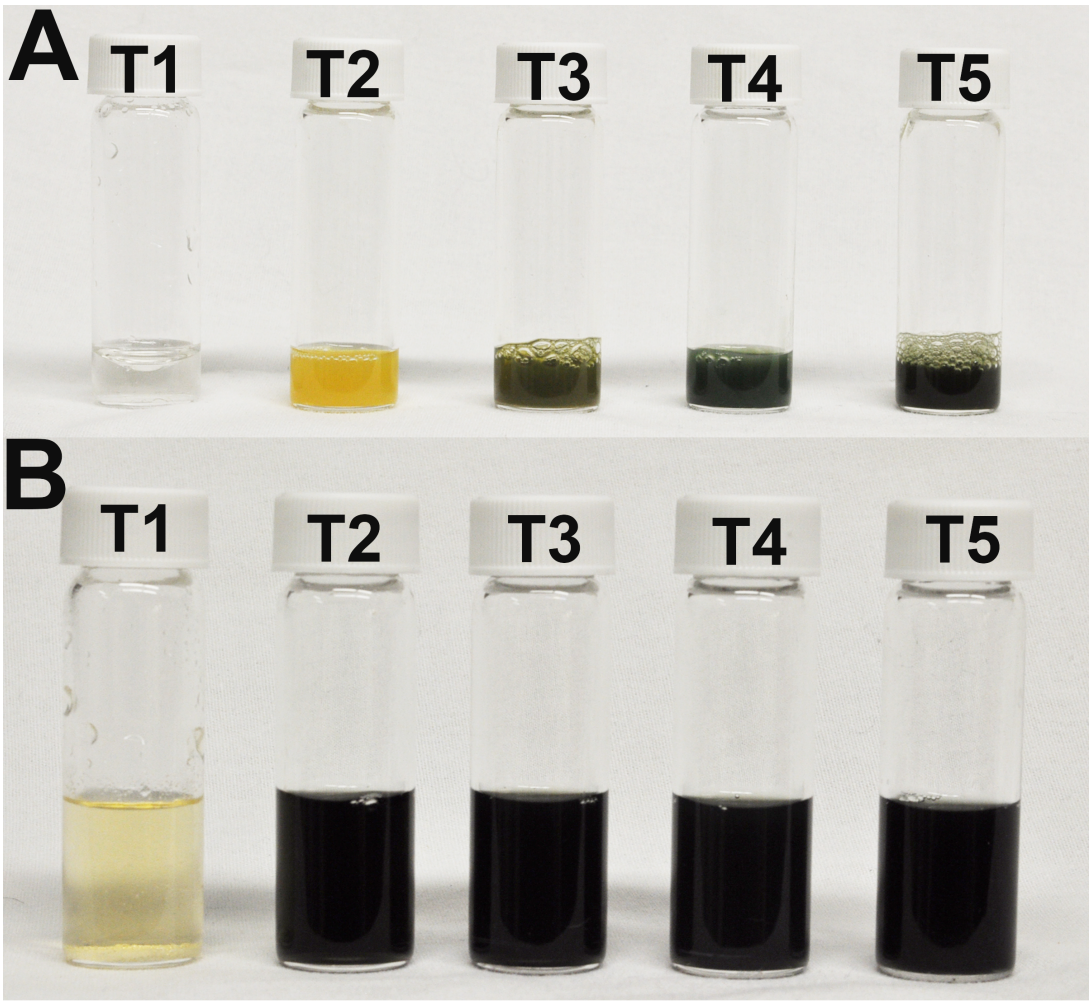

Figure 4-8. Images of Trials 1-5 **A.** Image of samples prior to addition of $FeCl_3$. **B.** Image of samples after the addition of $FeCl_3$

Suspensions synthesized without any DBSA in the organic phase were unstable after polymerization and did not exhibit an absorbance in the NIR region. It can be concluded that for this method DBSA is required in the organic phase to help stabilize the monomer when added to the aqueous phase prior to polymerization. As discussed in Section 4.3.1, the polymerization of PEDOT and PEDOT derivatives in the presence of Triton X-100 in the aqueous phase led to rod-shaped particles. In a study reported by Jin *et al.*, β-1,3-glucan, a polysaccharide extracted from *Sparassis crispa*, was added to

EDOT in the organic phase to obtain a stable colloidal suspension of spherical polymer particles in aqueous medium.[117] β-1,3-glucan acts as a stabilizer in water by forming triple helix structures that complex with PEDOT.[117,118] Similar to β-1,3-glucan, DBSA in the organic phase helps stabilize the monomer once added to the aqueous phase prior to polymerization by the formation of micelles. This occurs because of the hydrophobicity of the monomer and the amphiphilic nature of the surfactant. Once polymerized, the oxidized polymer is balanced by the negatively charged DBSA and PSS-co-MA. Washing the particles removes excess DBSA and PSS-co-MA, and the remaining surfactant is complexed with the oxidized polymer. PEDOT particles reported by Han *et al.* which were synthesized in the presence of DBSA in the organic phase and no surfactant in the aqueous phase were rod-shaped; however, particles synthesized in the presence of both DBSA and PSS-co-MA were spherical.[112] This was also observed in our studies. Figure 4-8 shows the TEM images of the suspensions of P3 with different DBSA concentrations, as well as the DLS for trials 3 and 4. It was observed that in trial 5 the the particles were rod-shaped and, as the concentration of DBSA was increased, the spherical shape began to evolve. Trial 2 suspensions were still rod shaped; however, they were smaller than the rods observed in trial 5. Polymer particles prepared in trial 3 and 4 were spherical, with trial 3 having slightly smaller size. The long chain PSS-co-MA helps stabilize the DBSA-monomer micelle; from the results it is postulated that if the DBSA concentration is too low, or in absence of PSS-co-MA, the micelles may expand or coagulate during polymerization forming rigid polymer sheets. $\pi - \pi^*$ interactions between these sheets may then lead to $\pi - \pi^*$ stacking of the sheets along the backbone forming layered rod-shaped particles. From the TEM images and DLS data, the

nanoparticle suspension prepared with 6 mg/mL DBSA appears to produce larger particles than that prepared with 3 mg/mL DBSA. A study by Muller *et al.* reported that as the concentration of the emulsifier increased, the size of the particles decreased.[119] This was reported for the synthesis of PEDOT nanoparticles in the presence of a single surfactant. In our experiments we determined that by using a two-surfactant system the particles first change morphology, from rod-shaped to spherical with increasing concentration of surfactant in the organic phase, followed by an increase in size as observed by increasing the concentration from 3 mg/mL to 6 mg/mL of DBSA. TEM images in Figure 4-8 show the change in size as the different DBSA concentration. This increase in size still needs to be further investigated, but may be attributed to an increase in viscosity of the organic solution. The increased viscosity caused by the higher DBSA concentration may lead to larger droplet size during addition. Due to the low shear produced by mechanical stirring these larger droplets may not get broken into smaller ones when mixing.

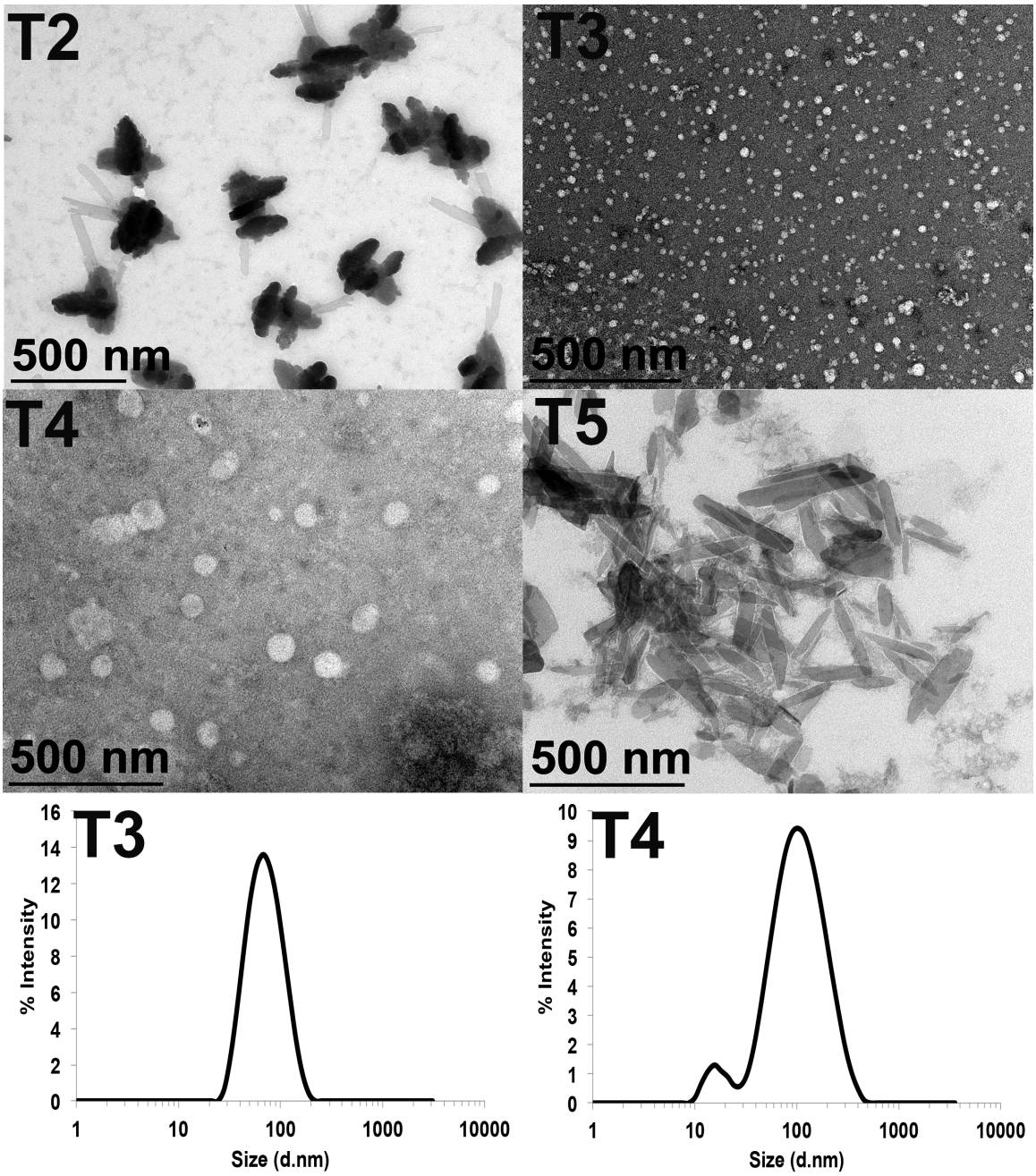

Figure 4-9. Effect of surfactant concentration on P3 nanoparticle size and morphology. TEM images of the resulting P3 nanoparticles prepared in: Trial 2, Trial 3, Trial 4, and Trial 5. DLS size distribution of P3 nanoparticles prepared in Trial 3 and Trial 4.

4.4 Conclusions

Colloidal suspensions of P2 and P3 in aqueous media were prepared via emulsion polymerization using one- or two-surfactant systems; both resulted in polymer nanoparticle formation. Using the first method, the surfactant that showed the most promise for the suspension of P1 and P2 was Triton X-100. The particles obtained using the first method with Triton X-100 as the surfactant produced particles with a rod-shaped morphology (as evidenced by TEM) and an absorbance in the NIR region. However, the particles were not stable in suspension for long periods of time. The rod-shaped morphology is attributed to $\pi - \pi^*$ interactions within the rigid backbone of the polymer. The two-surfactant system plays an important role in the formation of oxidized spherical nanoparticles. PSS-co-MA helps stabilize the particles in the aqueous media, allowing for the formation of spherical particles. The use of DBSA is needed to help form micelles when the monomer is initially added to the aqueous media, as well as keeping the polymer in the oxidized state after polymerization. Using this method the nanoparticles obtained had a spherical morphology, could be produced in the desired size range (sub-100 nm diameter), and presented strong absorption in the NIR range of the spectrum.

5 EVALUAITON OF CONDUCTIVE POLYMERS AS PHOTOTHERMAL ABLATION AGENTS

5.1 Introduction

The nanoparticles synthesized in the previous chapter were further explored as photothermal (PT) agents for breast cancer treatment. In this study, we determined the PT effect of the nanoparticles in the NIR region at different concentrations, as well as the PT conversion efficiency of the colloidal suspensions. The PT effect and efficiency of P2 and P3 were both compared to commercially available Clevios PH1000 (PEDOT:PSS) and gold nanorods (GNRs) synthesized and provided by the laboratory of Dr. Joseph Tracy from North Carolina State University. The suspensions were compared both at the same concentration as well as at the same optical density. The cytotoxicity of the nanoparticles after incubation for 24 h in the presence of breast cancer cells was determined at a concentration range of 0.2 – 500 μg/mL. Further *in vitro* studies determined the PT therapeutic effect of the nanoparticles on breast cancer cells.

5.2 Materials and Methods

5.2.1 Materials

Poly(4-styrenesulfonic acid-co-maleic acid) sodium salt (PSS-co-MA, 20,000 Da, 3:1 styrenesulfonic acid: maleic acid) was purchased from Sigma Aldrich and used as received. 4-Dodecylbenzenesulfonic acid was purchased from TCI America and used as received. Ultra pure water was obtained from a Millipore Direct-Q 3 purifying system. 3,4-Ethylenedioxythiophene (EDOT) was purchased from VWR and purified as described previously.[86]

MDA-MB-231 metastatic human breast cancer cells derived from pleural effusion were purchased from ATCC®. Dulbecco's Modified Eagle's Medium (DMEM) with or without phenyl red, fetal bovine serum (FBS), Dulbecco's Phosphate-Buffered Saline (DPBS) with or without calcium and magnesium, Trypsin, (4-2-hydroxyethyl)-1-piperazineethanesulfonic acid) (HEPES), and penicillin streptomycin were all purchased from Corning. (3-[4,5-dimethylthiazol-2-yl]-2,5diphenyl tetrazolium bromide) (MTT) was purchased from Alfa Aesar and the Live/Dead® cell viability assay (L3224) was purchased from Thermo Fisher Scientific.

5.2.2 Instrumentation Used for Photothermal Studies

The setup used for the photothermal studies is shown in Figure 5-1. This set up has been previously utilized for the investigation of the photothermal conversion efficiency of gold nanostructures by our collaborators.[50] An 808-nm diode laser rated at 1 W of power was used in these studies. An InSb infrared IR camera (FLIR Systems) was used to measure the temperature change of the samples. The laser was focused to a 6 mm diameter with the use of a bioconvex lens (Thor Labs) which was mounted at approximately 30° in order to avoid interfering with the measurements of the IR camera. All of the measurements were conducted in 96-well plates with a sample volume of 100 μL.

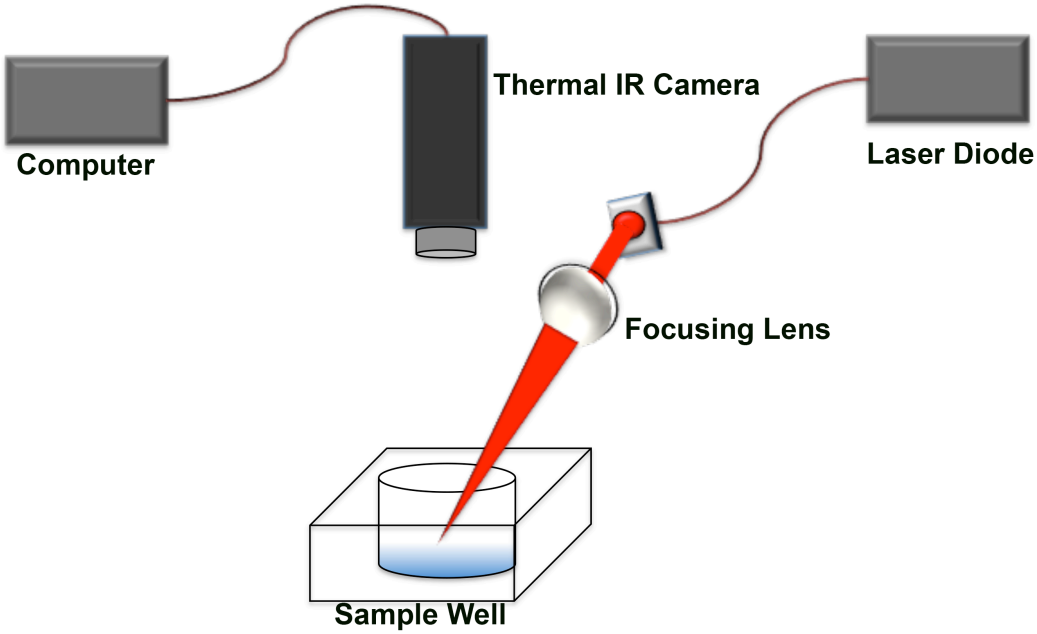

Figure 5-1. Diagram of set up utilized for photothermal studies. The laser beam transported through an optical fiber was focused through a biconvex lens set a slight angle so as to not to interfere with temperature measurements. A thermal IR camera was placed directly above the sample well to measure sample temperature changes over time.

5.2.3 Photothermal Conversion Efficiency Determination

The PT conversion or transduction efficiency, η_T, of the polymeric nanoparticles was calculated using a method previously reported by Roper *et al.*[120], as described by Equation 1:

$$\eta_T = \frac{hA(T_{max} - T_{amb}) - Q_0}{I_O(1 - 10^{-OD})} \quad (1)$$

where h is the heat-transfer coefficient, A is the surface area, T_{max} is the maximum temperature reached by the system, T_{amb} is the ambient temperature of the surroundings, Q_0 is the heat generated by the light absorbed from the sample well and water, I_O is incident laser power, and OD is the optical density.

In order to determine η_T, the total energy balance of the system is considered and shown in Equation 2:

$$\sum_i m_i C_{p,i} \frac{dT}{dt} = Q_{in,np} + Q_{in,sample} - Q_{ext} \quad (2)$$

where m_i and $C_{p,i}$ are the mass and heat capacity, respectively, T is the temperature of the sample and t is the time. The term $Q_{in,np}$ is representative of the heat generated by the nanoparticles upon laser irradiation at a given wavelength. It should be noted that this term excludes the heat generated by the water in which the nanoparticles are suspended. The term $Q_{in,sample}$ is representative of the heat generated by laser light absorbed by the 96-well plate and water. The term Q_{ext} is the heat transfer between the sample and the surroundings.

The heat generated by the nanoparticles upon irradiation $Q_{in,np}$ can be defined as:

$$Q_{in,np} = (I_O - I)\eta_T \quad (3)$$

where I_O is the incident laser intensity and I is the transmitted intensity. Equation 3 is derived from:

$$OD = \log_{10} \frac{I_O}{I} \quad (5)$$

After taking the inverse log of both sides equation 5 becomes:

$$10^{OD} = \frac{I_O}{I} \quad (6)$$

solving for I yields:

$$I = I_O 10^{-OD} \quad (7)$$

Equation 7 can then be plugged into Equation 3 yielding:

$$Q_{in,np} = I_O(1 - 10^{-OD})\eta_T \quad (8)$$

where I_O is the incident laser power and OD is the optical density of the nanoparticle suspension at the laser wavelength (808 nm) under the conditions of the study.

The term $Q_{in,sample}$, was measured by irradiating a sample well containing 100 μL of the buffer solution using the same conditions for the irradiation of nanoparticle suspensions and is defined as:

$$Q_{\text{in,sample}} = hA\left(T_{sample} - T_{amb}\right) \quad (9)$$

The term Q_{ext} can be defined by Newton's 2nd law of cooling:

$$Q_{ext} = hA\left(T_{sample} - T_{amb}\right) \quad (10)$$

where h is the heat transfer coefficient, A is the area of the sample well, T_{sample} is the temperature of the sample after reaching steady state during laser irradiation, and T_{amb} is the room temperature. The value of hA can be determined by measuring the cooling rate of the sample after heating to steady state and turning the laser off. In the absence of laser irradiation, the values for $Q_{in,np}$ and $Q_{in,sample}$ are zero and Equation 2 reduces to:

$$\sum_i m_i C_{p,i} \frac{dT}{dt} = -hA\left(T_{sample} - T_{amb}\right) \quad (11)$$

after integrating and solving for t equation 6 becomes:

$$t = -\frac{\sum_i m_i C_{p,i}}{hA} \ln(\Delta T) \quad (12)$$

By plotting ln(ΔT) vs. time of the cooling, a line is obtained where the slope is equal to the $(-\Sigma_i m_i C_{p,i}/hA)^{-1}$ and hA can be determined. In our experiments m_i and $C_{p,i}$ are the mass and heat capacity of the sample, which are approximated to those of water.

Using the calculated value of *hA,* one can determine the value of $Q_{in,sample}$ value by using Equation 9. After solving for $Q_{in,sample}$ and *hA* these values can be used in Equation 1 to solve for η_T.

5.2.4 Photothermal Comparison

A procedure similar to Han *et al*. was followed during the preparation of the nanoparticles. The monomer (M2 or M3, 16 mg/mL) and DBSA (0.3 g/mL) were dissolved in chloroform. The solution was mixed for 30 min to ensure homogeneity. In a separate container, PSS-co-MA was dissolved in ultrapure water at a concentration of 2% w/v and stirred for 30 min. The organic phase was then added dropwise at 10 μL intervals to the aqueous phase while stirring. After completing the addition of the organic phase, 3 mL of ultrapure water were added $FeCl_3$ (2.2 mol) was added to the emulsion as an aqueous solution at 100 mg/mL while stirring. The emulsion was stirred for 1 h to enable the polymerization to take place. The suspension was then dialyzed for several days using a 100,000 molecular weight cut-off cellulose ester membrane. The dialyzed nanoparticle suspension was then stored under argon and sealed until further use. The concentration of nanoparticles in suspension was determined by lyophilizing 1 mL of the dialyzed suspension and weighing the dried product.

5.2.5 Cell Culture

MDA-MB-231 breast carcinoma cells were grown in Dulbecco's Modified Eagle's Medium (DMEM) containing 10% fetal bovine serum (FBS). The cells were grown in T-75 flasks and incubated at 37 °C under an 8.5% CO_2 atmosphere.

5.2.6 Cytotoxicity

The cells in the T-75 flasks were washed three times with DPBS (without calcium and magnesium) and incubated at 37 °C with trypsin. The trypsinization process was then stopped by addition of fresh media. The cells were transferred to a centrifuge tube and centrifuged at 125 x g for 5 min. The cells were resuspended in fresh media and counted using a hemocytometer. The cells were seeded on to 96-well plates at a cell density of 5,000 per well. The cells were incubated for 24 h at 37 °C and 8.5% CO_2 prior to the addition of nanoparticle suspensions.

Nanoparticle suspensions were dialyzed in water for 24 h, after which they were transferred to the laminar flow hood. Prior to use, the nanoparticle suspensions were sterilized by filtration through a 0.2 μm polyethersulfone (PES) membrane filter. The nanoparticle suspensions were diluted in complete media without phenol red. Nanoparticles were added to the cells (100 μL) at a starting concentration of 500 μg/mL and diluted by thirds to a final minimum concentration of 0.2 μg/mL. Positive and negative controls were incubated with 100 μL of media lacking nanoparticless. The cells were incubated in the presence of nanoparticles for 24 h. After the incubation time, the nanoparticle suspensions were removed and the cells were washed with DPBS (containing calcium and magnesium) twice. Cells in the negative control were treated with methanol for 10 min. The MTT assay was used to determine the cell viability. The MTT assay is a colorimetric assay where (3-[4,5-dimethylthiazol-2-yl]-2,5diphenyl tetrazolium bromide) is cleaved by mitochondrial dehydrogenases, found in live cells, producing purple formazan crystals that are insoluble in water. The crystals are dissolved by DMSO, and the purple product can be measured spectrophotometically.[121] The MTT

reagent solution was made at a concentration of 0.5 mg/mL in DPBS (containing calcium and magnesium) and was sterile filtered. Cells were then incubated with 100 μL of the MTT solution for 2.5 h. After incubation, the MTT solution was carefully removed and replaced with 100 μL of DMSO. The plates were placed on an orbital shaker for 5 minutes to completely dissolve the formazan crystals. The absorbance of the samples was determined at 570 and 700 nm. The background absorbance (700 nm) is subtracted from that of the formazan solution (570 nm) to normalize the data. Each concentration was analyzed in replicates of six. The six values for each concentration were averaged and compared to the control.

5.2.7 *In Vitro* Photothermal ablation of MDA-MB-231 cells

The PT studies were conducted in a custom-made incubator at 37 °C in order to emulate physiological temperature, the inside of the incubator is shown in Figure 5-2. The heat in the incubator was generated using filament bulbs that were wired to an STC-1000 probe temperature controller. The temperature controller maintained a constant temperature of 37 ± 1 °C within the incubator. The CO_2 level within the incubator was not maintained. A live/dead cell assay was used to determine the cell death by irradiation in the presence of nanoparticles. The cells were seeded at a cell density of 5,000 cells per well in 96-well plates and incubated for 24 h at 37 °C and 5 % CO_2 prior to use. The nanoparticle suspensions were filtered through a 0.2 μm filter and diluted in DMEM without phenol red containing 10 % FBS, 1% streptomycin, and 1 % HEPES. The media was removed from the 96-well plates and the cells were washed twice with DPBS. The nanoparticle suspensions were added at two different concentrations (10 and 50 μg/mL), and the cells were incubated for 1.5 h prior to irradiation. Negative ablation controls

included cells exposed to nanoparticles but not irradiated (dark control), cells exposed to laser irradiation in the absence of nanoparticles, and cells not exposed to laser or nanoparticles. Positive controls consisted of cells killed with methanol.

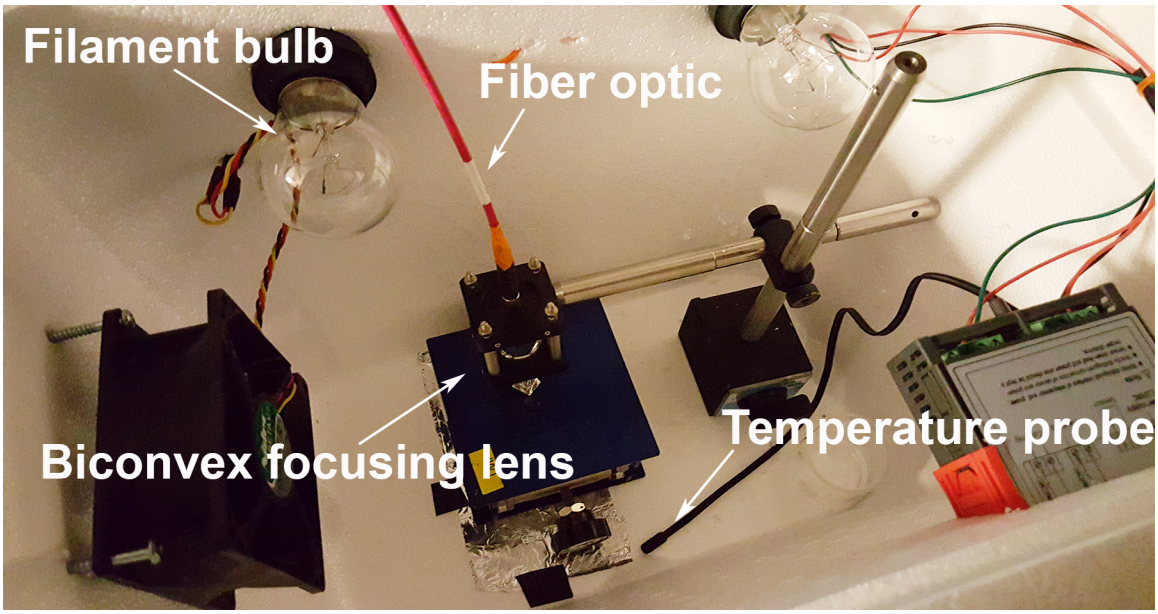

Figure 5-2. Inside of the incubator used for the *in vitro* photothermal studies. The temperature was maintained at 37 ± 1 °C

For irradiation, 96-well plates were transferred to the temperature-controlled incubator where the samples were irradiated for 5, 10 and 15 min intervals at a laser power of 0.8 W with a spot size of 3 mm. After irradiation, the nanoparticle suspensions were removed and the cells washed with DPBS with calcium and magnesium three times. The cells were then incubated for 1 h after irradiation prior to determination of the extent of cell death. All of the studies were done in triplicate.

The extent of cell death after irradiation in the presence of the nanoparticles was determined qualitatively and quantitatively. For qualitative analysis, a live/dead assay kit was used to distinguish the live and dead cells by staining. The Live/Dead viability kit for

mammalian cells is a two-color fluorescence assay that determines cell viability by distinguishing live cells from dead cells. Calcein AM and ethidium homodimer-1 (EthD–1) are two dyes that can recognize cell viability, by intracellular esterase activity and plasma membrane activity.[122] Nonfluorescent Calcein AM is enzymatically converted to fluorescent calcein (excitation ~495 nm, emission ~515 nm) by intracellular esterases present in live cells.[122] EthD–1 enters cells with a compromised membrane; once in the cell, EthD-1's fluorescence is increased 40-fold (excitation ~496 nm, emission ~635 nm) upon binding to nucleic acids, thus dead cells fluoresce red.[122]

The live/dead working solution was made by diluting calcein AM and EthD–1 in DPBS (containing calcium and magnesium). The following procedure is for the preparation of 3 mL of working solution. A volume of 2.25 μL of 2 mM EthD–1 was added to a sterile centrifuge tube and mixed with 2.996 mL of DPBS yielding a final EthD-1 concentration of 3 μM. To this same solution, 1.5 μL of 4 mM calcein AM was added, giving a final concentration of 1 μM calcein. The assay solution was vortexed to ensure it was thoroughly mixed. After incubation of the cells with nanoparticles for 1 h, laser exposure, removal of the nanoparticles, and further incubation, the media was removed and the live/dead assay working solution was added. The cells were incubated at room temperature for 30 min prior to imaging. The samples were imaged using an EVOS FL optical microscope that was equipped with red fluorescent protein (RFP) and green fluorescent protein (GFP) filter cubes.

Cytotoxicity studies of nanoparticle-exposed, laser-irradiated cells were also measured quantitatively using the MTT assay. Dark controls consisted of cells exposed to nanoparticles but not irradiated. After nanoparticle treatment and laser irradiation of

samples for 5 min, the nanoparticle/media was removed and the cells were washed three times with DPBS. The nanoparticle/media was also removed from the dark controls and they washed with DPBS three times. MTT solution (100 μL) was added to both the dark controls and the irradiated samples at a concentration of 0.5 mg/mL. The cells were incubated at 37 ^{o}C and 5 % CO_2 for 2.5 h. The MTT solution was then removed and replaced with 100 μL of DMSO. The sample wells were mixed for several minutes, prior to measuring the absorbance at 570 and 700 nm. Data were processed as described above in section 5.2.6.

5.3 Results and Discussion

5.3.1 Investigation of Photothermal Potential of Nanoparticles

The photothermal effect of aqueous suspensions of different concentrations, 50, 100, and 500 μg/mL, of P2 and P3 nanoparticles was determined. Figures 5-3A and 5-3B show the temperature change for both P2 and P3 after 5 min of laser irradiation at 2 W/cm^2 followed by 5 min of cooling. The study was conducted at room temperature. P2 suspensions exhibit temperature changes of approximately 12 – 34 ^{o}C at concentrations of 50 to 500 μg/mL, while temperatures of P3 suspensions increase approximately 14 – 35 ^{o}C at concentrations of 50 to 500 μg/mL. For both suspensions the temperature change increased as the concentration increased. From these data, it is determined that both P2 and P3 demonstrate enough temperature increase to substantially damage cells. An increase of 5 °C or greater leads to irreversible cell damage.[123] Both P2 and P3 demonstrated temperature changes of greater than 10 °C at the lowest concentration measured (50 μg/mL) when irradiated at a laser power of 2 W/cm^2. Both P2 and P3

demonstrated similar temperature changes at the same concentration. This similarity may be attributed to the size of the nanoparticles as well as the dopant: both P2 and P3 nanoparticles are similar in size, and both are doped with the same anionic polymer. This similarity would cause both polymers to have similar absorbance characteristics in the NIR region as well as similar intensities. As discussed in Chapter 4, the state of the polymer dramatically affects the absorbance; polymers in the neutral state show a blue shift in the absorbance in comparison to polymer in the oxidized state. These similar characteristics help explain the similarities in the heating of the material.

The photothermal heating properties of P2 and P3 were also compared to those of Clevios PH1000. Both P3 and Clevios PH1000 are composed of the same polymer; however, the charge stabilizer is different. Both P2 and P3 are stabilized by DBSA and PSS-co-MA, whereas Clevios PH1000 is stabilized by PSS alone. When comparing the temperature curves there is no significant temperature difference between the three polymeric nanoparticles indicating that they all behave relatively the same at the tested concentrations. The slight difference in the temperature profile of the three suspensions may be attributed to a few different factors such as the dopant used, the method used to oxidatively polymerize the polymer, slight difference in the extent of polymerization (molecular weight of the core polymers) as well as error in measuring the concentration of the nanoparticles.

The cycled heating of both P2 and P3 at 500 μg/mL shows no change in the photothermal heating of the material when irradiated with at 808 nm at a power density of 2 W/cm^2 over three cycles, as shown in Figure 5-4. The similarity after three repeated cycles suggest that both P2 and P3 nanoparticles are photostable and can be irradiated

multiple times without degrading. Photostability is an important characteristic for photothermal agents. Once accumulated at the tumor, photothermal agents should not degrade after irradiation because this may limit their use for multiple treatment cycles.

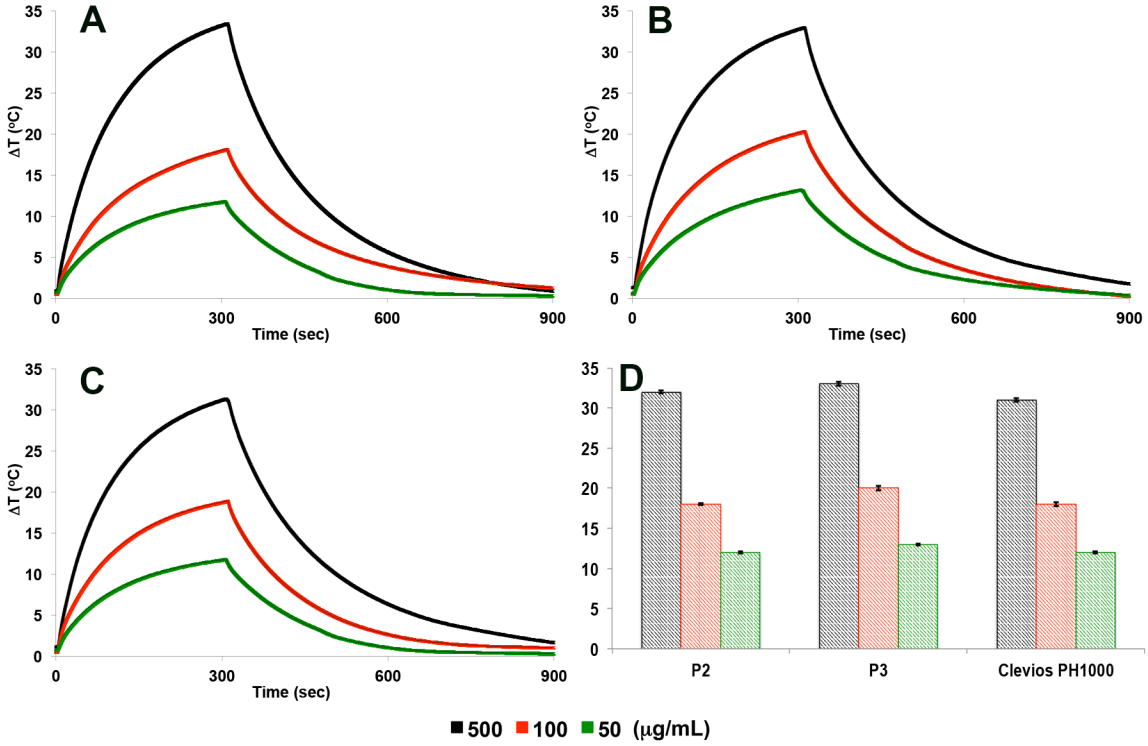

Figure 5-3. Temperature change curves of nanoparticle suspensions after 5 min of laser irradiation and subsequent cooling at concentrations of 500 (black), 100 (red), and 50 (green) μg/mL. **A.** P2. **B.** P3 **C.** Clevios PH1000. **D.** Bar graphs representative of the maximum temperature change at the three different concentrations. Data were averaged over three consecutive runs.

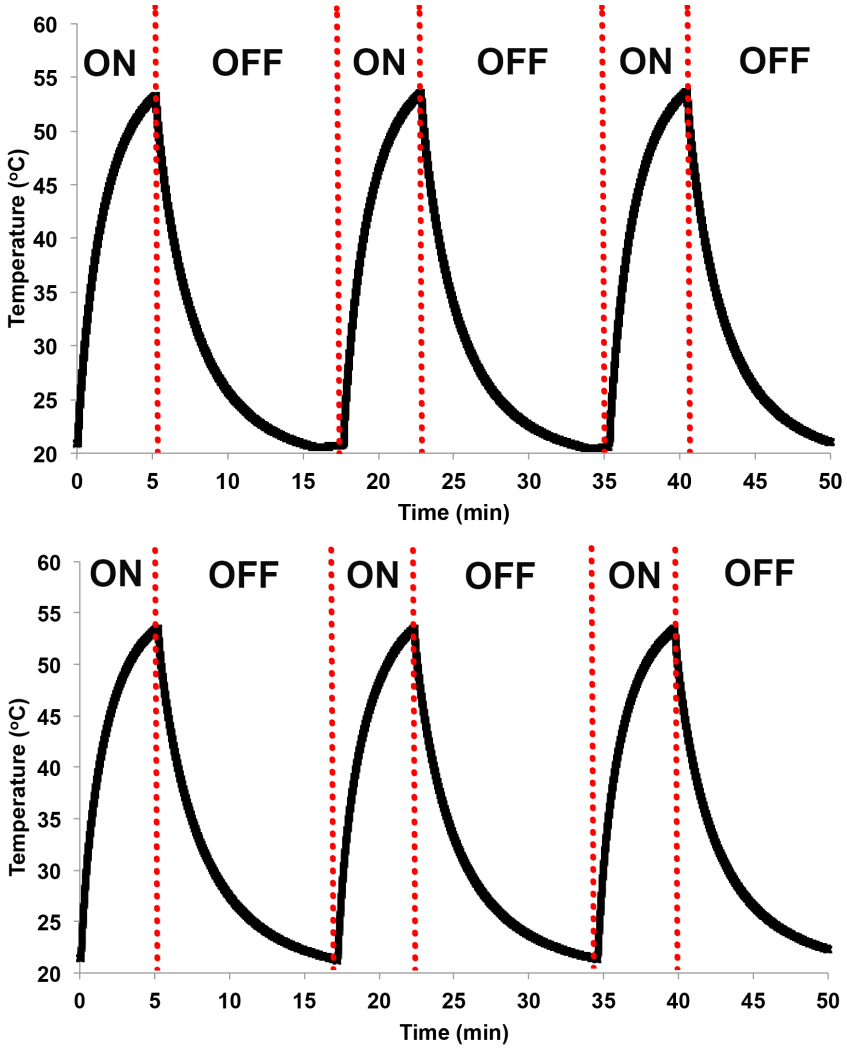

Figure 5-4. Cycled heating of nanoparticle suspensions (500 μg/mL). ON is indication of sample irradiation at 808 nm at a power density of 2 W/cm^2, while OFF is indication of laser being turned off, allowing the suspension to cool back to room temp. **Top**: P2. **Bottom**: P3.

5.3.2 Investigation of Photothermal Conversion Efficiency of Nanoparticles

The photothermal conversion efficient was determined as described in Section 5.2.3. First, the cooling curve data after powering the laser off, Figure 5-5A, was fit to Equation (12) to determine the heat transfer coefficient. P2, P3, Clevios PH1000, and GNRs were diluted in ultra pure water to an optical density of 0.45 at 808 nm. These

suspensions were then irradiated until the system reached a steady state at which the rate of heat gain due to photothermal conversion by the nanoparticles, water, and sample holder equals heat output to the surrounding, leading to a constant sample temperature. Finally, the suspensions were allowed to cool back to room temperature. The cooling data were plotted as ln(ΔT) vs. time. The slopes of the linear plots, $(-\Sigma C_p M_i/hA)^{-1}$, were then plugged into Equation (12) enabling the calculation of the product of the heat transfer coefficient, *h*, and the heat transfer surface area of the system, A. These values were then plugged into Equation (1). Using this method the photothermal conversion efficiency for P2 and P3 were calculated to be approximately 33% and 38% respectively, as shown in Figure 5-5B. The photothermal conversion efficiencies for Clevios PH1000 and GNRs were also determined experimentally to be 37% and 32% respectively.

Both P3 and Clevios PH1000 are composed of PEDOT polymers and have very similar conversion efficiencies. This may indicate that the stabilizer has no significant role in the conversion efficiency and the polymer itself is what dictates the heat conversion of the material. P2 showed a slightly lower conversion efficiency than the PEDOT samples. This may either be attributed to the extent of polymerization of P2, having less repeat units in comparison to the PEDOT polymers, or again this may be attributed to error in measuring the concentrations of the polymers. The GNRs demonstrated slightly less heating efficiency that the polymeric nanoparticles; the concentration was based on mass of the entire suspension (including excess surfactant present) and not necessarily reflective of the amount of gold in the sample. Therefore the heating efficiency of the gold to polymer ratio by mass may not be reflected in this data, and further studies would need to be conducted to determine the amount of heating

generated when comparing to the amount of gold per particle vs. the amount of polymer per particles.

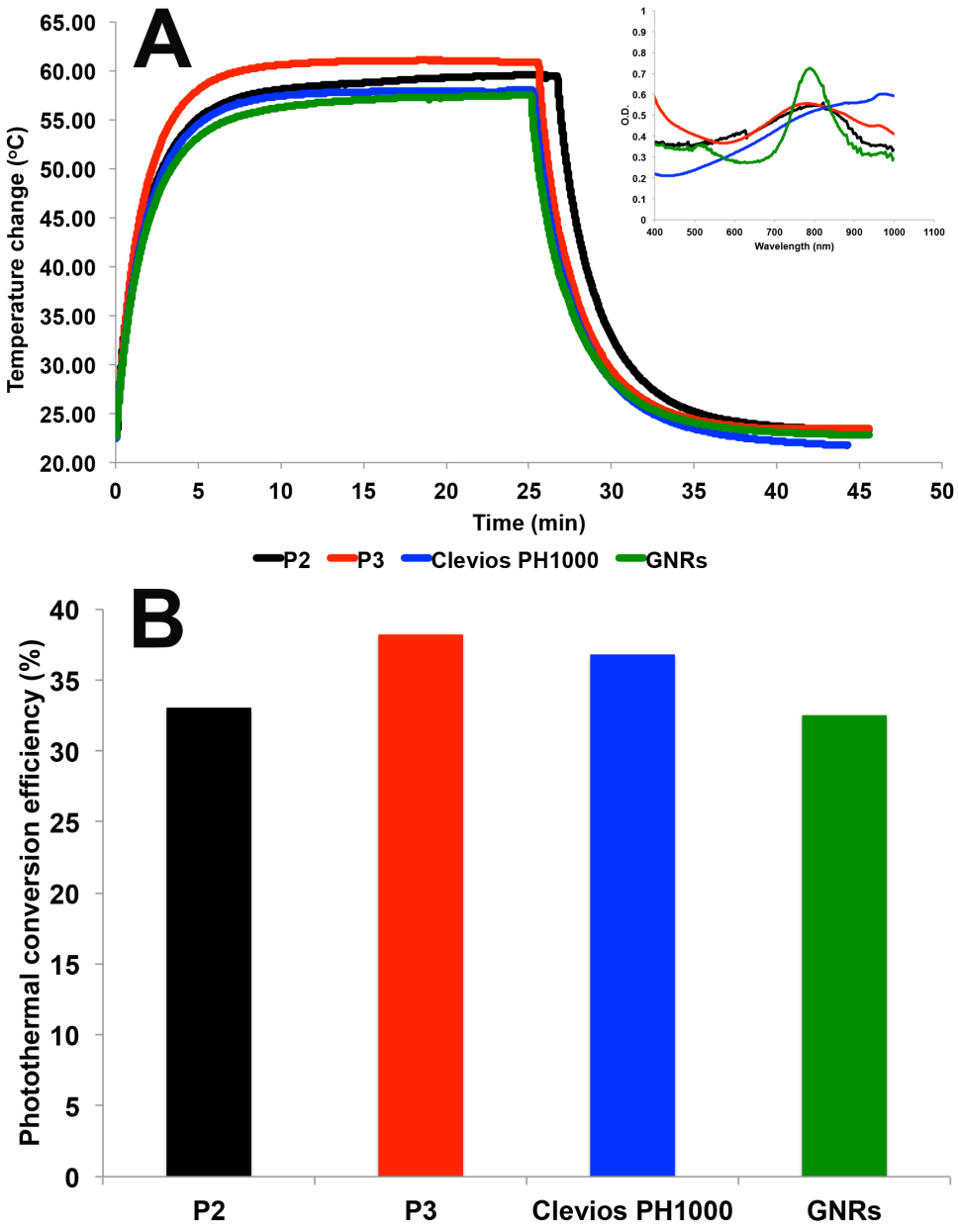

Figure 5-5. A. Temperature change of P2 (black) and P3 (red): samples were irradiated until equilibrium was reached. The laser was then turned off, and the suspensions were allowed to cool to room temperature. The data was used to determine the photothermal conversion efficiency. **B.** Bar graph of the photothermal conversion efficiency % of P2 (black) and P3 (red) at an optical density of 0.45 (inset graph).

5.3.3 Cytotoxicity

The cytotoxicity of the nanoparticles was determined *in vitro*. In this study, MDA-MB-231 breast cancer cells were used. The particles were sterile filtered and diluted in cell medium. The percent cell viability of cells after 24 h of exposure to either P2 or P3 nanoparticles with concentrations ranging from 500 to 0.2 μg/mL is shown in Figure 5-6. The data demonstrates toxicity at high nanoparticle concentrations only, with a percent cell viability less than 80% in relationship to the positive control (no nanoparticles). Below concentrations of ~55 μg/mL of P2 and P3, the nanoparticles are cytocompatible, with a percent cell viability of 80% or higher.

It is also important to note that there was no significant shift in the absorbance of the nanoparticles when suspended in media, as shown in Figure 5-7. This important characteristic shows that the nanoparticles are unaffected by the medias' environment (pH, high salt concentration) and can still be used as PT agents under these conditions.

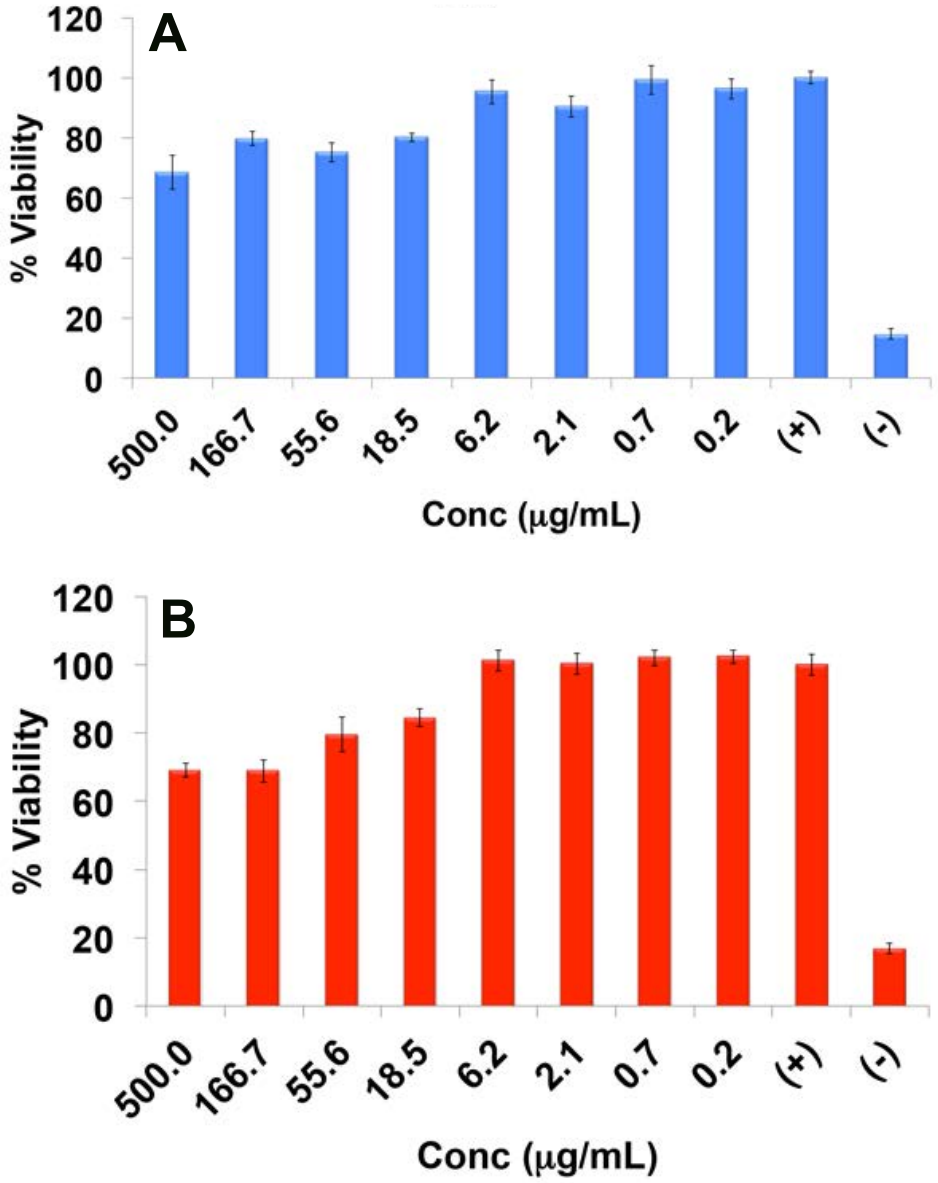

Figure 5-6. Percent viability charts of MDA-MB-231 cells exposed to varying concentrations of nanoparticles ranging from 0.2 to 500 µg/mL for 24 h. Positive control represents cells incubated in media, while negative controls are cells exposed to methanol. A. Viability of cells exposed to P2. B. Viability of cells exposed to P3. Error bars are standard deviation over several trials (n=6).

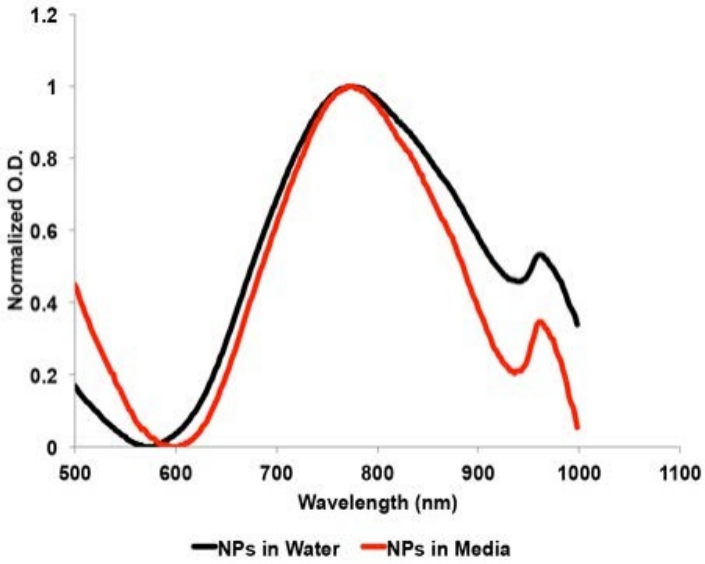

Figure 5-7. Absorbance of P3 nanoparticles in water (black) and in media (red) No significant difference in the absorbance is observed.

5.3.4 *In Vitro* Photothermal Ablation Study

P2 and P3 nanoparticles were diluted to a final concentration of 50 to 10 μg/mL in cell media containing HEPES and Streptomycin/Penicillin. The extent of cell death after 5, 10, and 15 min irradiation times was determined. Fluorescence microscopy images of cells stained with the live/dead assay which contains calcein AM and EthD-1 are shown in Figure 5-8. In these images, viable cells are stained green, while dead cells are stained red. The images shown are overlays containing both green and red channels. As can be seen from Figure 5-8, cells irradiated in the presence of nanoparticles present significant cell death. In contrast, cells exposed to nanoparticles in the absence of laser irradiation and cells irradiated in the absence of nanoparticles showed little if any cell death. Definitive cell death is observed upon irradiation of cells for 5 min in the presence of P2 or P3 nanoparticle concentrations of 10 and 50 μg/mL; in contrast, live cells are observed

in samples that contained only nanoparticles at the same concentrations of 10 and 50 μg/mL but that were not irradiated. This study was also done at a max concentration of 500 μg/mL and a minimum concentration of 0.5 μg/mL. Cell death was observed in all concentration above 50 μg/mL. At concentrations of 0.5 and 1 μg/mL cell death is still observed after 5 min of irradiation, however there are still live cells visible, Figure 5-9. However, when 0.5 and 1 μg/mL are irradiated for 10 min a significant amount of cell death is observed, Figure 5-9.

The percent viability was also determined for the irradiated samples using the MTT assay, as shown in Figure 5-10. As described in the procedure, the cells were irradiated in a temperature-controlled environment; however, the CO_2 levels were not maintained, and this is believed to have led to some of the cells detaching from the plate and thereby increasing the percent error within each condition. Nevertheless, the samples irradiated in the presence of nanoparticles suffered a significant decrease in percent viability in comparison to their respective dark controls. In order to determine the amount of cell death caused by the NIR light itself, cells were irradiated without the presence of nanoparticles. After irradiation for 15 min, very little cell death was observed as indicated by the ~90% viability. We were unable to measure the percent viability of both the 0.5 and 1 μg/mL samples.

This data confirm that the particles themselves are generating enough heat to initiate cell death. The mechanism of cell death was not explored in this study; however, previous studies on gold nanorods, have extensively studied the cell death mechanism.[124,125] It was first reported by Tong *et al*. that the mechanism of cell death caused by heating from internalized gold nanorods was by apoptosis.[124] However, more

recently in a study done by Patini *et al*. it was determined that the cell death mechanism is dependent on the gold nanoparticles internalization within the cell.[125] Particles that have only reached the cell membrane tend to induce cell necrosis while particles that are internalized near organelles tend to induce cell apoptosis.[125] While these studies can be correlated to other gold nanoparticles, to our knowledge there have not been any studies investigating cell death mechanisms associated with photothermal therapy enabled by polymeric nanoparticles.

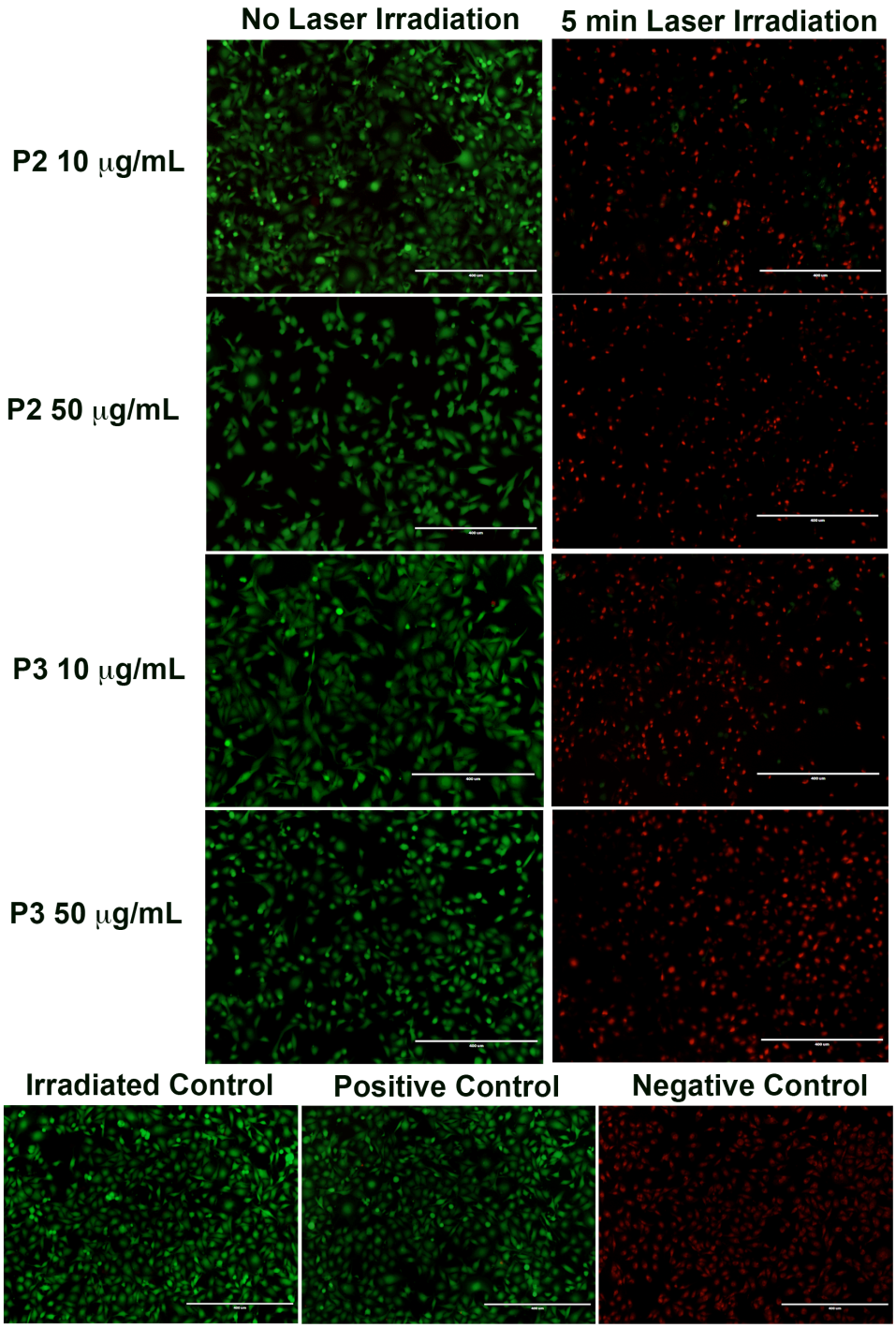

Figure 5-8. Optical microscopy images of cells irradiated (5 min) and not irradiated (0 min) containing 50 or 10 μg/mL of P2 or P3. Green color is indication of live cells, and red indicates dead cells. The irradiated control contained no nanoparticles and was irradiated for 15 min. The positive control did not contain nanoparticles and was not irradiated. The negative control consists of methanol-fixed cells.

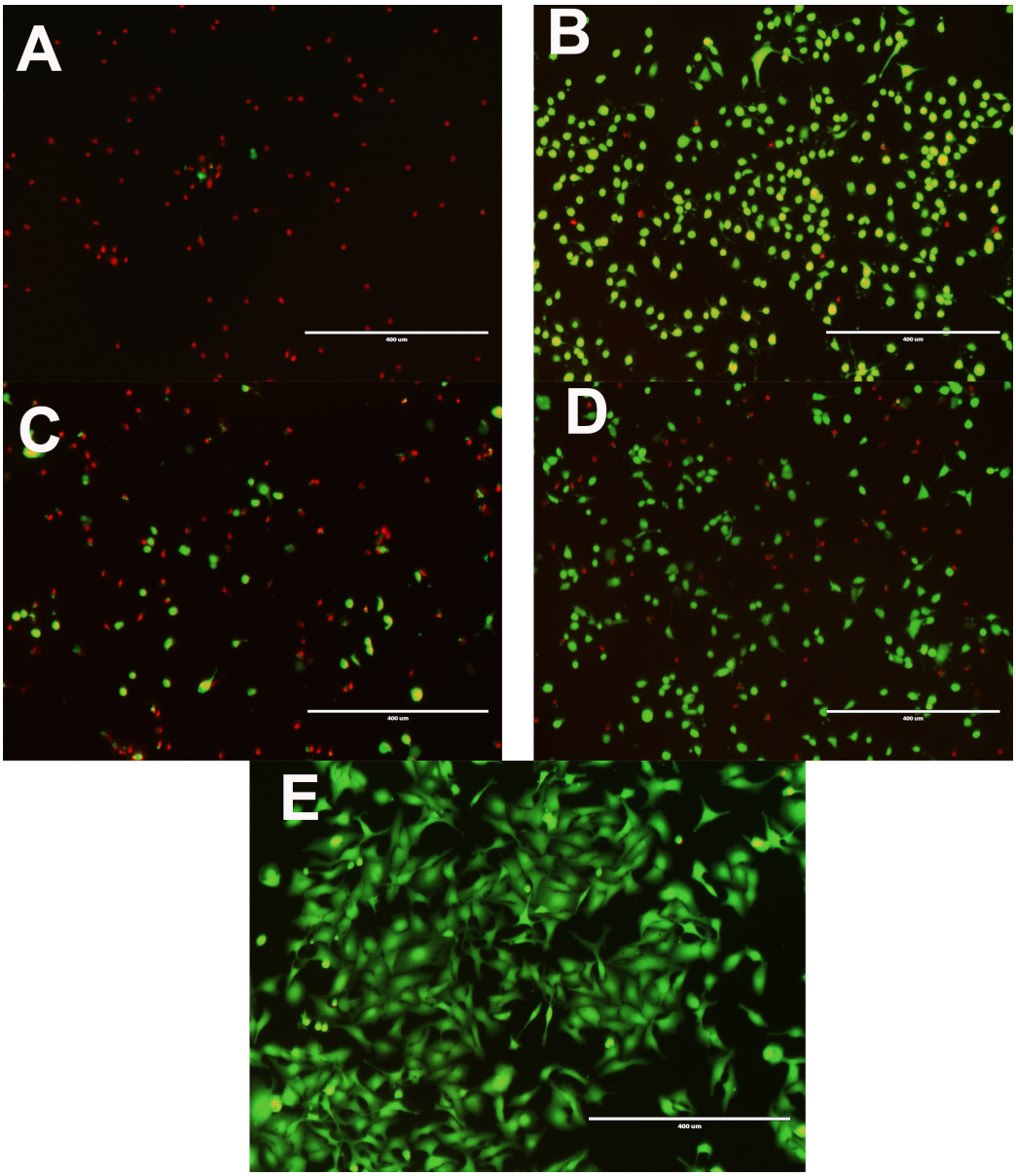

Figure 5-9. Fluorescence microscopy images of MDA-MB-231 cells. Green color is indication of live cells, and red indicates dead cells. A. 10 min irradiation at 1 μg/mL of P2 nanoparticles B. 5 min irradiation at 1 μg/mL of P2 nanoparticles C. 10 min irradiation at 0.5 μg/mL of P2 nanoparticles D. 5 min irradiation at 0.5 μg/mL E. Cell incubated with P2 nanoparticles at a concentration of 1 μg/mL but were not exposed to irradiation.

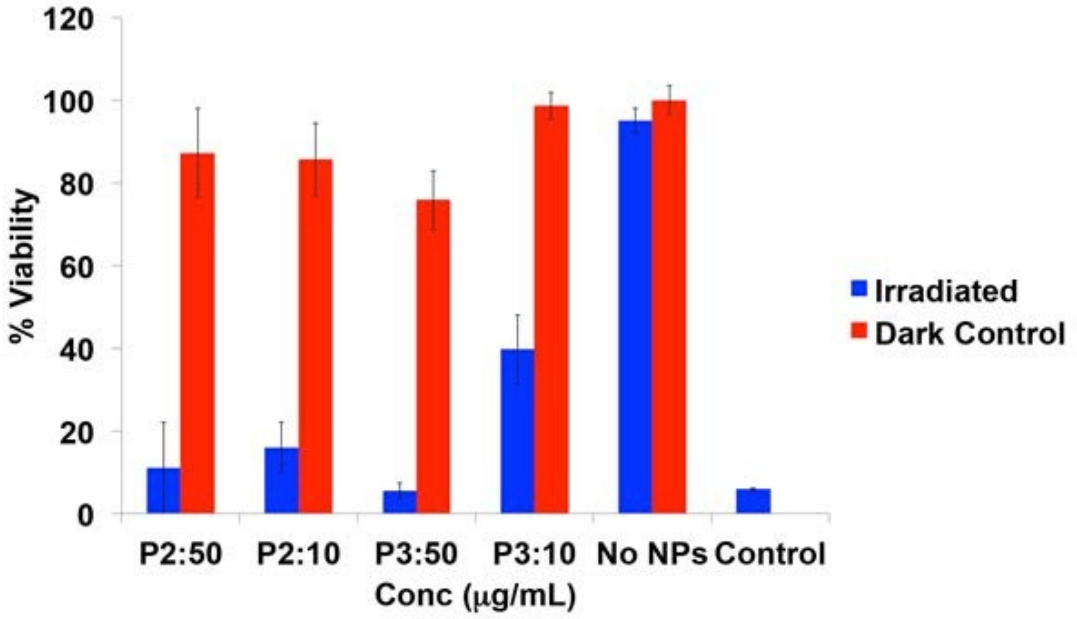

Figure 5-10. Percent viability of cells irradiated and not irradiated (dark control) in the presence of nanoparticles. Error bars are standard deviation over four trials

5.4 Conclusions

The photothermal effect of the nanoparticles was investigated in water. It was determined that there was sufficient heating for both P2 and P3 at 50, 100, and 500 μg/mL to cause photothermal ablation. There was no significant difference in the heating of three polymer nanoparticles at the tested concentrations. The slight change in the heating profile may be attributed to extent of oxidation of the polymer as well as error in measuring the concentration of the particles. Both P2 and P3 also showed photostability after three cycled heating intervals.

The photothermal conversion efficiency was determined for P2, P3, Clevios PH1000 and GNRs. It was determined that the photothermal efficiency were ~33%, ~38%, ~37%, and ~32% for P2, P3, Clevios PH100, and GNRs respectively. The

similarities of the conversion efficiencies for P3 and Clevios PH1000 may be attributed to the similarity in the core of the particles.

Cytotoxicity studies showed that at concentrations below 55 μg/mL, both P2 and P3 are nontoxic to breast cancer cells resulting in a percent viability greater than 80%. The absorbance of the nanoparticles in media was measured and compared to particle suspended in water. It was determined that the media has no effect on the absorbance as no visible shift was observed in the spectrum.

Lastly the photothermal ablation *in vitro* was investigated using breast cancer cells. Cell death was observed at concentration of 10 and 50 μg/mL for P2 and P3, within 5 min of laser exposure. Significant differences in the cell death were observed between irradiated samples vs. dark controls. It was also determined that cell death was attributed to the heat generated by the nanoparticles and not to sole exposure to NIR radiation, as is evident from the lack of cell death upon irradiation of a control sample in the absence of nanoparticles. Both P2 and P3 particles have the potential to be used as PT agents, showing great photostability, and the ability to initiate cell death when irradiated at nontoxic levels.

6 CONCLUSTIONS AND FUTURE WORK

6.1 Synthesis of 1,4-Bis(3,4-ethylenedioxythienyl)-2,5-dialkoxybenzenes

In this portion of the study, we successfully synthesized two extended conjugated monomers (M1 and M2) using Negishi coupling. Electroactive polymer films were prepared electrochemically. Oxidation and reduction potentials of both polymer films were determined and compared to similar previously reported extended conjugation polymers. The role of an electron withdrawing group on the oxidation potential of the polymer was explored; it was determined that by adding the alkoxy ester pendant group the oxidation potential of the monomer was lowered compared to alkoxy pendant groups. In an effort to further understand the effect of the electron withdrawing ester group on the conjugated backbone, we attempted to synthesize a third monomer with an ester group directly on the monomer backbone and compare that to M2. However, we were unsuccessful at synthesizing dihexyl 2,5-bis(2,3-dihydrothieno[3,4-b][1,4]dioxin-5-yl) terephthalate using two different methods: Negishi and Stille coupling. The oxidized polymers P1 and P2, prepared from M1 and M2 respectively, both demonstrated a strong absorbance in the near infrared (NIR) region whereas the neutral polymers were blue-shifted and did not absorb significantly in the NIR.

6.2 Nanoparticle Synthesis

In this portion of the study we successfully prepared nanoparticles composed of P1, P2, and poly(3,4-ethylenedioxythiophene) (P3). The nanoparticles were prepared using an emulsion polymerization process. Several different approaches were attempted in an effort to achieve sub-100 nm spherical nanoparticles. In our first trials, several different

stabilizers were used in an attempt to stabilize the polymer in aqueous media. Using this method we found that only Triton X-100 was able to stabilize the polymer in the oxidized state in aqueous media, enabling it to present a strong absorbance in the NIR region. The nanoparticles synthesized using this method were rod-shaped rather than spherical. This morphology is attributed to the rigidity of the polymer backbone restricting the polymer from coiling around itself. Using a two-surfactant method, where stabilizers were included in both the organic and aqueous phases, we were able to produce sub-100 nm spherical nanoparticles. In our study, 4-dodecylbenzenesulfonic acid (DBSA) was used as a stabilizer in the organic phase, and poly(4-styrenesulfonic acid-co-maleic acid) sodium salt (PSS-co-MA) was used in the aqueous phase. Using this method, both M2 and M3 were successfully polymerized yielding P2 and P3 nanoparticles. The nanoparticle suspensions for both P2 and P3 demonstrated a strong absorbance in the NIR region.

6.3 Photothermal Effect

The nanoparticles synthesized in the previous section were further investigated as photothermal agents. The photothermal effect was determined by irradiating for both P2 and P3 nanoparticles using an 808-nm laser at a power density of 2 W/cm^2. It was determined that both P2 and P3 demonstrated a significant temperature increase at 50, 100, and 500 μg/mL indicating that they could be used as PT agents. In both polymer suspensions it was found that as the concentration decreased, so did the temperature change enabled by photothermal transduction. The two synthesized polymer suspension were compared to Clevios PH1000, a commercially available PEDOT:PSS suspension. All three of the polymer suspensions demonstrated very similar heating profiles at the same concentrations. After repeated cycled heating, P2 and P3 were also found to be

photostable as there was no decrease in the photothermal conversion enabled by the suspensions after three heating/cooling cycles when irradiated with a 808-nm laser at power density of 2 W/cm^2. The photothermal conversion efficiency was also determined for P2 and P3 using an equation derived by Roper *et al*.[120] The photothermal conversion efficiency for Clevios PH1000 and gold nanorods (GNRs) was also experimentally determined and compared to that of P2 and P3. All three of the polymer suspensions demonstrated very similar conversion efficiencies. The GNRs that we tested demonstrated slightly less conversion efficiency than the polymer nanoparticles.

Once the photothermal effect and efficiency were determined for P2 and P3, the therapeutic potential of these nanoparticles was further investigated *in vitro*. The cytotoxicity of the nanoparticle suspensions was investigated using MDA-MB-231 breast cancer cells. The cells were exposed to the nanoparticles at concentrations of 0.2 to 500 μg/mL for 24 h. We observed that at concentrations at or below 55 μg/mL the nanoparticles are nontoxic. It was also observed that nanoparticles suspended in media still demonstrate a strong absorbance in the NIR region. Lastly, *in vitro* photothermal ablation of cancer cells was tested. At concentrations of 10 and 50 μg/mL, significant cell death is observed in comparison to controls. This demonstrates that both P2 and P3 have the potential to be used at photothermal agents at concentrations that are nontoxic.

6.4 Future Work

In the future the synthesis of dihexyl 2,5-bis(2,3-dihydrothieno[3,4-b][1,4]dioxin-5-yl) terephthalate may be further explored, for example by following the indium-based coupling reaction reported by Sarandeses *et al*.[126] In order to increase processability of the extended conjugated polymers, the use of metal-mediated polymerization reaction

which helps to increase regioregularity could be used to in turn increase the solubility of the polymer in organics. Rieke *et al.* reported the polymerization of zinc modified 3-alkylthiophene yielding poly(3-alkylthiophene) by Negishi coupling.[127] This method resulted in 98.5% regioregular polymer.[127] Using this method will allow for alternative nanoparticle preparation routes that require less toxic starting materials and fewer steps to achieve nanoparticles. For example, nanoparticles could be prepared via nanoprecipitation or emulsion/solvent evaporation methods through simple protocols starting with polymer solutions. Post-polymerization functionalization of the polymer to covalently attach poly(ethylene glycol) (PEG) to the side chains of the polymer via transesterification can also help to improve polymer and nanoparticle solubility as well as biocompatibility.

The method used for the nanoparticle process developed in this study still has room for improvement. This includes the ability to control size of the nanoparticles; furthermore producing nanoparticle suspensions with consistent low polydispersity is an important factor that needs to be optimized. The stability of the nanoparticles in different conditions, including pH and temperature changes, should also be investigated in more detail.

Another area that should be further explored is the mechanism of interaction of the conductive polymers with the stabilizers used in the two-surfactant method for nanoparticle preparation. This could be accomplished using spectroscopy methods such as infrared spectroscopy in an effort to see bond interactions. In an effort to better understand the interaction of PEDOT with PSS-co-MW, Han *et al*. reported the use of x-

ray diffraction spectroscopy.[128] This can be another valuable study done in order to better understand the properties of the nanoparticles herein developed.

The nanoparticle design can further be enhanced by surface modification with PEG to enhance biocompatibility of the nanoparticles. PEG-amine can be covalently bound to the carboxylic acids on the surface of the nanoparticles using carbodiimide crosslinking chemistry. Specifically, the carboxylic acids on the surface of the nanoparticles from the maleic acid functional groups found on the strongly adsorbed PSS-co-MA stabilizer can be used to bind to amine-functionalized PEG. Another approach that can be used to functionalize the surface of the nanoparticles with PEG is by using a layer-by-layer method where the nanoparticles are first coated with positively charged poly(allylamine) and then coated with a negatively charged layer of poly(acrylic acid). These two layers can then be crosslinked by amide formation.[61] Once crosslinked, PEG can then be covalently attached to the surface of the nanoparticles.[61]

There are still many studies that need to be conducted to further understand how P2 and P3 enter the cancer cells and the mechanism of cell death induced by the irradiated nanoparticles. In order to study how the nanoparticles enter the cells, the particles can be loaded with a fluorescent dye during the nanoparticle preparation process. Fluorescence microscopy can then be used to track where the particles are within the cells at different time points. This would make it possible to determine the optimal incubation time for particles to migrate pass the cell membrane and to study how their ultimate intracellular distribution affects their ability to kill cancer cells via photothermal ablation. To investigate the mechanism of cell death caused by photothermal therapy using P2 and P3 as photothermal agents, apoptosis assays could be carried out to determine the extent of

apoptosis vs. necrosis induced in the cells. The relationship of these mechanisms to the nanoparticle dose, nanoparticle intracellular distribution, and irradiation dose/rate could then be determined.

Some other potential applications of these conductive polymeric nanoparticles are laser triggered drug delivery, localized cell heating, and self healing materials. By using the nanoparticle preparation methods we described in this work, one can easily load hydrophobic drugs or dyes. By adding the drug or dye to the organic phase during the preparation of the nanoparticles the hydrophobic material will be encapsulated with in the conductive polymer. With the conductive polymeric nanoparticles acting as a drug delivery vehicle, the chemotherapeutic has the potential to be release upon irradiation. This would allow for the dual treatment of photothermal therapy and controlled drug release. The nanoparticless can also be incorporated into bulk material creating composites. Once nanoparticles are loaded the material can be irradiated generating localized heat within the material. This could allow for self healing material.

6.5 Final Conclusions

In this work, we demonstrated the successful synthesis of conductive polymer nanoparticles, one of which is made from a polymer that had not been previously reported. The nanoparticles demonstrated a significant temperature change when irradiated with an NIR laser. The nanoparticle suspensions also were found to provide a photothermal conversion efficiency greater than 30%. Cell viability was above 80% after a 24-hour exposure to concentrations equal to or below 55 μg/mL of either P2 or P3 nanoparticles. The particles were also demonstrated to be effective photothermal agents *in vitro* at concentrations as low as 10 μg/mL. Although there are still many studies that

need to be conducted to better understand the properties of these polymeric nanoparticles, this work gave us a foundational understanding of how these materials behave and demonstrated their potential as photothermal agents for cancer treatment.

APPENDIX SECTION

APPENDIX A: ^{1}H NMR of M1

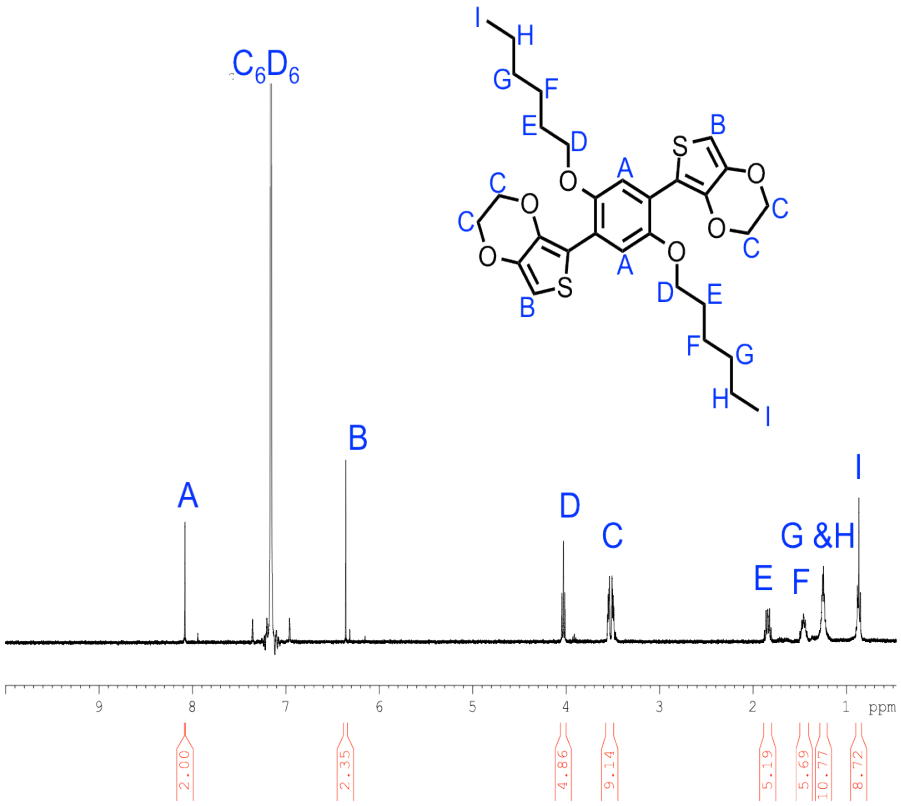

APPENDIX B: ^{1}H NMR of M2

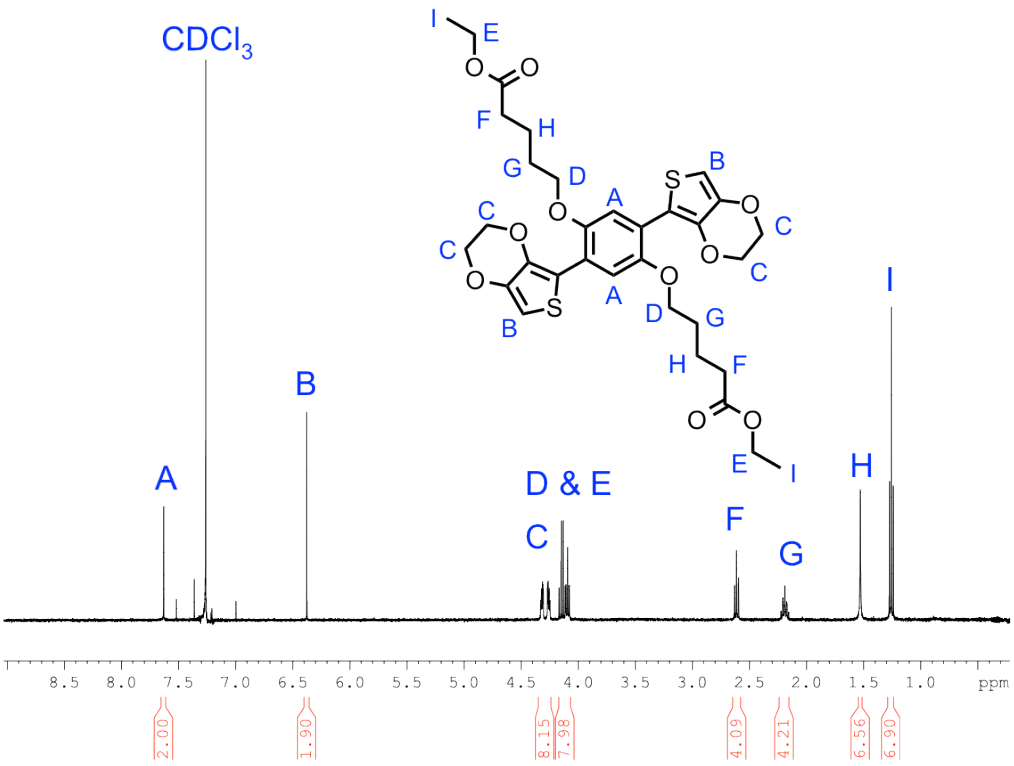

REFERENCES

(1) American Cancer Society. *Cancer Facts & Figures 2015*; Atlanta, 2015.

(2) Lang, L. Cancer costs projected to reach at least $158 billion in 2020. www.cancer.goc/newscenter/newsfromnci/2011/CostCancer2020 (accessed Oct 1, 2015).

(3) Deasy, S.; Szczepanek, K.; Hunter, K. Targeting Metastatic Breast Cancer: Problems and Potential. *F1000Research* **2015**, *4*.

(4) Blok, E. J.; Derks, M. G. M.; Hoeven, J. J. M. Van Der; Velde, C. J. H. Van De; Kroep, J. R. Extended Adjuvant Endocrine Therapy in Hormone-Receptor Positive Early Breast Cancer : Current and Future Evidence. *Cancer Treat. Rev.* **2015**, *41*, 271–276.

(5) Brannon-Peppas, L.; Blanchette, J. O. Nanoparticle and Targeted Systems for Cancer Therapy. *Adv. Drug Deliv. Rev.* **2012**, *64*, 206–212.

(6) Byrne, J. D.; Betancourt, T.; Brannon-Peppas, L. Active Targeting Schemes for Nanoparticle Systems in Cancer Therapeutics. *Adv. Drug Deliv. Rev.* **2008**, *60*, 1615–1626.

(7) Hahn, M. A.; Singh, A. K.; Sharma, P.; Brown, S. C.; Moudgil, B. M. Nanoparticles as Contrast Agents for in-Vivo Bioimaging: Current Status and Future Perspectives. *Anal. Bioanal. Chem.* **2011**, *399*, 3–27.

(8) Lowery, A. R.; Gobin, A. M.; Day, E. S.; Halas, N. J.; West, J. L. Immunonanoshells for Targeted Photothermal Ablation of Tumor Cells. *Int. J. Nanomedicine* **2006**, *1*, 149–154.

(9) Tan, S. J.; Campolongo, M. J.; Luo, D.; Cheng, W. Building Plasmonic Nanostructures with DNA. *Nat. Nanotechnol.* **2011**, *6*, 268–276.

(10) Qin, Z.; Bischof, J. C. Thermophysical and Biological Responses of Gold Nanoparticle Laser Heating. *Chem. Soc. Rev.* **2012**, *41*, 1191–1217.

(11) Hill, T. K.; Abdulahad, A.; Kelkar, S. S.; Marini, F. C.; Long, T. E.; Provenzale, J. M.; Mohs, A. M. Indocyanine Green-Loaded Nanoparticles for Image-Guided Tumor Surgery. *Bioconjug. Chem.* **2015**.

(12) Wilczewska, A. Z.; Niemirowicz, K.; Markiewicz, K. H.; Car, H. Nanoparticles as Drug Delivery Systems. *Pharmacol Rep* **2012**, *64*, 1020–1037.

(13) Pillai, G. Nanomedicines for Cancer Therapy : An Update of FDA Approved and Those under Various Stages of Development. *SOJ Pharm Pharm Sci* **2014**, *1*, 13.

(14) Taurin, S.; Greish, K. Enhanced Vascular Permeability in Solid Tumors: A Promise for Anticancer Nanomedicine. In *Tight Junctions in Cancer Metastasis*; Martin, T. A.; Jiang, W. G., Eds.; Springer, **2013**; Vol. 19, pp. 81–118.

(15) Cho, K.; Wang, X.; Nie, S.; Chen, Z. G.; Shin, D. M. Therapeutic Nanoparticles for Drug Delivery in Cancer. *Clin. Cancer Res.* **2008**, *14*, 1310–1316.

(16) Iyer, A. K.; Khaled, G.; Fang, J.; Maeda, H. Exploiting the Enhanced Permeability and Retention Effect for Tumor Targeting. *Drug Discov. Today* **2006**, *11*, 812–818.

(17) Betancourt, T. Targetable Biodegradable Nanoparticles for Delivery of Chemotherapeutic and Imaging Agents to Ovarian Cancer, University of Texas at Austin, **2007**.

(18) Friedman, A. D.; Claypool, S. E.; Liu, R. The Smart Targeting of Nanoparticles. *Curr. Pharm. Des.* **2013**, *19*, 6315–6329.

(19) Hermanson, G. *Bioconjugate Techniques*; 2nd ed.; Elsevier, **2008**.

(20) Barker, K.; Rastogi, S.; Dominguez, J.; Cantu, T.; Brittain, W.; Irvin, J.; Betancourt, T. Biodegradable DNA-Enabled Poly(ethylene Glycol) Hydrogels Prepared by Copper-Free Click Chemistry. *J. Biomater. Sci. Polym. Ed.* **2015**, 1–3.

(21) Nieves, D. J.; Azmi, N. S.; Xu, R.; Lévy, R.; Yates, E. A.; Fernig, D. G. Monovalent Maleimide Functionalization of Gold Nanoparticles via Copper-Free Click Chemistry. *Chem. Commun. (Camb).* **2014**, *50*, 13157–13160.

(22) Lidke, D. S.; Nagy, P.; Heintzmann, R.; Arndt-Jovin, D. J.; Post, J. N.; Grecco, H. E.; Jares-Erijman, E. A.; Jovin, T. M. Quantum Dot Ligands Provide New Insights into erbB/HER Receptor-Mediated Signal Transduction. *Nat. Biotechnol.* **2004**, *22*, 198–203.

(23) Bertrand, N.; Wu, J.; Xu, X.; Kamaly, N.; Farokhzad, O. C. Cancer Nanotechnology: The Impact of Passive and Active Targeting in the Era of Modern Cancer Biology. *Adv. Drug Deliv. Rev.* **2014**, *66*, 2–25.

(24) Tai, W.; Mahato, R.; Cheng, K. The Role of HER2 in Cancer Therapy and Targeted Drug Delivery. *J. Control. Release* **2010**, *146*, 264–275.

(25) Jang, M.; Yoon, Y. Il; Kwon, Y. S.; Yoon, T. J.; Lee, H. J.; Hwang, S. Il; Yun, B. La; Kim, S. M. Trastuzumab-Conjugated Liposome-Coated Fluorescent Magnetic Nanoparticles to Target Breast Cancer. *Korean J. Radiol.* **2014**, *15*, 411–422.

(26) American Cancer Society. *Breast Cancer*; **2015**.

(27) Jordan, A.; Scholz, R.; Wust, P.; Fa, H.; Felix, R. Magnetic Fluid Hyperthermia (MFH): Cancer Treatment with AC Magnetic Field Induced Excitation of Biocompatible Superparamagnetic Nanoparticles. *J. Magn. Magn. Mater.* **1999**, *201*, 413–419.

(28) Laurent, S.; Dutz, S.; Häfeli, U. O.; Mahmoudi, M. Magnetic Fluid Hyperthermia: Focus on Superparamagnetic Iron Oxide Nanoparticles. *Adv. Colloid Interface Sci.* **2011**, *166*, 8–23.

(29) Huang, X.; Jain, P. K.; El-Sayed, I. H.; El-Sayed, M. A. Plasmonic Photothermal Therapy (PPTT) Using Gold Nanoparticles. *Lasers Med. Sci.* **2008**, *23*, 217–228.

(30) Gilchrist, R. K.; Medal, R.; Shorey, W. D.; Hanselman, R. C.; Parrott, J. C.; Taylor, C. B. Selective Inductive Heating of Lymph Nodes *. *Ann. Surg.* **1957**, *146*, 596–606.

(31) Deatsch, A. E.; Evans, B. A. Heating Efficiency in Magnetic Nanoparticle Hyperthermia. *J. Magn. Magn. Mater.* **2013**, *354*, 163–172.

(32) Reddy, L. H.; Arias, J. L.; Nicolas, J.; Couvreur, P. Magnetic Nanoparticles: Design and Characterization, Toxicity and Biocompatibility, Pharmaceutical and Biomedical Applications. *Chem. Rev.* **2012**, *112*, 5818–5878.

(33) Chatterjee, D. K.; Fong, L. S.; Zhang, Y. Nanoparticles in Photodynamic Therapy: An Emerging Paradigm. *Adv. Drug Deliv. Rev.* **2008**, *60*, 1627–1637.

(34) Konan, Y. N.; Gurny, R.; Allémann, E. State of the Art in the Delivery of Photosensitizers for Photodynamic Therapy. *J. Photochem. Photobiol. B Biol.* **2002**, *66*, 89–106.

(35) Ormond, A. B.; Freeman, H. S. Dye Sensitizers for Photodynamic Therapy. *Materials (Basel).* **2013**, *6*, 817–840.

(36) Del Pino, P.; Pelaz, B. Hyperthermia Using Inorganic Nanoparticles. In *Nanobiotechnology: Inorganic Nanoparticles vs Organic Nanoparticles*; De la Fuente, J. M.; Grazu, V., Eds.; Elsevier, **2013**; pp. 309–335.

(37) Huang, X.; Kang, B.; Qian, W.; Mackey, M. A.; Chen, P. C.; Oyelere, A. K.; El-Sayed, I. H.; El-Sayed, M. A. Comparative Study of Photothermolysis of Cancer Cells with Nuclear-Targeted or Cytoplasm-Targeted Gold Nanospheres: Continuous Wave or Pulsed Lasers. *J. Biomed. Opt.* **2010**, *15*, 058002.

(38) Khosroshahi, M. E.; Hassannejad, Z.; Firouzi, M.; Arshi, A. R. Nanoshell-Mediated Targeted Photothermal Therapy of HER2 Human Breast Cancer Cells Using Pulsed and Continuous Wave Lasers: An in Vitro Study. *Lasers Med. Sci.* **2015**, *30*, 1913–1922.

(39) Pustovalov, V. K.; Smetannikov, A. S.; Zharov, V. P. Photothermal and Accompanied Phenomena of Selective Nanophotothermolysis with Gold Nanoparticles and Laser Pulses. *Laser Phys. Lett.* **2008**, *5*, 775–792.

(40) Chen, W. R.; Adams, R. L.; Bartels, K. E.; Nordquist, R. E. Chromophore-Enhanced in Vivo Tumor Cell Destruction Using an 808-Nm Diode Laser. *Cancer Lett.* **1995**, *94*, 125–131.

(41) Diven, D. G.; Pohl, J.; Motamedi, M. Dye-Enhanced Diode Laser Photothermal Ablation of Skin. *J. Am. Acad. Dermatol.* **1996**, *35*, 211–215.

(42) Chen, W. R.; Adamsc, R. L.; Heaton, S.; Dickeyd, D. T.; Bartelsd, K. E.; Nordquistc, R. E. CANCER Interaction Using an 808-Nm Diode Laser. *Cancer Lett.* **1995**, *88*, 15–19.

(43) Huang, X.; Jain, P. K.; El-Sayed, I. H.; El-Sayed, M. A. Plasmonic Photothermal Therapy (PPTT) Using Gold Nanoparticles. *Lasers Med. Sci.* **2008**, *23*, 217–228.

(44) Huang, X.; El-Sayed, M. A. Gold Nanoparticles: Optical Properties and Implementations in Cancer Diagnosis and Photothermal Therapy. *J. Adv. Res.* **2010**, *1*, 13–28.

(45) Jain, P. K.; Lee, K. S.; El-Sayed, I. H.; A., E.-S. M. Calculated Absorption and Scattering Properties of Gold Nanoparticles of Different Size, Shape, and Composition: Applications in Biological Imaging and Biomedicine. *J. Phys. Chem. B* **2006**, *110*, 7238–7248.

(46) Oldenburg, S. J.; Averitt, R. D.; Westcott, S. L.; Halas, N. J. Nanoengineering of Optical Resonances. *Chem. Phys. Lett.* **1998**, *288*, 243–247.

(47) Loo, C.; Lin, A.; Hirsch, L.; Lee, M.-H.; Barton, J.; Halas, N.; West, J.; Drezek, R. Nanoshell-Enabled Photonics-Based Imaging and Therapy of Cancer. *Technol. Cancer Res. Treat.* **2004**, *3*, 33–40.

(48) Hirsch, L. R.; Jackson, J. B.; Lee, a.; Halas, N. J.; West, J. L. A Whole Blood Immunoassay Using Gold Nanoshells. *Anal. Chem.* **2003**, *75*, 2377–2381.

(49) Huang, X.; El-Sayed, I. H.; Qian, W.; El-sayed, M. A. Cancer Cell Imaging and Photothermal Therapy in the Near-Infrared Region by Using Gold Nanorods. *Jacs* **2006**, *128*, 2115–2120.

(50) Pattani, V. P.; Tunnell, J. W. Nanoparticle-Mediated Photothermal Therapy: A Comparative Study of Heating for Different Particle Types. *Lasers Surg. Med.* **2012**, *44*, 675–684.

(51) Cobley, C. M. Targeting Gold Nanocages to Cancer Cells for Photothermal Destruction and Drug Delivery. *Expert Opin Drug Deliv.* **2010**, *7*, 577–587.

(52) Yavuz, M. S.; Cheng, Y.; Chen, J.; Cobley, C. M.; Zhang, Q.; Rycenga, M.; Xie, J.; Kim, C.; Song, K. H.; Schwartz, A. G.; *et al.* Gold Nanocages Covered by Smart Polymers for Controlled Release with near-Infrared Light. *Nat. Mater.* **2009**, *8*, 935–939.

(53) Chen, J.; Wang, D.; Xi, J.; Au, L.; Siekkinen, A.; Warsen, A.; Li, Z. Y.; Zhang, H.; Xia, Y.; Li, X. Immuno Gold Nanocages with Tailored Optical Properties for Targeted Photothermal Destruction of Cancer Cells. *Nano Lett.* **2007**, *7*, 1318–1322.

(54) Rengan, A. K.; Kundu, G.; Banerjee, R.; Srivastava, R. Gold Nanocages as Effective Photothermal Transducers in Killing Highly Tumorigenic Cancer Cells. *Part. Part. Syst. Charact.* **2014**, *31*, 398–405.

(55) Wang, C.; Xu, L.; Liang, C.; Xiang, J.; Peng, R.; Liu, Z. Immunological Responses Triggered by Photothermal Therapy with Carbon Nanotubes in Combination with Anti-CTLA-4 Therapy to Inhibit Cancer Metastasis. *Adv. Mater.* **2014**, 8154–8162.

(56) Moon, H. K.; Lee, S. H.; Choi, H. C. In Vivo Near-Infrared Mediated Tumor Destruction by Photothermal Effect of Carbon Nanotubes. *ACS Nano* **2013**, *3*, 3707–3713.

(57) Ghosh, S.; Dutta, S.; Gomes, E.; Carroll, D.; D'Agostino, R.; Olson, J.; Guthold, M.; Gmeiner, W. H. Increased Heating Efficiency and Selective Thermal Ablation of Malignant Tissue with DNA-Encased Multiwalled Carbon Nanotubes. *ACS Nano* **2009**, *3*, 2667–2673.

(58) Robinson, J. T.; Welsher, K.; Tabakman, S. M.; Sherlock, S. P.; Wang, H.; Luong, R.; Dai, H. High Performance In Vivo Near-IR(>1um) Imaging and Photothermal Cancer Therapy with Carbon Nanotubes. *Nano Res.* **2010**, *3*, 779–793.

(59) Liu, Z.; Robinson, J. T.; Tabakman, S. M.; Yang, K.; Dai, H. Carbon Materials for Drug Delivery & Cancer Therapy. *Mater. Today* **2011**, *14*, 316–323.

(60) Yang, K.; Xu, H.; Cheng, L.; Sun, C.; Wang, J.; Liu, Z. In Vitro and in Vivo near-Infrared Photothermal Therapy of Cancer Using Polypyrrole Organic Nanoparticles. *Adv. Mater.* **2012**, *24*, 5586–5592.

(61) Cheng, L.; Yang, K.; Chen, Q.; Liu, Z. Organic Stealth Nanoparticles for Highly Effective in Vivo near-Infrared Photothermal Therapy of Cancer. *ACS Nano* **2012**, *6*, 5605–5613.

(62) Cheng, L.; He, W.; Gong, H.; Wang, C.; Chen, Q.; Cheng, Z.; Liu, Z. PEGylated Micelle Nanoparticles Encapsulating a Non-Fluorescent Near-Infrared Organic Dye as a Safe and Highly-Effective Photothermal Agent for In Vivo Cancer Therapy. *Adv. Funct. Mater.* **2013**, *23*, 5893–5902.

(63) Irvin, J.; Reynolds, J. Low-Oxidation-Potential Conducting Polymer: Alternating Substituted Para-Phenylene and 3,4-Ethylenedioxythiophene Repeat Units. *Polymer (Guildf)*. **1998**, *39*, 2399–2347.

(64) Negishi, E.; Hu, Q.; Huang, Z.; Qian, M.; Wang, G. *The Negishi Coupling: An Update by the Negishi Coupling Enantiopure Sulfoxides and Sulfinamides New Products from Aldrich R & D*; **2005**; Vol. 38.

(65) Yang, Y.; Oldenhius, N.; Buchwald, S. Mild and General Condition for Negishi Cross-Coupling Enabled by the Use of Palladacycle Percatalysts. *Angew Chem Int Ed Engl* **2012**, *29*, 997–1003.

(66) Doblhofer, K.; Rajeshwar, K. Electrochemistry of Conducting Polymers. In *Handbook of Conducting Polymers*; Skotheim, T. A.; Elsenbaumer, R. L.; Reynolds, J. R., Eds.; Marcel Dekker, Inc., **1998**; pp. 531–588.

(67) Beaujuge, P. M.; Ellinger, S.; Reynolds, J. R. The Donor-Acceptor Approach Allows a Black-to-Transmissive Switching Polymeric Electrochrome. *Nat. Mater.* **2008**, *7*, 795–799.

(68) Beaujuge, P. M.; Reynolds, J. R. Color Control in Pi-Conjugated Organic Polymers for Use in Electrochromic Devices. *Chem. Rev.* **2010**, *110*, 268–320.

(69) Amb, C. M.; Dyer, A. L.; Reynolds, J. R. Navigating the Color Palette of Solution-Processable Electrochromic Polymers. *Chem. Mater.* **2011**, *23*, 397–415.

(70) Dal, L. Chapter 2 Conducting Polymers. In *Intelligent Macromolecules for Smart Devices*; Springer, **2004**; Vol. 1980.

(71) Bolto, B. A.; McNeill, R.; Weiss, D. . Electronic Conduction in Polymers. *Aust. J. Chem* **1963**, *16*, 1090–1103.

(72) Derivatives, H.; Louis, J.; Macdiarmid, A. G. Synthesis of Electrically Conducting Organic Polymers : *J.C.S Chem. Comm* **1977**, 578–580.

(73) Skotheim, T.; Reynolds, J. *Handbook of Conducting Polymers*; 3rd ed.; Taylor & Francis Group, **2007**.

(74) Frommer, J. E. Conducting Polymer Solutions. *Acc. Chem. Res* **1986**, *19*, 2–9.

(75) Chemical and Electrochemical Syntheses of Conducting Polymers. In *Conducting Polymers: A New Era in Electrochemistry*; Inzelt, G., Ed.; Monographs in Electrochemistry; Springer Berlin Heidelberg: Berlin, Heidelberg, **2008**; pp. 123–136.

(76) Sapurina, I. Y.; Shishov, M. a. Oxidative Polymerization of Aniline: Molecular Synthesis of Polyaniline and the Formaiton of Supermolecular Structures. In *New Polymers for Special Applications*; Gomes, A., Ed.; **2012**; pp. 251–312.

(77) Irvin, J. Low Oxidation Potential Electroactive Polymers, University of Florida, **1998**.

(78) Guimard, N. K.; Gomez, N.; Schmidt, C. E. Conducting Polymers in Biomedical Engineering. *Prog. Polym. Sci.* **2007**, *32*, 876–921.

(79) Street, G. B. Polarons, Bipolarons, and Solitons in Conducting Polymers. *Acc. Chem. Res.* **1985**, *18*, 309–315.

(80) Wang, Y. Research Progress on a Novel Conductive polymer–poly(3,4-Ethylenedioxythiophene) (PEDOT). *J. Phys. Conf. Ser.* **2009**, *152*, 012023.

(81) Heeger, A. J. Semiconducting and Metallic Polymers: The Fourth Generation of Polymeric Materials. *J. Phys. Chem. B* **2001**, *105*.

(82) Gerard, M.; Chaubey, A.; Malhotra, B. D. Application of Conducting Polymer to Biosensors. *Biosens. Bioeletronics* **2002**, *17*, 345–359.

(83) Abidian, M. R.; Kim, D.-H.; Martin, D. C. Conducting-Polymer Nanotubes for Controlled Drug Release. *Adv. Mater.* **2006**, *18*, 405–409.

(84) Ge, D.; Qi, R.; Mu, J.; Ru, X.; Hong, S.; Ji, S.; Linkov, V.; Shi, W. A Self-Powered and Thermally-Responsive Drug Delivery System Based on Conducting Polymers. *Electrochem. commun.* **2010**, *12*, 1087–1090.

(85) George, P. M.; LaVan, D. A.; Burdick, J. A.; Chen, C. Y.; Liang, E.; Langer, R. Electrically Controlled Drug Delivery from Biotin-Doped Conductive Polypyrrole. *Adv. Mater.* **2006**, *18*, 577–581.

(86) Winkel, K. L.; Carberry, J. R.; Irvin, J. A. Synthesis and Electropolymerization of 3,5-Bis-(3,4-Ethylenedioxythien-2-Yl)-4,4-Dimethyl Isopyrazole: A Donor-Acceptor-Donor Monomer. *J. Electrochem. Soc.* **2013**, *160*, G111–G116.

(87) Hoye, T.; Eklov, B.; Voloshin, M. No-D NMR Spectroscopy as a Convenient Method for Titering Organolithium (RLi), RMgX, and LDA Solutions. *Org. Lett.* **2004**, *6*, 2567–2570.

(88) Ko, S. B.; Cho, A. N.; Kim, M. J.; Lee, C. R.; Park, N. G. Alkyloxy Substituted Organic Dyes for High Voltage Dye-Sensitized Solar Cell: Effect of Alkyloxy Chain Length on Open-Circuit Voltage. *Dye. Pigment.* **2012**, *94*, 88–98.

(89) Umezawa, K.; Oshima, T.; Yoshizawa-Fujita, M.; Takeoka, Y.; Rikukawa, M. Synthesis of Hydrophilic-Hydrophobic Block Copolymer Ionomers Based on Polyphenylenes. *ACS Macro Lett.* **2012**, *1*, 969–972.

(90) Aranzaes, J. R.; Daniel, M.-C.; Astruc, D. Metallocenes as References for the Determination of Redox Potentials by Cyclic Voltammetry Permethylated Iron and Cobalt Sandwich Complexes, Inhibition by Polyamine Dendrimers, and the Role of Hydroxy-Containing Ferrocenes. *Can. J. Chem.* **2006**, *84*, 288–299.

(91) Echavarren, A. M.; Stille, J. K. Palladium-Catalyzed Coupling of Aryl Triflates with Organostannanes. *J. Am. Chem. Soc.* **1987**, 5478–5486.

(92) Imperato, G.; Vasold, R.; König, B. Stille Reactions with Tetraalkylstannanes and Phenyltrialkylstannanes in Low Melting Sugar-Urea-Salt Mixtures. *Adv. Synth. Catal.* **2006**, *348*, 2243–2247.

(93) Sortzing, G. A.; Reddinger, J. L.; Reynolds, J. R. Redox Active Electrochromic Polymers from Low Oxidation Containing 3,4-Ethylenedioxythiophene (EDOT). *Synth. Met.* **1997**, *84*, 199–201.

(94) Negishi, E. Palladium- or Nickel-Catalyzed Cross Coupling. A New Selective Method for Carbon-Carbon Bond Formation. *Acc. Chem. Res* **1982**, *15*, 340–348.

(95) Long, Y. T.; Rong, H. T.; Buck, M.; Grunze, M. Odd-Even Effects in the Cyclic Voltammetry of Self-Assembled Monolayers of Biphenyl Based Thiols. *J. Electroanal. Chem.* **2002**, *524-525*, 62–67.

(96) Irvin, D. Modification of the Electronic Properties of Conjugated Polymers, University of Florida, **1998**.

(97) Ananthakrishnan, N.; Padmanaban, G.; Ramakrishnan, S.; Reynolds, J. R. Tuning Polymer Light-Emitting Device Emission Colors in Ternary Blends Composed of Conjugated and Nonconjugated Polymers. *Macromolecules* **2005**, *38*, 7660–7669.

(98) Irvin, D. J.; Reynolds, J. R. Tuning the Band Gap of Easily Oxidized bis(2-Thienyl)- and bis(2-(3,4-Ethylenedioxythiophene))-Phenylene Polymers. *Polym. Adv. Technol.* **1998**, *9*, 260–265.

(99) Ojio, T.; Miyata, S. Highly Transparent and Conducting Polypyrrole-Poly(vinyl Alcohol) Composite Films Prepared by Gas State Polymerization. *Polym. J.* **1986**, *18*, 95–98.

(100) Bjorklund, R. B.; Lundstrsm, I. Some Properties of Polypyrrole-Paper Composites. *J. Electron. Mater.* **1984**, *13*, 211–230.

(101) Razaq, A.; Strømme, M.; Nyholm, L.; Mihranyan, A. Ultrafast All-Polymer Paper-Based Batteries. *Nano Lett.* **2009**, *9*, 3635–3639.

(102) Nyström, G.; Mihranyan, A.; Razaq, A.; Lindström, T.; Nyholm, L.; Strømme, M. A Nanocellulose Polypyrrole Composite Based on Microfibrillated Cellulose from Wood. *J. Phys. Chem. B* **2010**, *114*, 4178–4182.

(103) Mihranyan, A. Cellulose from Cladophorales Green Algae: From Environmental Problem to High-Tech Composite Materials. *J. Appl. Polym. Sci.* **2010**, *119*, 2449–2460.

(104) Kirchmeyer, S.; Knud, R.; Simpson, J. C. Poly(3,4-Ethylenedioxythiophene)-Scientific Importance, Remarkable Properties, and Applicaitons. In *Conjugated Polymers Theroy, Synthesis, Properties, adn Characterization*; Skotheim, T. A.; Reynolds, J. R., Eds.; CRC Press, **2007**.

(105) Hanemann, T.; Szabó, D. V. Polymer-Nanoparticle Composites: From Synthesis to Modern Applications. *Materials (Basel).* **2010**, *3*, 3468–3517.

(106) Ausa, J. Emulsion Polymerization : From Fundamental Mechanisms to. *J. Polym. Sci. Part A Polym. Chem.* **2004**, *42*, 1025–1041.

(107) Yamak, H. B. Emulsion Polymerization : Effects of Polymerization Variables on the Properties of Vinyl Acetate Based Emulsion Polymers. In *Polymer Science*; Yulmas, F., Ed.; Intech, **2013**; pp. 35–73.

(108) Nagavarma, B. V. N.; Yadav, H. K. S.; Ayaz, A.; Vasudha, L. S.; Shivakumar, H. G. Different Techniques for Preparation of Polymeric Nanopaticles-A Review. *Asian J. Pharaceutical Clin. Res.* **2012**, *5*, 16–23.

(109) Amaike, M.; Yamamoto, H. Preparation of Polypyrrole by Emulsion Polymerization Using Hydroxypropyl Cellulose. *Polym. J.* **2006**, *38*, 703–709.

(110) Choi, J. W.; Han, M. G.; Kim, S. Y.; Oh, S. G.; Im, S. S. Poly(3,4-Ethylenedioxythiophene) Nanoparticles Prepared in Aqueous DBSA Solutions. *Synth. Met.* **2004**, *141*, 293–299.

(111) Wu, C.-H.; Don, T.-M.; Chiu, W.-Y. Characterization and Conversion Determination of Stable PEDOT Latex Nanoparticles Synthesized by Emulsion Polymerization. *Polymer (Guildf).* **2011**, *52*, 1375–1384.

(112) Han, Y. K.; Yih, J. N.; Chang, M. Y.; Huang, W. Y.; Ho, K. S.; Hsieh, T. H.; Lou, J. G. Facile Synthesis of Aqueous-Dispersible Nano-PEDOT:PSS-Co-MA Core/shell Colloids through Spray Emulsion Polymerization. *Macromol. Chem. Phys.* **2011**, *212*, 361–366.

(113) Hoshina, Y.; Zaragoza-Contreras, E. A.; Farnood, R.; Kobayashi, T. Nanosized Polypyrrole Affected by Surfactant Agitation for Emulsion Polymerization. *Polym. Bull.* **2012**, *68*, 1689–1705.

(114) Peighambardoust, S. J.; Pourabbas, B. Synthesis and Characterization of Conductive Polypyrrole/Montmorillonite Nanocomposites via One-Pot Emulsion Polymerization. *Macromol. Symp.* **2007**, *247*, 99–109.

(115) Armes, S. P. Sterically Stabilized Polyaniline Colloids. In *Handbook of Conductive Po*; Skotheim, T. A.; Elsenbaumer, R. L.; Reynolds, J. R., Eds.; Marcel Dekker, Inc., **1998**.

(116) Sun, X.; Hagner, M. Novel Poly (acrylic Acid) -Mediated Formation of Conducting Polymer Nanowires. *Mactomolecules* **2007**, *25*, 8537–8539.

(117) Jin, S.-M.; Joo, Y.-T.; Park, Y.-J.; Kim, Y. Facile Preperation of Poly(3,4-Ethylenedioxythiophene) Nanoparticles via a Miniemulsion Polymerization Process. *J. Appl. Polym.* **2011**, *121*, 1442–1449.

(118) Sada, K.; Takeuchi, M.; Fujita, N.; Numata, M.; Shinkai, S. Post-Polymerization of Preorganized Assemblies for Creating Shape-Controlled Functional Materials. *Chem. Soc. Rev.* **2007**, *36*, 415–435.

(119) Müller, K.; Park, M.-K.; Klapper, M.; Knoll, W.; Müllen, K. Synthesis and Layer-by-Layer Deposition of Spherical Poly(3,4-Ethylenedioxythiophene) Nanoparticles - Toward Fast Switching Times between Reduced and Oxidized States. *Macromol. Chem. Phys.* **2007**, *208*, 1394–1401.

(120) Roper, D. K.; Ahn, W.; Hoepfner, M. Microscale Heat Transfer Transduced by Surface Plasmon Resonant Gold Nanoparticles. *J. Phys. Chem. C* **2007**, *111*, 3636–3641.

(121) Morgan, D. Tetrazolium (MTT) Assay for Cellular Viability and Activity. In *Methods in Molecular Biology*; Humana Press Inc.

(122) Wilson, N. H.; Hardisty, J. F.; Hayes, J. R. *Principles and Methods of Toxicology*; Hayes, W. A., Ed.; 5th ed.; **2008**.

(123) Chicheł, A.; Skowronek, J.; Kubaszewska, M.; Kanikowski, M. Hyperthermia – Description of a Method and a Review of Clinical Applications. *Reports Pract. Oncol. Radiother.* **2007**, *12*, 267–275.

(124) Tong, L.; Cheng, J.-X. Gold Nanorod-Mediated Photothermolysis Induces Apoptosis of Macrophases via Damage of Mitochondria. *Nanomedicine* **2009**, *4*, 265–276.

(125) Pattani, V. P.; Shah, J.; Atalis, A.; Sharma, A.; Tunnell, J. W. Role of Apoptosis and Necrosis in Cell Death Induced by Nanoparticle-Mediated Photothermal Therapy. *J. Nanoparticle Res.* **2015**, *17*, 20.

(126) Mosquera, A.; Riveiros, R.; Sestelo, J. P.; Sarandeses, L. Cross-Coupling Reactions of Indium Organometallics with 2,5-Dihalopyrimidines: Synthesis of Hyrtinadine A. *Org. Lett.* **2008**, *10*, 3745–3748.

(127) Ogawa, D.; Nishihara, Y. Applied Cross-Coupling Reactions. In; Nishihara, Y., Ed.; Springer, **2013**; Vol. 80, pp. 137–173.

(128) Han, Y.-K.; Yih, J.-N.; Chang, M.-Y.; Huang, W.-Y.; Ho, K.-S.; Hsieh, T.-H.; Lou, J.-G. Facile Synthesis of Aqueous-Dispersible Nano-PEDOT:PSS-Co-MA Core/Shell Colloids Through Spray Emulsion Polymerization. *Macromol. Chem. Phys.* **2010**, 361–366.